Singular orbital diamagnetism and paramagnetism in graphene

Jorge Vallejo Bustamante

université
PARIS-SACLAY

Singular orbital diamagnetism and paramagnetism in graphene.

Diamagnétisme et paramagnétisme orbital singulier dans le graphène.

Thèse de doctorat de l'université Paris-Saclay

École doctorale n°564, physique en Ile de France (PIF)
Spécialité de doctorat: Physique
Graduate School : Physique, Référent : Faculté des sciences d'Orsay

Thèse préparée dans l'unité de recherche Laboratoire de Physique des Solides UMR 8502, sous la direction de Hélène BOUCHIAT, Directrice de recherche, la co-direction de Meydi FERRIER, Maître de conférences

Thèse soutenue à Paris-Saclay, le 24 février 2023, par

Jorge VALLEJO BUSTAMANTE

Composition du jury

Claude CHAPELIER Directeur de Recherche, CEA, Université Grenoble-Alpes	Président
Franck BALESTRO Professeur, Université Grenoble-Alpes	Rapporteur & Examinateur
Giovanni VIGNALE Professeur (E), University of Missouri	Rapporteur & Examinateur
Nedjma BENDIAB Professeure d'Université, Université Grenoble-Alpes	Examinatrice
Christophe MORA Professeur, Université Paris Diderot	Examinateur

THESE DE DOCTORAT

NNT : 2023UPASP024

université PARIS-SACLAY

ÉCOLE DOCTORALE
Physique en Île-de-France (PIF)

Titre: Diamagnétisme et paramagnétisme orbital singulier dans le graphène.
Mots clés: graphène, orbital, diamagnétisme, paramagnétisme, GMR

Résumé: Le graphène est un des matériaux les plus étudiés dans la matière condensée en raison de ses propriétés surprenantes liées à sa relation de dispersion linéaire. Une de ces propriétés est la susceptibilité orbitale divergente diamagnétique au point de Dirac. Cette caractéristique, qui est une signature étonnante de la phase anormale de Berry égale à π dans le graphène, avait été prédite plusieurs décennies auparavant, mais il a été difficile de la mesurer au niveau d'une monocouche unique. Une autre prédiction passionnante concerne le magnétisme orbital des cristaux 2D en général. L'existence d'une susceptibilité paramagnétique orbitale divergente a été prédite. Ces singularités sont attendues aux points selle de la structure de bandes.

Pour réaliser nos expériences, nous avons utilisé une nouvelle technique qui implique des sondes de magnétorésistance géantes (GMR) très sensibles en combinaison avec le contrôle du potentiel chimique par une modulation de la grille. Nous avons ainsi réussi à mesurer la susceptibilité diamagnétique orbitale singulière dans le graphène monocouche, pour la première fois au niveau d'une monocouche unique. Nous avons également mesuré la susceptibilité paramagnétique orbitale singulière du graphène dans un superpotentiel moiré qui provient de l'alignement du graphène et du nitrure de bore. Nous présentons également les résultats préliminaires de la susceptibilité orbitale du graphène bicouche AB, et son évolution lorsqu'un champ électrique perpendiculaire est appliqué. Nos résultats ouvrent une nouvelle voie pour explorer le magnétisme orbital et les courants orbitaux dans les matériaux 2D. Cette expérience devrait également permettre complémenter l'étude des particularités de la géométrie de la structure de bande des cristaux 2D, en particulier les anomalies de phase de Berry ou les points selle, ou révéler l'existence de courants de boucle balistique le long des bords des isolants topologiques 2D.

Title: Singular orbital diamagnetism and paramagnetism in graphene.
Keywords: graphene, orbital, diamagnetism, paramagnetism, GMR

Abstract: Graphene is one the most studied materials in condensed matter because of its astonishing properties related to its linear dispersion relation. One of these properties is the diamagnetic divergent orbital susceptibility at the Dirac point. This characteristic, which is a striking signature of the anomalous π Berry phase in graphene, was predicted many decades before, but it has been challenging to measure at a single-flake level. Another exciting prediction concerns the orbital magnetism of 2D crystals in general. The existence of a divergent orbital paramagnetic susceptibility has been predicted. These singularities are expected at the saddle points of the band structure.

To realize our experiments he have used a new technique that involves highly sensitive giant magneto-resistant (GMR) probes in combination with chemical potential control through a gate modulation. By the means of this technique, we have measured the singular orbital diamagnetic susceptibility in monolayer graphene, for the first time at single-flake level. We have also measured the singular orbital paramagnetic susceptibility in graphene in a moiré superpotential that comes from the alignment of graphene and boron nitride. We also present the preliminary results of the orbital susceptibility of AB bilayer graphene, and its evolution when a perpendicular electric field is applied. Our results open a new way to explore the orbital magnetism and currents in 2D materials. This experiment should also complement the investigation of the particularities of the geometry of the band structure of 2D crystals, particularly Berry phase anomalies or saddle points, or reveal the existence of ballistic loop currents along the edges of 2D topological insulators.

université PARIS-SACLAY

Singular orbital diamagnetism and paramagnetism in graphene.

Diamagnétisme et paramagnétisme orbital singulier dans le graphène.

Thèse de doctorat de l'université Paris-Saclay

École doctorale n°564, physique en Ile de France (PIF)
Spécialité de doctorat: Physique
Graduate School : Physique, Référent : Faculté des sciences d'Orsay

Thèse préparée dans l'unité de recherche Laboratoire de Physique des Solides UMR 8502, sous la direction de Hélène BOUCHIAT, Directrice de recherche, la co-direction de Meydi FERRIER, Maître de conférences

Thèse soutenue à Paris-Saclay, le 24 février 2023, par

Jorge VALLEJO BUSTAMANTE

Composition du jury

Claude CHAPELIER Directeur de Recherche, CEA, Université Grenoble-Alpes	Président
Franck BALESTRO Professeur, Université Grenoble-Alpes	Rapporteur & Examinateur
Giovanni VIGNALE Professeur (E), University of Missouri	Rapporteur & Examinateur
Nedjma BENDIAB Professeure d'Université, Université Grenoble-Alpes	Examinatrice
Christophe MORA Professeur, Université Paris Diderot	Examinateur
Gilles MONTAMBAUX Directeur de Recherche (E) CNRS, Université Paris-Saclay	Jury Invité
Hélène Bouchiat Directrice de Recherche CNRS, Université Paris-Saclay	Directrice de Thèse

THESE DE DOCTORAT
NNT : 2023UPASP024

Acknowledgments

I would like to give infinite thanks to my thesis supervisors Hélène and Meydi for all the incredible support they gave me during these years. If something has been achieved is in great measure because of their effort to help me work in the best conditions. In particular, Hélène has become a role model not only as a scientist but as a human being for me. I will try to replicate the example of professionalism and kindness in my future life.

I want also to give big thanks to the Mesoscopic Physics group in LPS. Thanks to all the team for the uncountable discussions, in particular, thanks to Sophie for the questions, remarks and suggestions. To all the group, thanks for the good moments, for the lunch time, for the traditional pause café/chocolat, for your kindness and support. You have become my family in France.

Thanks to the Theory group: Gilles, Jean Noel and Fréderic. I have learned so much from every reunion and I only have words of admiration for you. Thanks for making it a bit more understandable the complicated formulas, always in a kind way.

I would like to thank Claude, Myriam and Elodie whose amazing work is the central pillar for these experiments.

Thanks to Rebeca for having opened the doors of her lab to me, for teaching and helping me with the fabrication. And thanks for the many discussions about the world around twistronics. It has opened my interest to this part of physics.

I want to say thanks also to LPS, and all the people that make it an amazing lab. Thanks to your effort, you make the students feel like home in there.

To the closest friends I've had here Xavier and Victor. Thank you for always sharing pleasant moments, lots of laughter in the office and for your solidarity in less joyful moments. Thank you also for sharing your knowledge and experience in fabrication as well as in life.

I would like to give the credits to Yan for always being by my side. For having the patience to tolerate me in the stressful moments and for sharing with me always a kind word and a smile. Your company has made this time even more enjoyable.

A mi familia, el pilar fundamental de mi vida, aún en la distancia he podido sentir su apoyo y su cariño. Infinitas gracias por todo. Ustedes han estado siempre conmigo apoyándome para cumplir mis sueños.

Contents

Introduction

The study of orbital currents has started to raise interest by analogy to its spin counterpart as a way to reveal, access and control new degrees of freedom that can be used in new technologies [1]. In recent studies, it has been demonstrated that controlling pure orbital currents is possible [2, 3, 4]. Also, it has been shown that orbital currents can mediate and explain the spin Hall effect (SHE) or valley Hall effect (VHE) [5, 6, 7] in 2D materials. Other phenomena studied include for example orbital Rashba Edelstein effects [8, 9, 10] or orbital torque. However, orbitronics is far less developed than spintronics, partly due to the existence of orbital quenching in some metals (particularly from the Fe family). This phenomenon is known for reducing the orbital angular momentum to zero and thus, the spin is the only relevant contribution to angular momentum and magnetism in these type of systems.

Nevertheless, there are systems where the orbital part is an important contribution for magnetism, for example, Landau diamagnetism in metals [11] that originates from the motion of effectively free electrons in magnetic fields is of the same order of magnitude as the spin Pauli magnetism. In some semi-metals as graphite or bismuth, orbital magnetism becomes the dominant contribution and even arrives to a divergence in the case of graphene [12]. Other examples are the Meissner effect in superconductors, the magnetization of mesoscopic copper rings produced by persistent currents [13], or more recently, the observation of intra-unit-cell magnetism that is attributed to loop currents in the unit cell of high-T_c superconductor YBCO [14].

Among the systems where the orbital magnetism presents exciting properties we can find graphene and some of the van der Waals structures based on it. For example, the existance of orbital ferromagnets in twisted bilayer graphene [15, 16] has been found recently.

During this thesis, we focused on the experimental study of the orbital magnetism of 3 systems: monolayer graphene, graphene on a moiré potential and bilayer graphene.

In this spirit, we dedicate the first chapter 1 to orbital magnetism. In this chapter we will present a very brief introduction to the fundamental definitions needed for the rest of the manuscript. We will also mention the interrelation between the experimentally accessible features of the orbital susceptibility and the particularities of the band structure that are at their origins.

The general properties and most fundamental characteristics of graphene are presented in chapter 2. Here we used the tight binding model to give a very simple explanation of its most prominent magnetic property, the McClure diamagnetic peak diverging at the Dirac point, which is a striking signature of the anomalous π Berry phase in graphene.

In the third chapter, we will present one of the key aspects that makes possible the experimental detection: the giant-magneto-resistance probes (GMRs). We will present the characteristics as well as a simple but intuitive model to explain their functioning in a general way.

Chapter 4 details the set up and principle of the experimental detection. It highlights the technique that allows us to reduce the contributions of spurious magnetic signals. We also present the fabrication of our samples in this chapter.

The experimental study of the orbital diamagnetic singular response in graphene is given in chapter 5. It shows the measurements of the gate-voltage dependent magnetization of a single monolayer graphene flake encapsulated between boron nitride crystals. It is also accompanied with the a theoretical model that allows for understanding of the details. This chapter is taken from the article [17] that was published during this project.

Next on chapter 6, we present the experimental exploration of the orbital magnetism of monolayer graphene in a moiré potential. This was made by aligning the graphene flake with one of the BN crystals that encapsulates it. In particular, we focus on the region where saddle points in the band structure are expected, which is accompanied by divergences in the density of states. At these points, the susceptibility is expected [18] and experimentally found to be paramagnetic .

We present the preliminary results of the orbital magnetism of bilayer graphene in chapter 7. Here, we mainly focus on the evolution of the susceptibility as a function of the perpendicular electric displacement field.

Finally, we present the summary of this project and the results as a conclusion section.

1 - Orbital magnetism

It is a well established fact that magnetism can originate, either from the spins of fundamental particles, or on the other side, it can come from the quantum mechanical motion of charged particles. The later is known as orbital magnetism and is the subject of experimental interest in this thesis. The orbital motion or spin effect of this charges can be localized, as for example electrons orbiting in atoms, or delocalized, as it occurs in a crystal with electrons moving in the bands. In this delocalized magnetism, Bloch electrons have orbital and spin momenta that can both interact with magnetic fields. It is this delocalized component of orbital magnetism that is studied in this thesis. In particular, we are interested in electrons in graphene crystals, so their motion is restricted to the 2D plane.

Recently, orbital magnetism in general has started to be seen under a perspective where multiband physics plays a major role [19, 20, 21]: the orbital motion within one band is influenced by the other bands, through virtual interband transitions that can be mediated by magnetic fields. These interband transitions can reflect non-trivial geometry of band eigenstates, for example the contributions of the Berry phase [22, 23, 24]. In particular in reference [21], it was shown that for a two-band system, with electron-hole symmetry, the orbital susceptibility can be decomposed in the sum of contributions from different origins. For example, the Landau-Peierls susceptibility (contributions from each individual band proportional to the curvature of the bands), a term containing the Berry curvature and a term characterized by the metric tensor. This allows us to see that orbital susceptibility is deeply connected to the geometry of the Bloch functions in the reciprocal space and so, by measuring this quantity, we can have an experimental way to obtain information about these properties.

We will not give the full expressions for the orbital susceptibility in this manuscript (that can be found in [20, 21] for example). Instead, we will focus, for each experiment, on the particular behavior of the band structure that we were able to explore. In consequence, it is first convenient to introduce some definitions and cases that we will use frequently throughout this manuscript.

1.1 . Magnetization, susceptibility and magnetic field

The main relation we use defines the magnetic linear response of a system in the presence of an external magnetic field

$$\vec{M} \equiv \chi_{orb}\vec{B} \tag{1.1}$$

where $\vec{B}$ is the external magnetic field, χ_{orb} is the susceptibility and $\vec{M}$ is the magnetization of the system. Because in 2D, $\vec{M}$ is the density of magnetic moments

$\vec{m}$ per unit surface, the magnetization will be given in Amperes, A, the external field in Tesla, T, and so, the susceptibility will be given in Ampere per Tesla, A/T.

When the magnetization opposes to the magnetic field, equivalently $\vec{M}$ and $\vec{B}$ are anti-parallel, then the susceptibility is negative, $\chi_{orb} < 0$. We talk in this case of orbital diamagnetism. In the opposite case, when $\vec{M}$ and $\vec{B}$ are parallel, we talk about orbital paramagnetism and $\chi_{orb} > 0$. All this is general to 2D magnetism.

1.2 . Magnetism as a thermodynamic property

Taking into consideration a large number of electrons, as it is the case inside a crystal, magnetization must be defined as a statistical property. It accounts for the effect of the external field in the ensemble of charged particles in the crystal. To quantify this effect, first we need to define the statistical ensemble. It is convenient for us to use the grand canonical ensemble in which the temperature T and chemical potential μ are defined by reservoirs. This is justified by the set up of our experiments in which the sample is generally in a thermal bath and the chemical potential will be controlled and fixed by using a gate. In this ensemble, the characteristic state function is the grand potential Ω. This is the quantity that allows us to obtain all the information of the system, particularly the effects of the magnetic field. In this case, the magnetization of a grand canonical ensemble is given by:

$$\vec{M} = -\frac{1}{S}\frac{\partial \Omega}{\partial B}\vec{u}_z \tag{1.2}$$

and consequently, the orbital susceptibility is

$$\chi_{orb} = -\frac{1}{S}\frac{\partial^2 \Omega}{\partial B^2}\bigg|_{B\to 0}. \tag{1.3}$$

Focusing in the 2D crystals, there are several different regimes that we could find while studying the characteristics and behavior of the orbital susceptibility. This characteristics of course are related with their band structure. This is the reason why before going into the detail of experimental realization, it is necessary to mention some very basic ground ideas about the magnetism and what to expect due to some particular shapes in the band structure. We will focus in a few of them, those relevant in the experiments performed during this thesis.

Even if not all of them are achievable in the same type of crystal and it is worth mentioning as they are part of what we can find in a normal metal, in graphene, or in a moiré superlattice or in bilayer grapehene.

1.3 . Magnetic moment of a classical charge

In order to go further with the understanding of orbital magnetism, it is always useful to draw some parallel lines to what can be easily understood through intuition

and for this we can use classical mechanics. For instance, a classical charge moving with a velocity $\vec{v} = v_x\vec{u}_x + v_y\vec{u}_y$, in an electromagnetic field $(\vec{E}, \vec{B} = B\vec{u}_z)$ experiences a force given by

$$\vec{F} = q\vec{E} + q\vec{v} \times \vec{B}. \tag{1.4}$$

From this equation we see that because $\vec{v}$ and $\vec{B}$ are perpendicular, the charge will move forming loops, which are known as the cyclotron orbits. These orbits are defined by their radius r_c and the frequency of orbiting ω_c, given by

$$\omega_c = \frac{qB}{m}, \tag{1.5}$$

related by $r_c\omega_c = v$. m is known as the cyclotron mass.

We can then define a surface $S = \pi r_c^2$ and a current loop $I = q\omega_c$. This current generates a magnetic moment $\vec{m}$ given by $\vec{m} = IS\vec{u}_{norm}$, being $\vec{u}_{norm}$ the perpendicular direction of the oriented surface delimited by the current. Figure 1.1 shows this orientation for a positive charge. It also shows the directions of the vectors that are involved in equation 1.4 and the magnetic moment. As it is shown, the sign of the normal direction is opposed to the one of the external magnetic field that produces the loop, so the magnetic moment will be opposed to the external field. Then, the orbital magnetization of a charge moving in a plane is equivalent to a current

$$\vec{M}_C = \frac{\vec{m}}{S} = -I_{orb}\vec{u}_z = -\frac{q^2B}{m}\vec{u}_z \tag{1.6}$$

and the susceptibility is

$$\chi_C = -\frac{q^2}{m}. \tag{1.7}$$

In this way, every time we talk about orbital magnetism, we will automatically define the equivalent orbital current. That is why all along this manuscript we speak about orbital magnetism and orbital current indistinctly. It is worth noting that regardless the sign of the charge, the susceptibility due to the movement of classical charges in 2D is negative, therefore diamagnetic.

Equation 1.4 tells us that free classical charges in a magnetic field will move in orbits whose magnetization direction is opposed to that of the external field. Therefore, we may be tempted to think that diamagnetism at every scale is just a consequence of the Lorentz force, even further, that only diamagnetism is possible due to orbital movement. However, this is a good example of a conclusion that we get when we use a classical argument and stop the reasoning midway through it, paraphrasing Feynman. It turns out that magnetism needs a quantum description to be understood and classical mechanics is a very useful tool to draw intuitive analogues, but not to explain magnetism. In fact, when classical statistical mechanics is applied *rigorously* to an ensemble of electrons at thermal equilibrium, the net magnetization of the system is identically null.

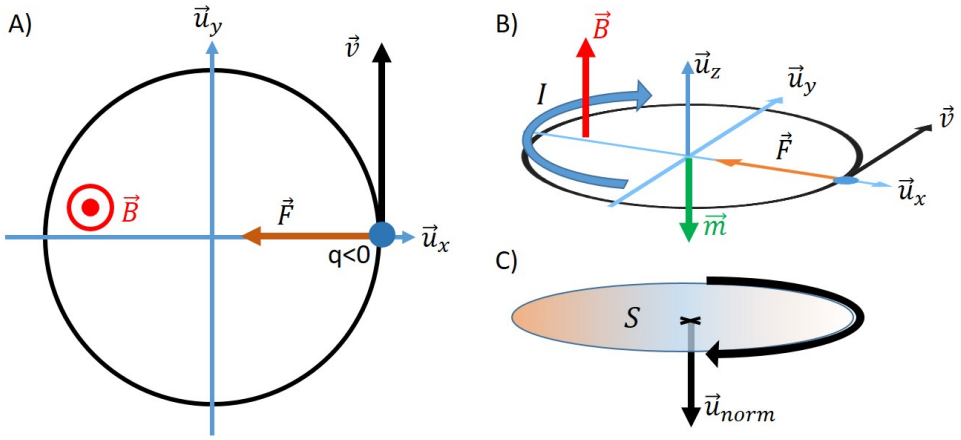

Figure 1.1: A) Shows the direction of the Lorentz force acting on a negative charge. B) Shows the current I associated to the movement of the negative charge in A. The current is positive in the direction of positive moving charges. C) Definition of an oriented surface. The orientation is given with respect to the current I. This sign can be viewed as analogous to the Lenz law.

This is known as the Bohr-van Leeuwen theorem. The intuitive argument is that according to Maxwell-Boltzmann statistics, the probability of the system of being in a particular state of energy E is proportional to $e^{-E/kT}$. E accounts for the kinetic and potential energy so it is independent from the magnetic field. In other words, because magnetic field produces a force perpendicular to the velocity, it does not generate work, so it does not change the energy of the particles. Then, the probability of any state of movement with magnetic field at thermal equilibrium will be the same as the probability without field. Figure 1.2 gives a schematic explanation of the impossibility of orbital magnetism with classical orbits.

1.4 . Case of a 2D free electron gas

One of the simplest cases of orbital magnetism comes from free electrons. We can use equation 1.3 to study the behavior of electrons in a 2D electron gas (2DEG). This is handy when we want to compare to the case of the classical result given in 1.7 and later on, to put into perspective the different results obtained.

The treatment to study the susceptibility consists on studying free electrons in a magnetic field, which obey the Schrodinger equation with minimal coupling. This means that the moment operator is replaced via the substitution [21]

$$\vec{p} \rightarrow \vec{\Pi} = \vec{p} - e\vec{A}, \tag{1.8}$$

where $\vec{A}$ is the vector potential associated to the external magnetic field $\vec{B} =$

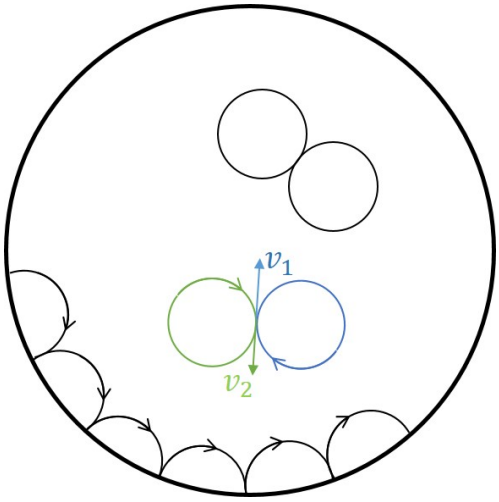

Figure 1.2: Classical trajectories of electrons in 2DEG in the presence of a magnetic field. In each point there are 2 trajectories with velocities v_1 and v_2 that are equal and opposed. Then, the contribution to angular momentum in each point is zero. Therefore, there is no magnetism in a 2DEG with classical trajectories. Adapted from [25].

$\vec{\nabla} \times \vec{A}$. Then, Schrodinger equation becomes

$$\hat{H}\Psi = \frac{1}{2m}\vec{\Pi}^2\Psi = E\Psi. \tag{1.9}$$

It is usual To solve this equation by rewriting this equation in the form of an harmonic oscillator, whose eigenenergies are given by

$$E_n = \hbar\omega\left(n + \frac{1}{2}\right). \tag{1.10}$$

The index n is the number of Landau levels. Then, by calculating the grand potential:

$$\Omega = k_B T g_B \sum_{n\geq 0} \ln\left(1 + e^{-(\hbar\omega_c(n+1/2)-\mu)/k_B T}\right) \tag{1.11}$$

and by applying the definition of susceptibility given by 1.3, and considering the limit when $\alpha \equiv \hbar\omega_c/k_B T << 1$, then, the susceptibility at $T \to 0$, up to second order in α is [21].

$$\chi_L = -\frac{e^2}{24\pi m}. \tag{1.12}$$

We can think that the Landau susceptibility is the quantum description of susceptibility of the one calculated in 1.7, arising from the formation of the Landau levels as parallel to the cyclotron orbits.

This Landau susceptibility exists also in the majority of normal metals, however the mass that appears must be replaced by the effective mass to take into

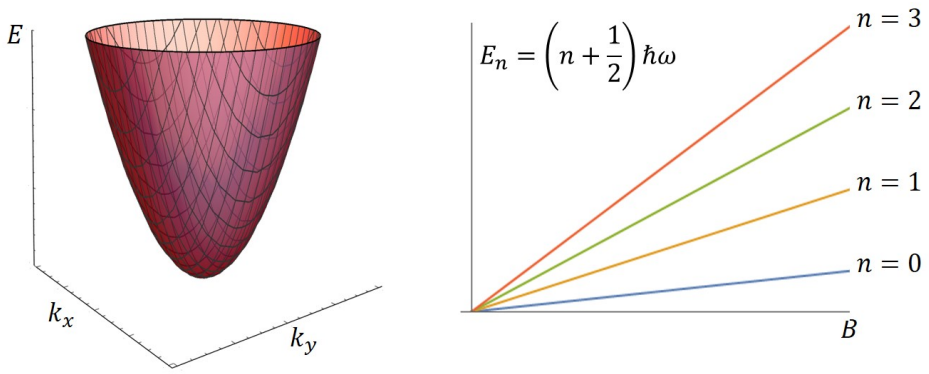

Figure 1.3: Left: Parabolic dispersion relation of a 2EDG. This is behavior is equivalent to the one found in normal metals, where the dispersion relation is parabolic. Right: Landau levels corresponding to the dispersion relation in the right. Adapted from [21].

account the effects of the potential of the crystal in the band structure. Even more important, this description is only valid when the band can be considered isolated, i.e. separated from the neighboring bands by large enough energy gaps.

It was shown in [26, 27, 28], that orbital magnetism of semi-metals cannot be described by expression 1.12. As an example, [27] explains the diamagnetism in Bismuth as the contribution of the interband terms.

1.5 . Graphene in the vicinity of its neutrality point

In particular, the orbital susceptibility of graphene close to the neutrality point is determined by its Dirac conic band structure around K points, where graphene exhibits the crossing of two bands. Contrasting with the behavior of quadratic dispersion relation that is found in free electrons, electrons in graphene present a linear dispersion relation. This means that Dirac electrons behave as if their mass is effectively null. The consequences of this dispersion relation in the electronic properties of graphene has been extensively studied both theoretical and experimentally. One of this properties characteristics of graphene is its Landau spectrum, which are the energy levels of graphene in the presence of a magnetic field. Rabi [29] was the first to be interested in the study of the behavior of free Dirac electrons in a region of homogeneous magnetic field. Then, McClure in 1956 [12] explicitly calculated the Landau levels in graphene as $\epsilon_n = \text{sign}(n)\sqrt{2v_F^2 eB|n|}$. We will explicitly show a way to calculate these levels in chapter 2 in the case of graphene in the tight binding model, but for now, we will just compare this result to the case of free electrons. McClure also calculated the zero field orbital susceptibility, given by

$$\chi_{McC} = -\frac{e^2 v_F^2}{6\pi k_B T}\text{sech}^2(\mu/2k_B T). \tag{1.13}$$

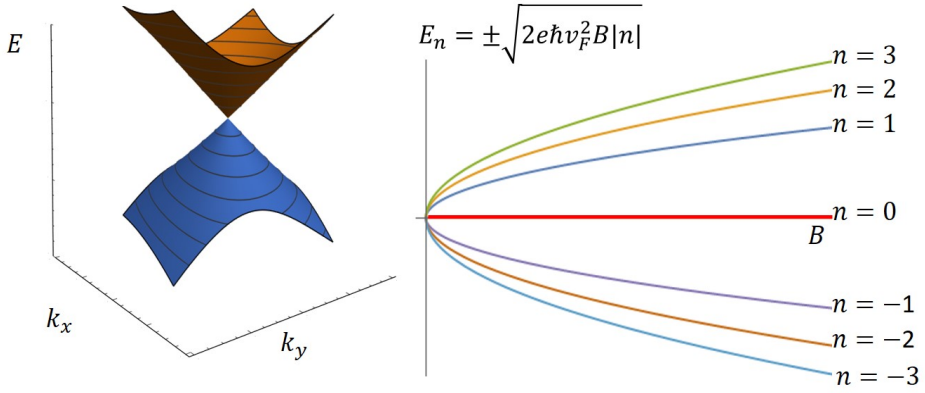

Figure 1.4: Left: linear dispersion relation. This is the behavior of electrons in graphene at low energies. Right: Landau levels for a linear dispersion relation. Adapted from [21].

where v_F is the Fermi velocity of graphene and n is the number of the Landau level.

By directly comparing χ_{McC} at ambient temperature ($T = 300$K) with χ_L (which is constant), we find that at $\mu = 0$, that $\chi_{McC} \sim 100\chi_L$. This provided an explanation of the large diamagnetism observed in graphite. We also note that this susceptibility diverges at low T when the Fermi level stands a the charge neutrality point (CNP), because $\chi \sim 1/T$.

1.6 . Van Hove singularities

Another feature that one can find while exploring the bands of graphene-based compounds are van Hove singularities. Following [30], we can relate the density of states, g_n, explicitly with the band structure of a crystal. The relation in 3D is:

$$g_n(\epsilon) = \int_{S_n(\epsilon)} \frac{dS}{4\pi^3} \frac{1}{|\nabla \epsilon_n(\vec{k})|}, \tag{1.14}$$

where the integral is made on the surface S_n in k-space, which is the surface of constant energy $\epsilon_n(\vec{k}) = \epsilon$. This illustrates a general result concerning the density of states: whenever the gradient of the dispersion relation at the band, $|\nabla \epsilon_n(\vec{k})|$ vanishes, then, the integrand of equation 1.14 diverges. This gradient can vanish at local maxima, minima or at saddle points. In 3D, the density of states remains finite although its derivative $dg/d\epsilon$ diverges. However, for a 2D lattice, the density of states diverges at a saddle point. A saddle point in the band structure is a (mathematical) critical point that exhibits neither a local maximum nor a local minimum. This means that the gradient $|\nabla \epsilon_n(\vec{k})|$ vanishes at this point but the curvature in perpendicular directions have opposite signs (lets say $\sim \partial^2\epsilon/\partial x^2 > 0$ and $\sim \partial^2\epsilon/\partial y^2 < 0$). Vignale [18] has shown that for a 2D lattice, the orbital

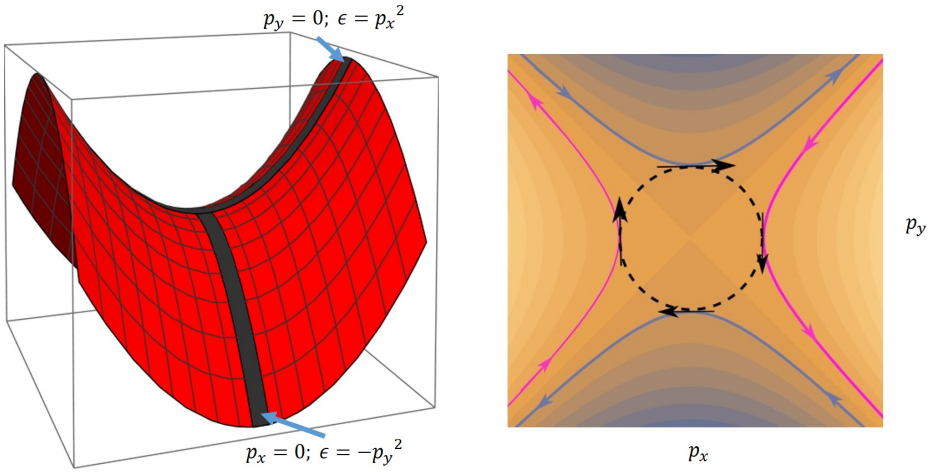

Figure 1.5: Left: Generic saddle point of a band where the dispersion relation is $E \sim p_x^2 - p_y^2$. Right: Color plot of iso-energy lines from the saddle point in the left. Adapted from [21].

magnetic susceptibility close to a saddle point follows the behavior of the density of states, with positive sign. This means, given that the density of states diverges as a logarithmic function, the orbital susceptibility diverges too in the same way. Vignale's formula of the susceptibility close to a saddle point is

$$\chi \sim -\frac{e^2\hbar^2 g(\epsilon)}{12\pi}\left[\frac{\partial^2 E_{\vec{k}}}{\partial \vec{k_x}^2}\frac{\partial^2 E_{\vec{k}}}{\partial \vec{k_x}^2}\right] \tag{1.15}$$

This same result can be obtained via the Landau-Peierls susceptibility, which will be shown later on in chapter 6, when discussing the orbital paramagnetism in a moiré superlattice.

In the case of the saddle point shown in figure 1.5, we can explicitly calculate the divergence of the density of states and the associated orbital susceptibility.

The physical intuitive reason for the existence of these orbits was given by Vignale in terms of magnetic breakdown [18, 31, 32] : the electrons have quasi-classical hyperbolic trajectories that follow the lines of constant energies. When they are close to the saddle point, the probability to tunnel towards another orbit is non-zero. This results in a change of the direction of the rotation and therefore, an inversion of the direction of the magnetic moments. If we consider figure 1.1, the resulting orbital magnetic moment will be paramagnetic.

2 - Monolayer Graphene

Given that all the 2D crystals in our experiments are based on graphene, we will devote this chapter to some of the basic electronic properties of monolayer graphene, specially those needed to understand our experimental results. Then we will talk about graphene in a magnetic field and finally present the results obtained.

Since the experimental realization of graphene in the early 2000s, graphene has become one of the most studied materials. Its popularity may have a variety of origins: form one side, μm-scale graphene is simple enough to obtain to be worldwide spread among condensed matter labs. Due to its structure, graphene present electronic (as well as mechanical and optical) properties that differ from what is known in conventional metals. Last but not least, because of its relative simplicity, the theoretical study of graphene is able to precisely describe the variety of phenomena present.

Electronic properties

A Carbon (C) atom has 6 electrons, with an electronic configuration of the ground state $1s^2\ 2s^2\ 2p^2$. This means that 4 (valence) electrons can participate in the fabrication of bonds. Different allotropes of carbon hybridize these 4 electrons in different way in order to get their crystalline structure. In the case of graphene layers, one of the s electrons is promoted to the p orbital, getting the excited configuration $1s^2\ 2s^1\ 2p^3$. Graphene crystal forms a honeycomb lattice, where each atom of carbon has a bond with 3 other C atoms, separated by 120°. This structure requires that two p orbitals hybridize with the remaining s orbital, forming three sp^2 orbitals in plane that allow C atoms to form the 3 σ bonds per C atom. This lets the the remaining orbital, p_z, perpendicular to the plane, giving one π bond per carbon atom.

Figure 2.1(a) shows the structure of graphene lattice. The figure shows a honeycomb lattice where every circle is a carbon atom. As it is well known, honeycomb lattice is not a Bravais lattice but instead the result of adding two triangular (solid and empty) lattices and shift them to create regular hexagons. It is mathematically equivalent to say it is a triangular lattice with a basis of two atoms. Centered in a carbon atom (sublattice A), the lattice vectors are given by $\vec{a_1} = a\ \hat{x}$ and $\vec{a_2} = \frac{a}{2}\hat{x} + \frac{a\sqrt{3}}{2}\ \hat{y}$ (or equivalent). The second carbon atom of the basis (sublattice B) is located at $\vec{\delta_1} = a_{cc}\ \hat{y}$, where $a = a_{cc}\sqrt{3} = 0.246nm$ is the lattice parameter of graphene and $a_{cc} = 0.142nm$ is the distance between nearest neighbor carbon atoms. The position of the first neighbors is given by the blue arrows in figure 2.1a, given by vectors $\vec{\delta_1} = (\sqrt{3}\hat{x} + \hat{y})a_{cc}/2$, $\vec{\delta_2} = (-\sqrt{3}\hat{x} + \hat{y})a_{cc}/2$, $\vec{\delta_3} = -a_{cc}\hat{y}$.

Reciprocal lattice vectors are given by $\vec{b_1} = (\frac{2\pi}{a}\hat{x} - \frac{2\pi}{a\sqrt{3}}\hat{y})$ and $\vec{b_1} = \frac{4\pi}{a\sqrt{3}}\hat{y}$. Figure 2.1b shows the first Brillouin zone in the shaded area and the thick border.

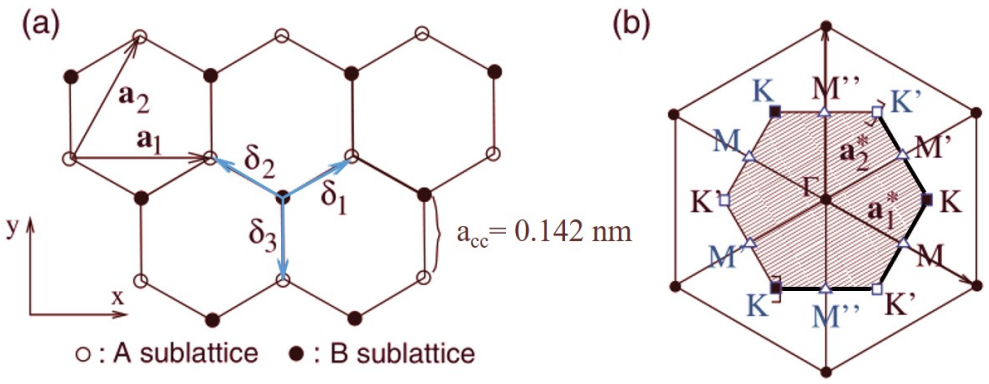

Figure 2.1: (a) Graphene lattice showing the latice vectors a_i, and the positions of the first neighbors δ_i. (b) First Brillouin zone (FBZ) showing the high symmetry points K and M. The thicker edge of the central hexagon belongs to the FBZ. Adapted from [33].

The non-equivalent points K and K' and the 3 non-equivalent M, M', M'' are highlighted. This non-equivalence is related with the nature of the Bravais lattice and the definition of the Brillouin zone.

Now, in order to derive electronic properties, it is necessary to describe graphene with a simple model. For this, let's consider the tight Binding (TB) approximation where electrons are allowed only between hop to nearest neighbors. This calculation was first done by Wallace [34]. This part will only show key points to make the calculation clear but it does not contain all the details. Reference [33] presents a comprehensive solution of the tight biding model.

This section addresses only to the π electrons, which are the ones responsible of the electronic properties at low energy. For these electrons, the TB Hamiltonian is given by:

$$\hat{H}_{TB} = \hat{H}^{atom} + \Delta V \tag{2.1}$$

where $\hat{H}^{atom}$ is the atomic Hamiltonian and ΔV is the correction of the potential due to the other atoms that are in the lattice. We need to solve the Schrodinger equation

$$\hat{H}_{TB}\Psi_{\vec{k}}(\vec{r}) = \epsilon_{\vec{k}}\Psi_{\vec{k}}(\vec{r}). \tag{2.2}$$

We use the test functions considering that we have two atoms per unit cell (A, B):

$$\Psi_{\vec{k}}(\vec{r}) = a_{\vec{k}}\psi^A_{\vec{k}}(\vec{r}) + b_{\vec{k}}\psi^B_{\vec{k}}(\vec{r}) \tag{2.3}$$

where $a_{\vec{k}}$ and $b_{\vec{k}}$ are complex constants and each ψ is a Bloch function of the form

$$\psi^{(j)}_{\vec{k}}(\vec{r}) = \sum_{\vec{R}_l} e^{i\vec{k}\cdot\vec{R}_l}\phi^{(j)}(\vec{r} + \vec{\delta}_j - \vec{R}_l) \tag{2.4}$$

with j indicates the sublattice A or B, vectors $\vec{\delta}$ connects nearest neighbors and ϕ are atomic orbitals that satisfy $\hat{H}^{atom}\phi^{(j)} = \epsilon^{(j)}\phi^{(j)}$, being $\epsilon^{(j)}$ the on-site energy,

which is the same in both sublattices because carbon atoms sit on both. This energy will only represent a constant shift of the Fermi energy and so we will consider equal to 0. Now, to solve equation 2.2, we multiply by the complex conjugate of the wavefunction from the left. Then, writting the Hamiltonian components of the matrix, will give us:

$$\hat{H}^{ij}_{\vec{k}} = \epsilon^{(j)}_{\vec{k}} s^{(ij)}_{\vec{k}} + t^{(ij)}_{\vec{k}} \tag{2.5}$$

where we already have removed the on-site energy, t is the hopping term and s is the overlap of the wavefunctions

$$\begin{aligned} t^{AB}_{\vec{k}} &= \left(1 + e^{i\vec{k}\cdot\vec{a}_2} + e^{i\vec{k}\cdot(\vec{a}_2-\vec{a}_1)}\right) \int d^2 r \phi^A(\vec{r})^* \Delta V \phi^B(\vec{r}+\vec{\delta}_3) \\ &= \gamma^*_{\vec{k}} t = \left(t^{BA}_{\vec{k}}\right)^* \end{aligned} \tag{2.6}$$

By orthonormality of ϕ, $s^{AA} = s^{BB} = 1$. We consider the overlap between orbitals at different sites to be negligible, so $s^{AB} = s^{AB} \sim 0$, and, because we consider only first neighbors hopping, we assume $t^{AA} = t^{BB} \sim 0$. These terms break electron-hole symmetry, but their signature is only important at high energies and do not contribute to the band structure to the Fermi level.

With all these simplifications, we arrive to the effective TB Hamiltonian in the A,B pairs, whose eigenenergies are obtained by solving:

$$\det \begin{bmatrix} \epsilon_{\vec{k}} & -t\gamma^*_{\vec{k}} \\ -t\gamma_{\vec{k}} & \epsilon_{\vec{k}} \end{bmatrix} = 0 \tag{2.7}$$

which yields energy bands:

$$\epsilon^{\lambda}_{\vec{k}} = \lambda\, t \sqrt{3 + \sum_{i=1}^{3} \cos\left(\vec{k}\cdot\vec{a}_i\right)} \tag{2.8}$$

where $\lambda = \pm$ indicating valence (-) or conduction (+) bands, and $\vec{a}_3 = \vec{a}_2 - \vec{a}_1$. When graphene is neutral, the chemical potential is by convention set at $\epsilon = 0$. This is obtained for the wave vectors that make $\gamma_{\vec{k}} = 0$:

$$\vec{k}_{\epsilon_F=0} = \vec{K}_D = \pm \frac{4\pi}{3\sqrt{3}a_{cc}} \hat{x} \tag{2.9}$$

i.e. where the two non-equivalent K, K' points of the reciprocal lattice are located. $\gamma_{\vec{k}}$ is defined by equation 2.6.

Now, it is frequent to use a low energy approximation as most of the experimental results take place at energies that are much smaller than the bandwidth. For this, we must expand the function $\gamma_{\vec{k}}$ around the position of the charge neutrality point (CNP), so the wave vector is written in the form $\vec{k} = \vec{K}_D + \vec{q}$. Taking only the first order in $|\vec{q}|a_{cc}$, we can obtain the low-energy Hamiltonian:

$$\hat{H}^{eff}_{\vec{q},\xi} = \xi \hbar v_F \begin{bmatrix} 0 & q_x - i\xi q_y \\ q_x + i\xi q_y & 0 \end{bmatrix} \tag{2.10}$$

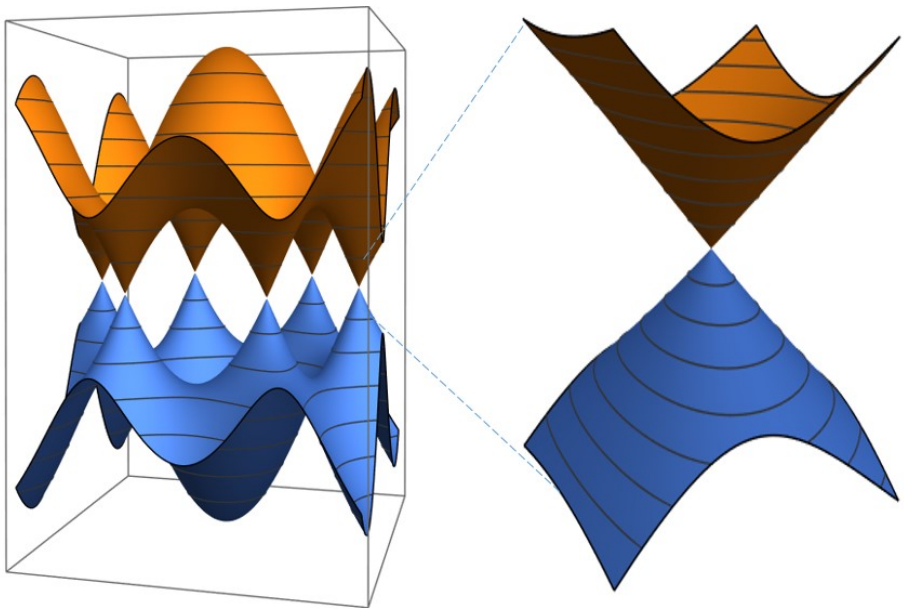

Figure 2.2: Lowest bands of graphene in the tight binding model. In zoom, the contact point between the two bands at the K points, where the Fermi level sits, for undoped neutral graphene.

where $\xi = \pm 1$ accounts for the valley and v_F is the Fermi velocity defined as:

$$v_F = \frac{3ta_{cc}}{2\hbar}. \tag{2.11}$$

The dispersion relation around the Fermi level is then

$$\epsilon = \hbar v_F q \tag{2.12}$$

Consequently, close to the K, K' points, graphene effectively behaves as a system with a linear dispersion relation, electron-hole symmetric and with the valence and conduction band touching in a single point. From this particular dispersion relation the density of states can be calculated:

$$g(E) = \frac{2|E|}{\pi\hbar^2 v_F^2} \tag{2.13}$$

which also follows a linear behavior. As we can see from figure 2.3, the DOS vanishes at the CNP, which by convention is set at $\epsilon = 0$. As mentioned before, it is the same position of the contact points of the linear conduction and valence bands. This is known as the Dirac point. This vanishing DOS gives graphene its well-known resistance maximum as a function of gate voltage. The maximum of the resistance is achieved at the CNP and from there, as electrons get into the conduction band, the resistance drops again, see figure 2.5.

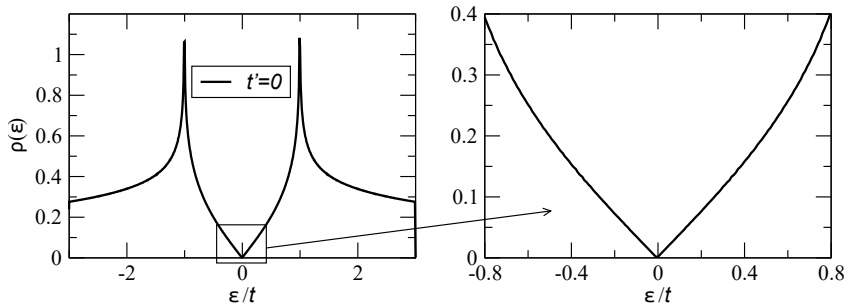

Figure 2.3: Calculation of the density of states (DOS) for graphene in the tight binding model, considering only nearest neighbor hopping, and setting the next-nearest neighbors hopping amplitude as zero $t' = 0$. In the right, a zoom of this plot where the linear behavior of the DOS is evident. Adapted from [35].

By analyzing the lowest energy bands in graphene, we can observe many interesting features present in the bands as well as in the susceptibility. Figure 2.4 shows the susceptibility as calculated in [36], accompanied by the band structure that leads to this magnetic response. In the x axis we show the chemical potential normalized by the hopping parameter t. At charge neutrality, in the K points ($\mu/t = 0$), the linear dispersion and the touching point of the bands is characteristic of graphene. This gives, as consequence, the Dirac-delta diamagnetic divergence (red arrow). At higher doping, at the M point ($\mu/t = 1$), there is a saddle point in the band structure. It is accompanied by a paramagnetic divergent susceptibility (black arrow). At the extremity of these bands, at the Γ points ($\nu/t = 3$), the dispersion relation is parabolic, and then, the limit where electrons behave quasi-freely is attained. Then, the Landau diamagnetism is observed (green arrows).

At the Dirac point then, graphene has a vanishing number of charges and one may expect that the screening of the external magnetic field due to free charges' motion is weak. However, graphite has a well-known large diamagnetic behavior when magnetic field is perpendicular to the plane of the layers. This paradoxical result was already studied theoretically in 1956 [12], where a singular behavior was predicted for the orbital magnetic susceptibility in response to an external magnetic field perpendicular to a single layer of graphene. We can introduce the magnetic field by minimal coupling $\vec{\Pi} = \vec{p} - e\vec{A}$, where $\vec{A} = -By\vec{u_x}$ in the Landau gauge. Then, introducing this in the Hamiltonian 2.10, for the $\xi = 1$ valley we have the Schrodinger equation

$$\hat{H}\Psi = v_F \begin{bmatrix} 0 & \Pi_x - i\Pi_y \\ \Pi_x + i\Pi_y & 0 \end{bmatrix} \begin{pmatrix} \psi_A \\ \psi_B \end{pmatrix} = \epsilon \begin{pmatrix} \psi_A \\ \psi_B \end{pmatrix} = \epsilon\Psi \tag{2.14}$$

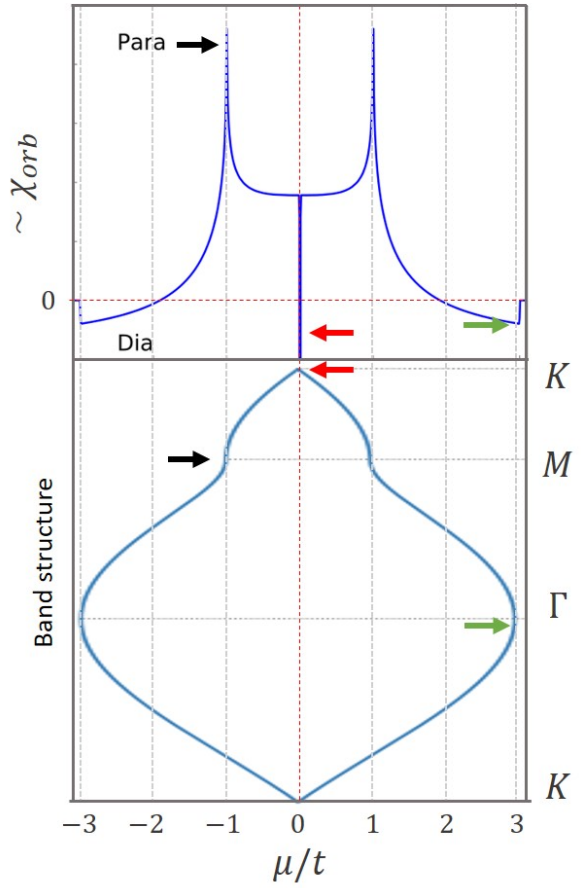

Figure 2.4: Up: orbital susceptibility of graphene in a model of 2 coupled bands calculated in [36]. Down: Band structure of the two lowest energy bands in graphene, calculated with the numerical package pybinding [37]. The black arrows are the points where saddle points appear in the band structure, and the corresponding paramagnetic susceptibility. Red arrows show places of Dirac points with diamagnetic divergences. Green arrows correspond to parabolic bands and Landau diamagnetism.

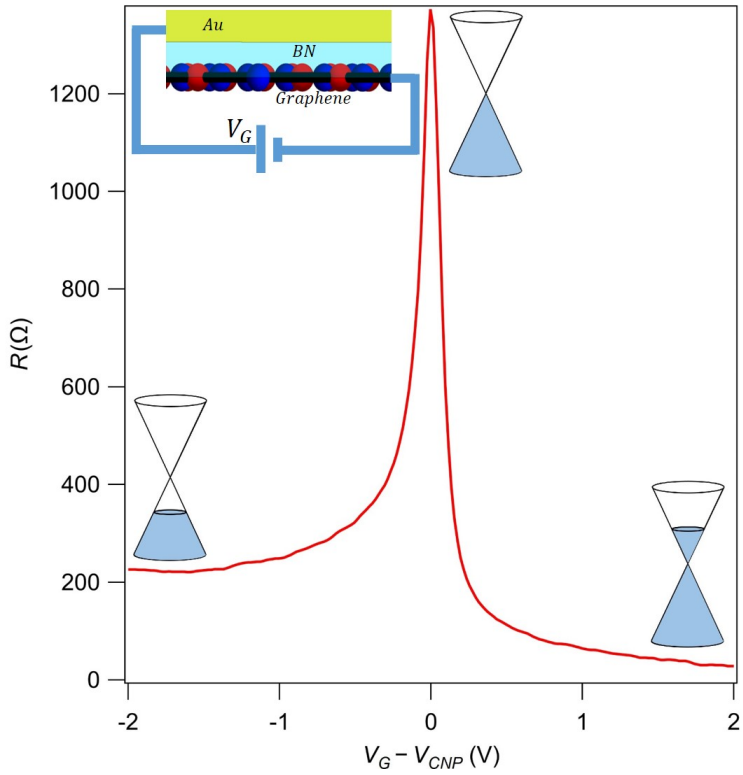

Figure 2.5: The red curve shows the typical behavior of graphene's resistance as a function of the gate voltage. It reaches a sharp peak at charge neutrality point, where the lower band is completely full. The resistance drops fast as graphene is doped with either electrons ($V_g > 0$) or holes ($V_g < 0$). This 3 cases are showed by the cones representing graphene's bands and their filling showing how the chemical potential can be controlled via a gate voltage. The inset of the top part is the schematics of a top gate on graphene. Au electrode and graphene are the two plates of a parallel capacitor, with BN as the dielectric.

[38, 33, 12] which leads us to a system of 2 equations:

$$\epsilon\psi_A = v_F\left(\Pi_x - i\Pi_y\right)\psi_B \tag{2.15a}$$

$$\epsilon\psi_B = v_F\left(\Pi_x + i\Pi_y\right)\psi_A. \tag{2.15b}$$

By substituting one into the other equation, we can decouple them and solve them independently. With a bit of algebra and by the use of the canonical commutation relations, we arrive to independent harmonic oscillator equations

$$\left[(e_0B)^2\left(\frac{\hat{p}_x}{e_0B} + \hat{y}\right)^2 + \hat{p}_y^2\right]\psi_A = \left(\frac{\epsilon^2}{v_F^2} + e_0B\hbar\right)\psi_A \tag{2.16}$$

where $e_0 = -e \simeq 1.6 \times 10^{-19}\mathrm{C}$. Looking at equation 2.16, we can notice that it has a similar shape than an harmonic oscillator in one dimension (y), centered around $\hat{p}_x/e_0B \equiv y_0$.

We can introduce the definitions of magnetic length l_B and cyclotron frequency ω_c' as [33]

$$l_B = \sqrt{\frac{\hbar}{e_0B}} \tag{2.17a}$$

$$\omega_c' = \frac{\sqrt{2}v_F}{l_B} = \frac{v_F\sqrt{2e_0B}}{\sqrt{\hbar}}. \tag{2.17b}$$

These constants are meaningful because in one case the magnetic length defines the limit when the Peierls substitution is valid, this means, as long as the space between atoms is much smaller than $l_B \simeq 23\mathrm{nm}/\sqrt{B(\mathrm{T})}$. In the other case, ω_c' is the equivalent of the cyclotron frequency for relativistic particles. If we multiply equation 2.16 in both sides by $v_F^2/\omega_c'\hbar$, with some algebra and rearrangement of the terms we obtain:

$$\left[\frac{\omega_c'^2}{2}\frac{\hbar}{\sqrt{2}v_f l_B}\left(\hat{y} + y_0\right)^2 + \frac{\hat{p}_y^2}{2}\frac{\sqrt{2}v_f l_B}{\hbar}\right]\psi_A = \frac{v_F^2}{\omega_c'\hbar}\left(\frac{\epsilon^2}{v_F^2} + e_0B\hbar\right)\psi_A \tag{2.18}$$

Now this equation has the exact same form of the 1D harmonic oscillator, ψ_A are eigenfunctions of the harmonic oscillator and the eigenvalues of the energy are $\lambda_n = \hbar\omega_c'(n + 1/2)$. Then, the right part of 2.18 leads to

$$\epsilon_n = \mathrm{sign}(n)\sqrt{2v_F^2\hbar B e_0|n|} \tag{2.19}$$

where n is the Landau level index and can take any integer number, including zero. Their degeneracy per unit area is given by $4eB/h$, where the factor 4 considers the spin and valley degeneracies.

The 0^{th} level is precisely the reason why graphene is strongly diamagnetic. The qualitative argument for this diamagnetism can be seen as follows: because of equation 2.13, we know that the states are distributed linearly and continuously

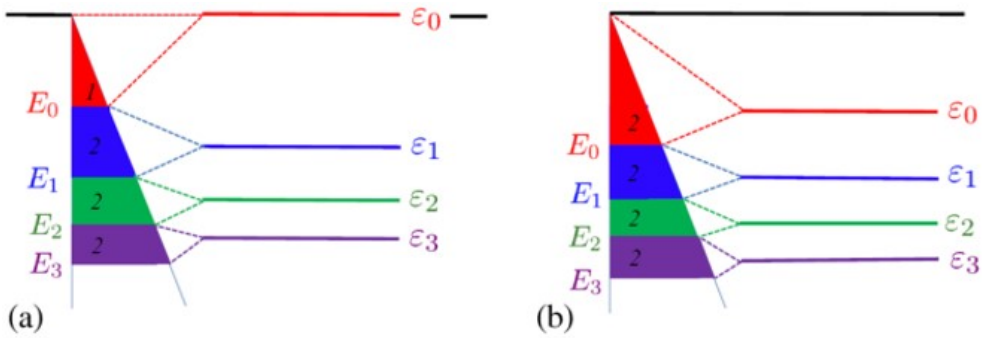

Figure 2.6: The continuous distribution of states in zero field coalesce to form the Landau levels spectrum. For graphene in (a), we notice the formation of a level at zero energy, which is absent for the Dice model in (b). Taken from [19].

when there is no magnetic field. Once the magnetic field is on, groups of states coalesce to the average energy of the group, see 2.6. The $n = 0$ level is shared between valence and conduction bands but the later are empty, so the levels in the valence have to increase their energy to form this Landau level, therefore, the magnetic response will be diamagnetic, repelling the external field. To show the importance of this level, McClure calculates an estimation to the contribution of the condensation of the states into the 0^{th} Landau level to the susceptibility [12]. Although the exact value is slightly different, it let us have a very close approximation. At zero field, the total energy of this group of electrons is

$$E = \int_{-E_0}^{E_0} g_0(\epsilon) f(\epsilon) \epsilon d\epsilon \tag{2.20}$$

where g_0 is the density of states given by 2.13, f is the Fermi-Dirac function and E_0 is the energy of the limit of the group of electrons that will populate the $n = 0$ level (see figure 2.6). The value of E_0 is obtained by equating the degeneracy of the level with the integral of the density of states up to that point. Because the density of states is linear, the integral is the area of a triangle with base E_0 and height $g_0(E_0)$. Then, because the $n = 0$ level is equally shared between electron and hole states, this area accounts only for half of the degeneracy in the level:

$$\frac{1}{2} E_0 \frac{2E_0}{\pi \hbar^2 v_F^2} = \frac{1}{2} \frac{4eB}{h} \tag{2.21}$$

from where

$$E_0 = v_F \sqrt{e\hbar B}. \tag{2.22}$$

If the energy scale associated to the magnetic field, $\epsilon_B = \sqrt{2ev_F^2 \hbar B}$, is small compared to the thermal energy, $k_B T$, then we can expand $f(\epsilon)$ to first order and

write:

$$E \simeq \frac{4}{\pi\hbar^2 v_F^2}\int_0^{E_0} \epsilon^3 f'(\epsilon=0)d\epsilon. \tag{2.23}$$

The change in energy produced by the field is $-E$ because the energy of the level 0 is exactly zero. Then, by neglecting the change in entropy (which is a rough approximation), the susceptibility in the limit $kT >> \epsilon_B$ is:

$$\chi_{n=0} \sim -\frac{\partial^2 E}{\partial B^2} \propto -\frac{e^2 v_F^2}{\pi}\frac{1}{k_B T}\text{sech}^2\left(\frac{\mu}{2k_B T}\right). \tag{2.24}$$

The maximum value of this function is at $\mu = 0$. χ_0 gets sharper and bigger as T gets smaller, and the limit is $\delta(\mu)$ when $T \to 0$. This χ_0 is an overestimation but it is of the same order of magnitude than the exact calculation, differing by a factor $2/3$ from the exact value due to the assumptions made before. What is important from the message given by McClure is that the large diamagnetism is due to the existence of the $n = 0$ level. The fact that this level is shared between valence and conduction band allows for the possibility of interband transitions and the fact that the diamagnetism is large is due to their very low effective mass (in fact they behave as massless particles).

In the limit when the temperature and chemical potential are zero ($T = 0$, $\mu = 0$), we can estimate the change of energy associated to this first region λ in a similar way. In this case, $f(\epsilon) = 1$ for the occupied states ($\epsilon < 0$) and then, the integral 2.20 becomes

$$\Delta E = -\int_{-\lambda}^{0} g_0(\epsilon)\epsilon d\epsilon = \frac{2}{3\pi\hbar^2 v_F^2}\epsilon^3 \Big|_{-\lambda}^{0}. \tag{2.25}$$

From equation 2.25 we obtain the magnetization:

$$M = -\frac{\partial \Delta E}{\partial B} = -\frac{v_F e^{3/2}}{\pi\sqrt{\hbar}}\sqrt{B} \tag{2.26}$$

which allows us to recover the $\sqrt{B}$ dependence of the magnetization, characteristic of graphene. Again this is an overestimation (by a factor 2 approximately) but it shows the importance of the zero level.

The existence of this $n = 0$ level can be seen equivalently as a consequence of the Berry phase of π in graphene, which can be understood by the following argument: The semiclassical Onsager's quantization rule [39] fails to recover the exact distribution of the Landau levels in graphene. This rule is the condition for a semiclassical wavefunction to have a single value. It states that when an electron moves around its cyclotron orbit, the total stationary phase accumulated is zero modulo 2π [40]. In a semiclassical approximation, only the spatial and Aharonov-Bohm phase contribute. In the case of graphene, the problem is the absence of the 0^{th} level even though the $(nB)^{1/2}$ law for Landau levels is present. However, a correction of this quantization rule can be done in order to solve this problem.

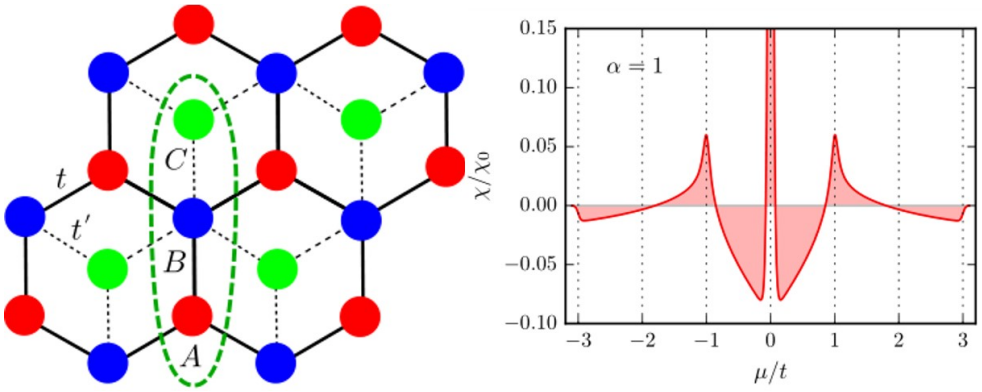

Figure 2.7: (Left) diagram of the dice lattice showing the 3 atoms per site whose . (Right) Numerically calculated orbital susceptibility of the dice lattice for a temperature $k_BT = 0.01t$. At $\mu = 0$, χ is divergent and paramagnetic. Adapted from [21].

Kohn [41] and later Roth [42] proposed a generalization of Onsager's rule in order to determine both the steady susceptibility and the de Haas-van Alphen oscillations in Bloch's electrons. By taking the next term in the expansion series of the energy as a function of magnetic field, the quantization condition is given by:

$$A_n = \pi k_n^2 = \left(n + \frac{1}{2} - \frac{\Phi_B}{2\pi}\right)\frac{2\pi eB}{\hbar}. \tag{2.27}$$

where each energy level, n, describes a semiclassical orbit with area A_n. Φ_B is the Berry phase acquired by the motion around the orbit. In the case of open orbits, it has the value of 0. For graphene, it is equal to π. By inserting 2.12 in 2.27, we are able to recover 2.19.

If the Berry phase is zero, however, the Landau spectrum is

$$\epsilon_n = \sqrt{2ev_f^2\hbar B\left(n + \frac{1}{2}\right)}. \tag{2.28}$$

It was shown in reference [19] that for a system whose Landau levels follow 2.28, the orbital susceptibility is still singular at the charge neutrality point, but the sign of the singularity is positive. This means that it is paramagnetic instead of diamagnetic. We see in figure 2.7 the $\mathcal{T}_3$-lattice (or dice) model. This is a triangular lattice with 3 atoms per lattice site. The distribution of Landau levels is given by equation 2.28. This subtle but important change inverts the sign of the divergence of the susceptibility, which now behaves as $\chi_{Dice} \sim +\delta(\mu)$.

The exact calculation of the susceptibility of graphene in the presence of disorder, magnetic field, as a function of temperature and chemical potential needs a bit of attention and the main steps to get it will be given in next chapter 5, as part of the results obtained by our collaborators and presented in [17].

However at this point we can make some comments about graphene's susceptibility. As it was mentioned earlier, McClure already found that in the limit where $T \to 0$, the susceptibility takes the form of a Dirac delta function of the chemical potential $\chi_{orb} \sim -\delta(\mu)$. This leads to a surprising result: the orbital magnetic susceptibility, at vanishing magnetic field, diverges at the charge neutrality point. But, the density of states at CNP in graphene is zero. Now, a paradoxical conclusion appears: at CNP there are no carriers that can make opposition to the external magnetic field, nevertheless, graphene's orbital magnetic susceptibility diverges!

In the words of McClure, the diamagnetic characteristic of this susceptibility is due to the degeneracy of the Fermi level and the existence of the interband terms in the tight binding Hamiltonian of graphene. This is nowadays resumed as the contribution of the π Berry phase [21]. The fact that susceptibility diverges is related to the ultra-relativistic nature of electrons in graphene, in simpler words, their linear dispersion relation [12, 19].

3 - Giant magneto-resistance (GMR) sensors

One of the main goals of this project was to measure the orbital magnetization of graphene and graphene-based 2D materials. As it was mentioned before, the orbital magnetic moment of a 2D crystal is expected to vary linearly with the applied external field. Then, the higher the external field, the larger the amplitude of the response signal, but also the undesired effects of the external field in the measurement become more important and harder to subtract. In addition, we must be sure that we can discriminate the signal from our sample from all the other magnetic contributions originating from external magnetic fields, electromagnetic radiation, impurities in the substrate or sample, or even magnetic contributions intrinsic to the sample that do not have the same nature, for example magnetic impurities from vacancies or defects. This is the reason why, it is necessary to ensure that only the magnetic signal coming from the orbital currents in the crystal is measured.

Another experimental difficulty that we have faced during this project is evident: the amplitude of the orbital magnetization of a single graphene flake is expected to be small. Using equation 1.13, mentioned in the previous chapter, one can estimate the order of magnitude of the susceptibility. At $T = 4\mathrm{K}$ and for a small external field, the orbital current expected is of about $10\mu\mathrm{A}$, in the absence of disorder. If we consider this current as a classical cyclotron orbit (to simplify), the magnetic field it produces is of the order of $1 - 10\mathrm{nT}$, at $1\mu\mathrm{m}$. This field is co-linear and anti-parallel to the external field that generates this response. Then, the signal we search is a correction of 10^{-7}-10^{-8} times the external field, in the best case scenario. This means that very sensitive probes are needed and which are usually limited by the range of operation of external field. (Later in this chapter, section 3.6, we will briefly mention the other probes that have been tested).

3.1 . GMR detectors

The probes that we chose to measure the magnetic response of the 2D materials studied are GMR probes. The magnetoresistive material of the GMR detectors consist of a multilayered material that contains ferromagnetic layers separated by non-magnetic layers with a large enough spin diffusion length, l_{SD} [43], which is the mean distance along which electrons can diffuse between spin-flipping events [44]. These layers are sufficiently thin to ensure negligible leakage fields. The GMR effect is based on the variation of conductivity in these multilayered ferromagnetic materials according to the relative orientation of the different layer's magnetization.

This effect was discovered in the late 1980 by the works of Fert and Grunberg [45, 46]. They observed a high change in the resistance of a ferromagnetic multi-layer device when the magnetization of these layers where brought into alignment

using an external magnetic field. Fert and Grunberg were awarded the Nobel prize in 2007 for their discovery, as it was one of the fundamental ideas behind the development of spintronics, field that has been extensively studied both theoretically and experimentally through these years. For example, the advances in this field has led to the improvement of the technology used for the reading of hard disks and for designing new methods for mass storage devices. In the heart of spintronics is the idea that electrons have the spin degree of freedom (that is quantized) and, through imposed conditions, can be manipulated to achieve control over their transport. For example, in magnetic materials, the spin of conducting electrons is polarized depending in the characteristics of the crystals and so magnetic scattering will be favored or not depending on the spins of electrons in an injected current. This is the idea behind the GMR devices.

Perhaps the easiest way to understand the magneto-resistance phenomenon in multilayered materials is by looking in figure 3.1A at the current perpendicular to plane geometry (CPP). Most of the applications of these devices in standard technology use the CPP configuration, for example hard disk drives. Following the direction of the current, the spin of the conduction electrons is polarized according to the direction imposed the magnetization of the pinned ferromagnetic layer (green). Then, electrons travel through a non-magnetic material (orange spacer layer) without magnetic scattering if l_{SD} is big enough. Afterwards, electrons go through the free ferromagnetic layer (blue). They will find it easier to enter in this second layer if the orientation of both magnetic layers is the same. From this basically general idea, we can expect that the resistance of the device will strongly depend on the relative angle between the hard (pinned) and soft (free) layers. Understanding this geometry in a theoretical model is relatively simple because the multilayer can be modeled as a series of resistors whose values change according to the relative alignment of the magnetic layers. For a detailed description of of this CPP geometry, we can see the corresponding section in reference [47].

GMR devices can also have a geometry similar to the one showed in figure 3.1B, where the current flows in parallel with the layers. This geometry is known as current in plane (CIP), and it is the one used in our experiments. In CIP configuration, the current flows parallel to the layers and electrons go through both magnetic layers and the spacer successively and repeatedly, with the condition that the layers are sufficiently thin. Thus, in order for this configuration to exhibit a sizable GMR behavior, there is an optimal thickness of the spacer which should be thin enough in order that the electrons can travel easily between the magnetic layers, but also thick enough in order that the coupling between ferromagnetic layers is not too high.

CIP mode can be modeled then as a small correction to the conductance. One can consider the conductance of all layers in parallel and add the contribution of the interfaces of magnetic layers in the transport of the electrons. They generally have a structure $(F/NM)_n$, which is made by stacking n times a layer of ferromagnetic

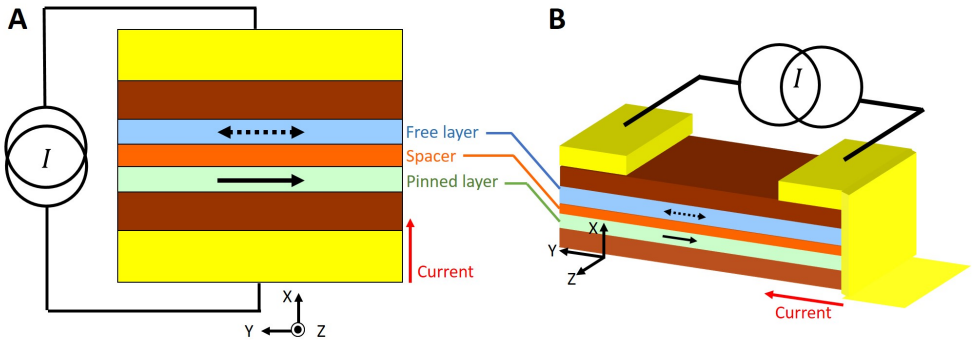

Figure 3.1: (A) Diagram of a spin valve device. In this geometry the current flows perpendicular to the plane of the layers (CPP) following the x axis (red arrow). (B) Diagram of a current in plane (CIP) geometry. Current flows in parallel with the plane of the layers following the y axis (red arrow). This is the geometry of our probes.

transition metal layer, F, in contact with a non ferromagnetic metal NM. Then, the whole stack is connected by the sides, as represented in figure 3.1B. In the following, we present a very brief description of the model derived in [48]. It allows to understand the GMR effect in the CIP geometry.

3.2 . CIP in a nutshell

In 1989 Camley and Barnas [48] proposed the first model in order to explain the changes in resistance observed in Fe/Cr layered structures, that was previously reported by Grunberg [46]. This model is based on the Fuchs-Sondheimer [49] theory of the conduction in thin films of metals. From a semi-classical approach, this model solves the Boltzmann equation for conduction quasi-free electrons by considering each spin species as independent. This is known as the two current model, where the total current density, $\vec{J}$, can be decomposed into two independent contributions, one for each spin.

$$\vec{J} = (\sigma_{\uparrow} + \sigma_{\downarrow})\,\vec{E} \tag{3.1}$$

where $\sigma_{\uparrow,\downarrow}$ are the conductivities for spin up and down respectively and $\vec{E}$ is the electric field. By neglecting the effects of magnetic fields on the conduction, the Boltzmann equation is:

$$-\frac{e}{m}\vec{E}\cdot\vec{\nabla}_v f + \vec{v}\cdot\vec{\nabla}_r f = -\frac{f - f_0}{\tau} \tag{3.2}$$

which relates the rate of change in f, the electrons distribution function, due to external fields, $\vec{E}$. f is the out-of-equilibrium, local, time-dependent Fermi-Dirac distribution of electrons in the material, in the presence of an electric field,

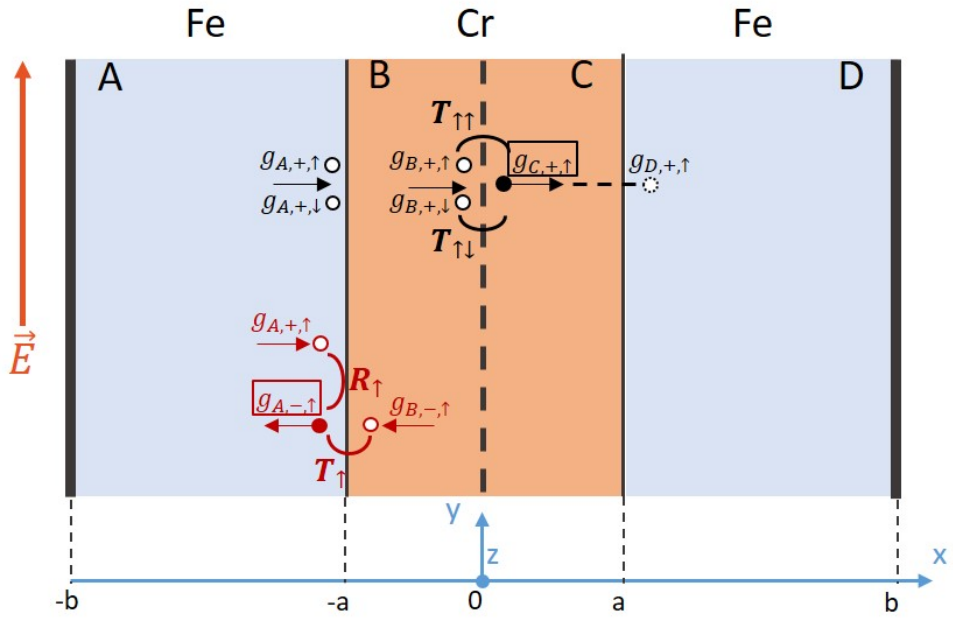

Figure 3.2: Fe/Cr/Fe multilayer in CIP configuration, the first generation of GMR devices. It is also the basic system that is analized by [48] in their model. In the figure, the equations 3.7 (red) and 3.8 (black) are shown schematically. Subindices $+, -$ refer to the velocity of the electrons along the x axis, i.e., $v_x > 0$ and $v_x < 0$, respectively. Subindices $\uparrow, \downarrow$ refer to the spin of the electrons along the z axis.

($f = f(\vec{r}, \vec{v}, t)$). τ is the relaxation time related to collisions and f_0 is the Fermi-Dirac equilibrium distribution function.

In a thin film whose thickness grows in the x direction, one can write f as

$$f = f_0 + g(\vec{v}, x), \tag{3.3}$$

where g is a small correction to the equilibrium, and so Boltzmann equation reads:

$$\frac{\partial g}{\partial x} + \frac{g}{\tau v_x} = \frac{eE}{m v_x} \frac{\partial f_0}{\partial v_y}, \tag{3.4}$$

where the electric field has been chosen along in the y direction, parallel to the layers, as it is in a CIP geometry.

At this point, g can be separated into different regions in space and adding the contributions of each spin species up or down (note that the defined regions are not the same as layers, as there are 4 regions for 3 layers). Thus, in **A** region, g has the form

$$g_{A,\pm,\uparrow} = \frac{eE\tau}{m} \frac{\partial f_0}{\partial v_y} \left[1 + A_{\pm,\uparrow} \exp\left(\frac{\mp x}{\tau |v_x|} \right) \right]. \tag{3.5}$$

Where the $\pm$ indicates the sign of the velocity of electrons in x and the arrow indicates the spin. Coefficients $A_{\pm,\uparrow}$ need to be determined by the boundary conditions of the layers and so we could calculate the current density originating from g as:

$$\vec{J}(x) = \int v_y g \; \vec{dv}. \tag{3.6}$$

At the interfaces, electrons can be transmitted with probability T or reflected with probability R, except at the outermost boundaries where electrons cannot escape so they will be perfectly reflected. As it is shown in figure 3.2, $g_{A,-,\uparrow}$ (which refers to electrons in region **A** with spin up and moving to the left $v_x < 0$), is affected by electrons coming from neighboring region **B** with same spin $\uparrow$ and velocity $v_x < 0$, and by electrons in the same region **A** with the same spin $\uparrow$ but opposite velocity $v_x < 0$ who reflect on the interface located at $x = -a$. For this boundary, we can write:

$$g_{A,-,\uparrow} = T_\uparrow \; g_{B,-,\uparrow} + R_\uparrow \; g_{A,+,\uparrow} \tag{3.7}$$

and similarly for the other boundaries, spins and velocity directions.

We can also wonder about electrons that start in one Fe layer and arrive to the next Fe layer, from region **A** to **D** or vice versa. Here we need to consider that the magnetization of the two layers may or may not be different, and so, an electron with spin up in the regions **A** and **B**, can be *seen* as an spin down in the regions **C** and **D**. This is not really a flip of the spin but instead a change in the direction of the quantization of the spin. In the model of Camley and Barnas, they place the $x = 0$ line as the point of this change of the direction of the quantization. In this case, it is necessary to take into account this possibility by adding coefficients of transmission up-up $T_{\uparrow\uparrow}$, down-down $T_{\downarrow\downarrow}$, up-down $T_{\uparrow\downarrow}$ or down-up $T_{\downarrow\uparrow}$.

As an example of the boundary conditions that we need to consider, we can focus on the region **C** at $x = 0$, according to figure 3.2 (red diagram). The distribution of electrons with spin up moving to the right is composed by the electrons coming from **B** (here there is no reflexion as $z = 0$ is not a real boundary). From one side, those electrons who have spin up, related to **A** region, and continue having the same direction respect to **D**. From the other side, spin downs in **A** region that are spin up respect to **D** region

$$g_{C,+,\uparrow} = T_{\uparrow\uparrow}\, g_{B,+,\uparrow} + T_{\uparrow\downarrow}\, g_{B,+,\downarrow} \tag{3.8}$$

where this double-transmission probabilities are dependent on the angle between the magnetization of Fe layers θ

$$\begin{aligned} T_{\uparrow\uparrow} &= T_{\downarrow\downarrow} = \cos^2(\theta/2) \\ T_{\uparrow\downarrow} &= T_{\downarrow\uparrow} = \sin^2(\theta/2), \end{aligned} \tag{3.9}$$

which will be determined ultimately by the external magnetic field B_{ext}.

To simplify the model and reduce the number of parameters in this already large set of equations, reference [48] assumed that there is no reflection at the inner interfaces of the multilayer, by considering the metals to be identical except for the magnetization, then all coefficients of reflexion are zero $R = 0$. This will greatly simplify the model making it depend only on three parameters: $T_\uparrow$, $T_\downarrow$ and of course $\theta(B_{ext})$. Once all the coefficients are obtained, the correction to the current can be calculated as a sum of two parts of different spins, and then added to the current given by the equilibrium distribution function. Although these simplifications seem rough, the model in [48] showed it is possible to capture the essence of the behavior of the magnetoresistance of the multilayer, as it is shown in figure 3.3.

The system studied in reference [48] is the multilayer used in [46] Fe/Cu/Fe. At zero magnetic field, the magnetization direction of the Fe layers is antiparallel. The magnetic field is applied along the easy axis of the stack, which is in plane, perpendicular to the direction of initial magnetization of the Fe layers.

Then, when both Fe layers have anti-parallel magnetization vectors, spins arriving to a layer of opposite magnetization orientation will have an extra energy and thus, they will relax by magnetic scattering events, producing a high resistance.

In the opposite case, when layers have parallel magnetization vectors, $\theta = 0$, the transmission for the majority of the species of spin is favored $(\cos(0) = 1)$ as it is aligned with the magnetization, producing a decrease in resistance. In figure 3.3, this regime is reached with high magnetic fields where the relative change in resistance is the lowest.

More sophisticated models have been proposed where it is explicitly taken into account in the calculations the difference in the mean free path of the spin species and between layers, for example [50]. Nevertheless, they maintain the idea of explaining the GMR effect through the coexistence of 2 currents of opposed spin

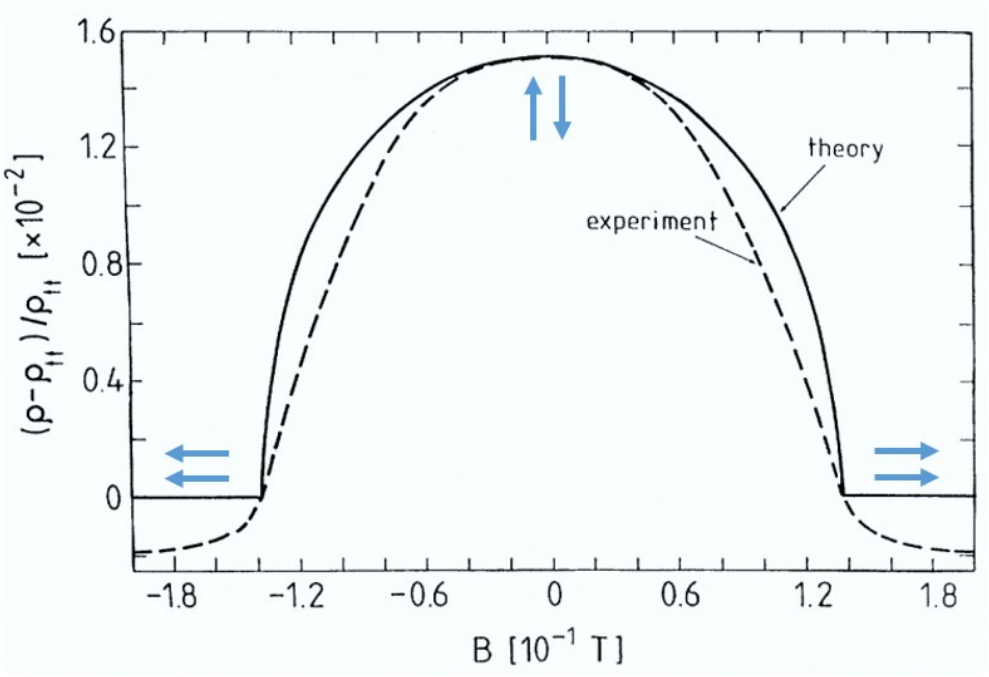

Figure 3.3: The results of the model of Camley and Barnas. The qualitative characteristics of the behavior of the change in resistance as a function of the field is captured. In the theoretical model and the experimental results (from [46]), the magnetization vectors of the Fe layers are antiparallel at zero magnetic field B_{ext} (antiferromagnetic coupling given by the thickness of Cu). By increasing the horizontal magnetic field, the magnetization of both Fe layers align with the direction of B_{ext} and then the resistance decreases to a minimum. The blue lines show the direction of the magnetization of each Fe layer. Adapted from [48].

that conduct in parallel, and whose difference can be attributed to the different transmission probabilities of each spin into a new layer, and that is also dependent on the angle between the direction of the magnetizations. But the purpose of this part is just to have a simple picture of the quantities that are involved and the origin of the GMR phenomena, to not treat our probes as mere black-box-transducers.

To summarize the functioning of the GMRs, the resistance of the multilayer can be seen as a constant part that is modified by a small correction dependent on the magnetic field. This small resistance correction changes according to the angle between the magnetization vectors of the layers. In this spirit, to take advantage of these effect, the magnetization of one of the layers can be pinned to one specific direction. Then, by applying a magnetic field that makes the soft layer aligned to the pinned one, the resistance of the device will be reduced. If the magnetic field makes the layers to be antiparallel, then the resistance will increase. This has been done in the probes we use. We can compare the results of the model and experimental results shown in figure 3.3 to the behavior of our sensors. If we consider only half of figure 3.3 (negative magnetic field up to zero), the behavior is the same we can observe in figure 3.5. By contrast, once we completely anti-align our GMRs, we saturate the resistance and we cannot see the decrease shown for positive fields in 3.3. The reason is that our probes have a pinned layer whose coercitivity is much larger than the applied external fields.

Our probes measure the orbital magnetization by detecting the stray field of graphene's orbital currents when they are present, changing the resistance of the device as a function of graphene's doping.

3.3 . Fabrication

The GMR probes we used were fabricated by Claude Fermon, Myriam Pannetier-Lecoeur and Elodie Paul, from SPEC-CEA. These sensors consist of a stack deposited by sputtering over a 300 μm-thick silicon substrate. It has the following composition as given in the suplementary materials of [17]: Ta (3 nm) / NiFe(5 nm) / CoFe (2.1 nm) / Cu (2.9 nm) / CoFe (2.1 nm) / Ru (0.85 nm) / CoFe (2nm) / IrMn (7.5 nm) /Ru (0.4 nm) / Ta (5 nm). The pinned layer is composed of the antiferromagnet IrMn coupled to a synthetic ferromagnet (CoFe/Ru/CoFe); on the other hand the soft layer is made of the CoFe/NiFe bilayer.

After the GMR stack deposition, an oven-annealing step at 1 T and 180 °C is performed to set the magnetization direction of the hard layer. The GMR sensors (3 $\mu\mathrm{m}$ wide and 20 $\mu\mathrm{m}$ long (in their active region), see figure 3.4) are defined by optical lithography and ion beam etching. Contacts consist of a Ti(10 nm)/Au (100 nm) bilayer deposited by evaporation. The resistance of the contacted GMR is 150 Ω at $4\mathrm{K}$. The sample is then protected by a ~ 900 nm-thick Al_2O_3 passivation layer, deposited by sputtering, that not only protects the probes, insulates them from the rest of the sampl and also, it allows to position graphene at an optimum

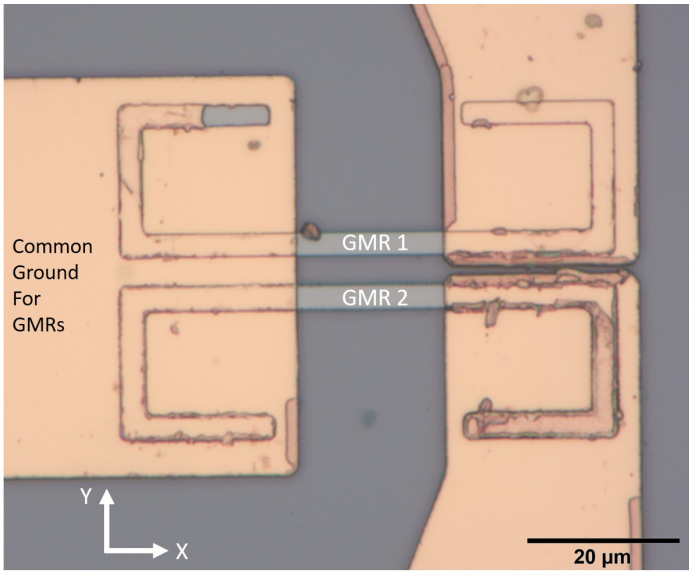

Figure 3.4: Optical image of the sensors. The central zone is where the BN/graphene/BN stack is going to be deposited, centered in between the two GMR stripes. The polarization current flows through each stripe to the common electrode, from right to left in the picture. The most sensitive direction is perpendicular to the long axis of the stripes, along the y axis.

height to maximize sensitivity. An image of the central zone of the probes on a chip is displayed in figure 3.4.

3.4 . Suppressing external fields

3.4.1 . Wheatstone bridge configuration

Once we understood the very basics of how our sensors work, the next challenge is to ensure that this high sensitive probes are only measuring the field generated by the orbital response of graphene. As it was mentioned in the previous section, GMRs will react to any horizontal magnetic field. It is necessary then to suppress all the spurious external fields. This is cleverly done by putting two GMRs parallel to one another and measuring the difference between their resistances. In this configuration, the contributions of magnetic fields which are identical on the 2 probes cancel each other. For example, one can be affected by macroscopic sources of electromagnetic radiation, for example, the earth's magnetic field, external magnetic noise from neighboring equipment, if we use only one GMR. But by subtracting the same background from the neighbor probe, we are not sensitive to this background. For the same reason, the field that are opposed in each of the GMRs add to one another. This is exactly what happens with the field generated

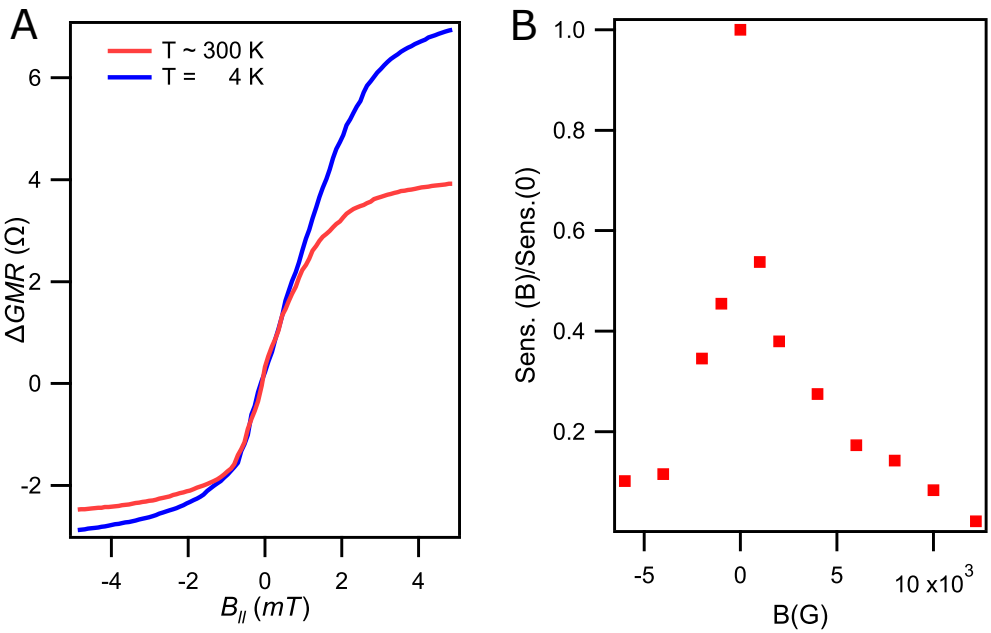

Figure 3.5: A shows the change in resistance of one GMR alone with horizontal field and B shows the relative change of sensitivity when the vertical field is not compensated. This loss of sensitivity (to compare with figure 3.8) is mainly due to the residual in-plane projection of the external field [17].

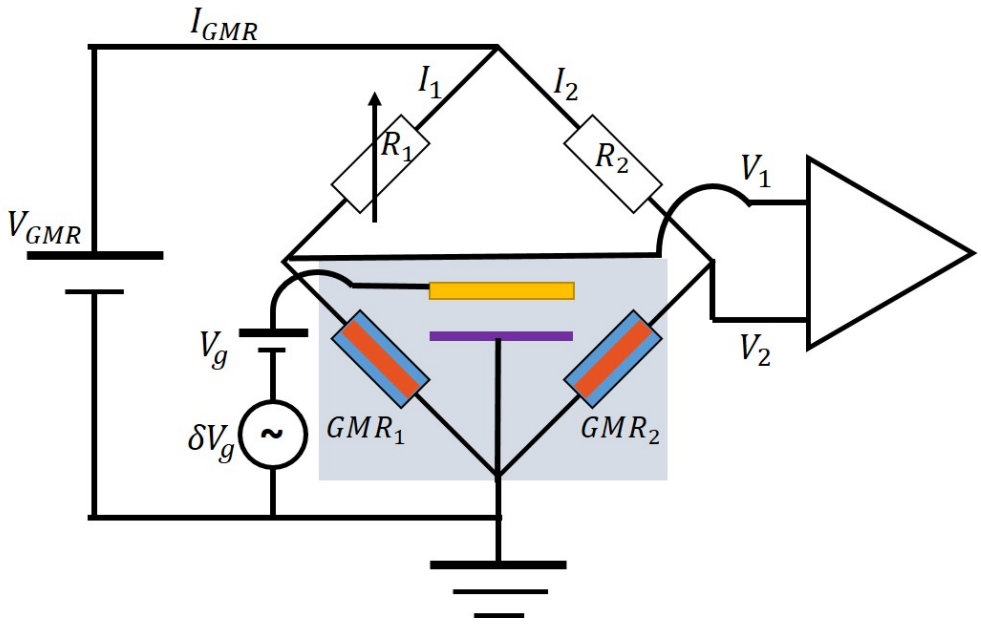

Figure 3.6: Diagram of the circuit used for the measurements. In the center, the Wheatstone bridge showing the set up for the connections of the GMRs. This set up allows for the system to remove the influence of external magnetic fields by tuning R_1 and R_2, polarization resistances, to get $\Delta V = V_1 - V_2$=0, when $B_{perp} = 0$. The purple bar represents graphene and the yellow is the gate electrode. The shaded gray area is the part of the circuit at low temperature, tipically $4\mathrm{K}$.

by the gated part of graphene, which lies in the middle of the two GMRs and because it is symmetric to the middle point of the GMRs, it has different sign in each one, so the measured graphene orbital field is doubled. But this is not the end of the story: we must be sure that the sensors report a zero value when they are in zero magnetic field and that they will respond in an equal way to magnetic field. For this, the first thing to do is to assure that the difference in the drop of tension in each GMR is zero, in other words we require $R_1 I_1 - R_2 I_2 = 0$. This is achieved by connecting the GMRs in Wheatstone bridge configuration as it is depicted in figure 3.6. The objective is to modify the resistance in the variable resistor (potentiometer) in a way that the potential drop at GMRs A and B are identical when there is no magnetic field.

3.4.2 . Compensation

When the perpendicular external field is applied, then it is necessary to take into account the misalignment between the direction of the field and the direction perpendicular to the plane of the GMRs. In an ideal situation, both directions coincide but in practice, these two directions do not exactly coincide. To com-

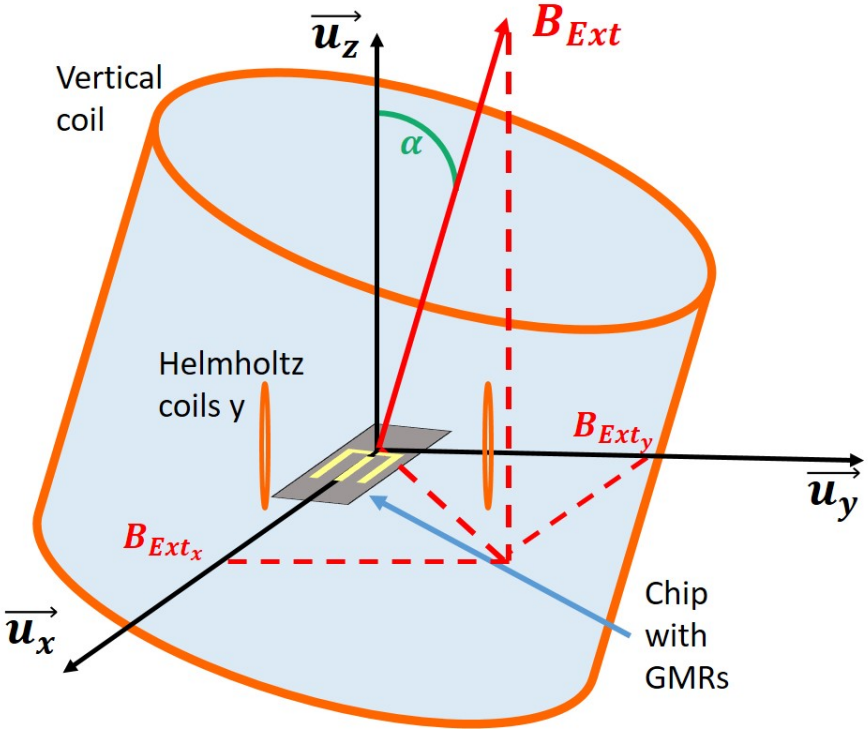

Figure 3.7: Schematics of the set up used to apply the external magnetic field. The horizontal Helmholtz coils cancel the horizontal projection of the external magnetic field.

pensate for the projection of the external field in the horizontal plane, two pairs of Helmholtz coils are placed along the x and y directions, see figure 3.7. We increase adjust the currents in the x and y coils while simultaneously measuring the sensitivity of the probes. We know in-plane components of the external field alter the value of the sensitivity only when the probes are out of its linear regime, which occurs at a few mT in the most sensitive direction (transversal, y in figure 3.4,3.7) as shown in figure 3.5 (the sensitivity along the longitudinal direction is $1/10$ of the transversal one). As figure 3.8 shows, there is also loss in sensitivity with the perpendicular magnetic field. This is due to some domains starting to align with the perpendicular direction when it is sufficiently strong, and thus, not participating in the correction to the conductivity part described in section 3.2. This loss of sensitivity is intrinsic to the design of experiment and there is nothing we can do about it, except for estimating its value from figure 3.8 and adding as a factor in our results.

3.5 . Sign determination

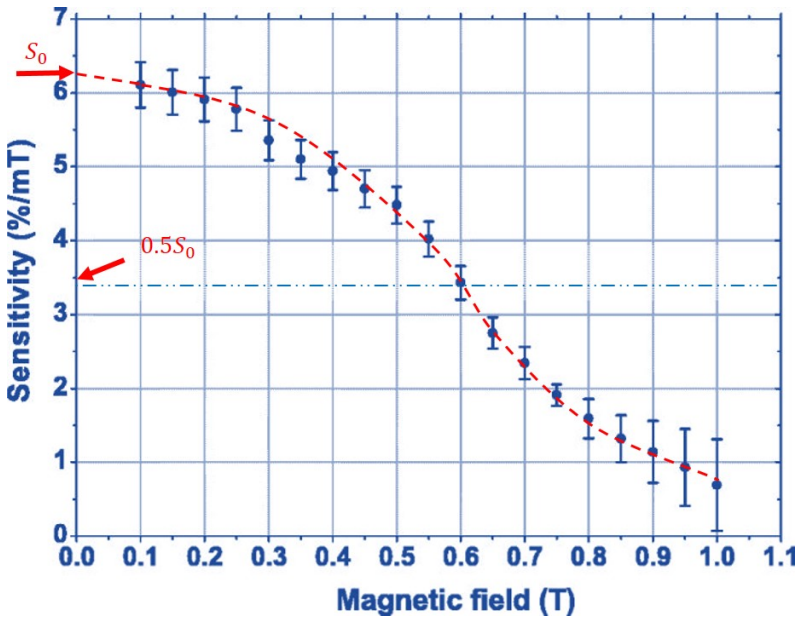

Figure 3.8: Variation in the sensitivity of a GMR device as a function of perpendicular magnetic field. As reference, points where the maximum sensitivity $B = 0$ and half of the sensitivity $B \sim 0.6T$ are highlighted, as well as a rough tendency of this variation. Plot adapted from [51].

If we want to determine the nature of the magnetic response, we must pay extreme attention to the sign of the response. If these curves are indeed showing the McClure peak, they must be diamagnetic, this means, to oppose the magnetic field. In this regard, the sign of these curves relative to the external field must be determined independently. The procedure is easier to do than to explain, but here is the description of how it was done:

- Fix the sign of the external magnetic field. This is easily done using the convention of the power source: positive sign will be the one created by a positive current.

- Determine the spatial orientation of this positive external field. With the help of the magnetometer in a smartphone, we can know whether our positive field points in +Z or -Z direction. In this case, let's assume positive field points to +Z direction. It is shown by the vertical red arrow in figure 3.9.

- We can use this knowledge to apply a known horizontal field to each of the GMRs independently, in this case, let's focus on the right GMR in figure 3.9. The idea is to know how will the GMRs respond to a known field that will mimic the stray field from the induced magnetic moment in graphene. Knowing that each of them will respond with opposite sign. As we have two pairs of horizontal coils that are perpendicular to each other, we can apply this horizontal field in the direction perpendicular to the long side (the y direction) of the GMRs, to simulate graphene's field.

- Let's say we apply a negative horizontal field to the GMR in the right. The signal coming from the change of resistance of the GMR will have a determined sign that will increase with increasing field. This sign will determine the diamagnetic sign of the field that will be measured by the GMRs.

- Once we know the diamagnetic sign, we should just compare it with the integrated sign of the data obtained (shown later in the results section), settling the diamagnetic or paramagnetic response of them.

- Then, by applying the opposite horizontal field, we can check that the GMR will show an opposite response and then, we determine the paramagnetic direction.

3.6 . Comparing with other sensors

As discussed in the SM in [17], we can briefly compare other probes to the GMRs. For example, TMR detectors are in principle more sensitive than the GMR sensors we have used. However, they are much noisier than GMRs in the range

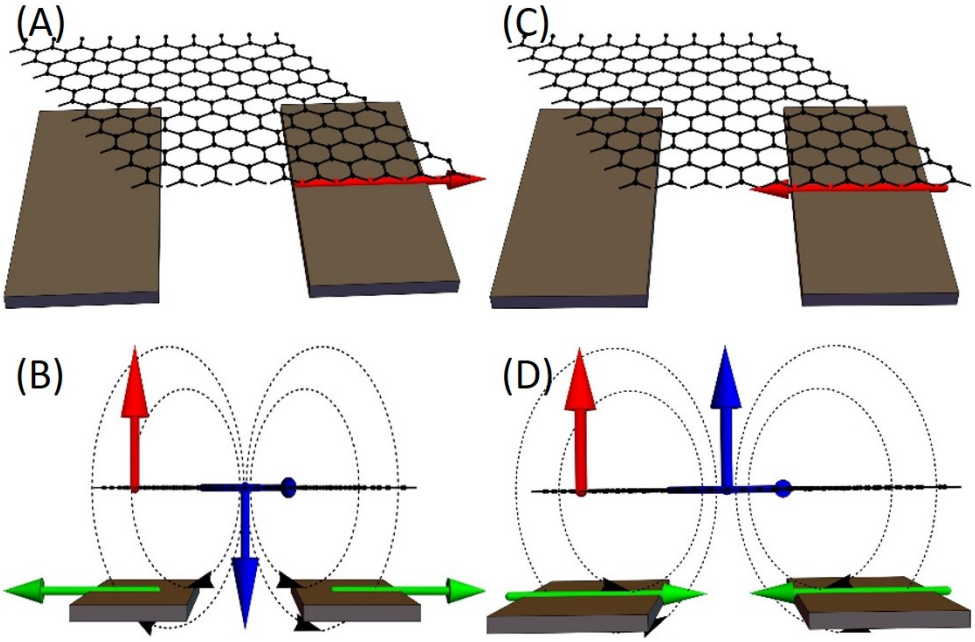

Figure 3.9: (A) Horizontal field applied on the right GMR to mimic the stray field from graphene. This field allows us to know the sign of response of the GMR to diamagnetism in graphene, shown in (B). (C) Horizontal field applied on the right GMR to mimic the stray field from graphene. This field allows us to know the sign of response of the GMR to paramagnetism in graphene, shown in (D).

of temperature and frequency we are working at. Moreover, the technique of fabrication of these sensors with the constraint that they also should work at cryogenics temperature with a small electric power consumption in order not to heat the graphene sample, is not as advanced as for the metallic GMR sensors we used. It is also interesting to compare this sensitivity of detection of our GMR set up to SQUID detectors. If one considers a SQUID of 10 micron square 0.1 nT leads to a flux of the order of 10^{-21}Wb $= 0.5 \times 10^{-6}\Phi_0$ which is of the order of the best sensitivity which can be achieved in zero magnetic field in a micro SQUID. Nano SQUIDs are even more sensitive in terms of flux detection. Their sensitivity in terms of magnetic field is however limited to 1nT, see [52]. They have a much better spatial resolution than our GMR detectors which translates into a higher sensitivity in terms of magnetic moment [53]. They can detect a single Bohr magneton electronic magnetic moments, however all these SQUID detectors are also very sensitive to out-of-plane magnetic field. In the present experiment, we exploit the fact that GMR sensors are insensitive to the out-of-plane component of the magnetic field, which is obviously not the case for SQUID sensors. NV sensors are very nice quantum detectors of small magnetic moments but they cannot be operated in magnetic fields above 100mT moreover they are not sensitive to the sign of the magnetic field detected, whereas this sign issue is essential in our experiment.

3.7 . Limit of magnetic field detection

The magneto-resistive sensors are inserted into a Wheatstone bridge circuit with adjustable dc currents (in the 0.1 to $1\mathrm{mA}$ range) through the two GMR strips, in such a way that the bridge voltage is zero in a uniform horizontal magnetic field. The bridge voltage is then read by a low noise voltage amplifier. We use a low noise voltage amplifier which input noise voltage is $2\mathrm{nV}/\sqrt{\mathrm{Hz}}$ above $40\mathrm{Hz}$ (the current noise of the order of 10^{-14} $\mathrm{A}/\sqrt{\mathrm{Hz}}$ yields a negligible contribution through the 150 Ω GMR sensors). We show in figure 3.10 the voltage noise of the amplifier together with the noise measured on the DC current biased GMR sensors. This data show that the amplifier noise is negligible compared to the intrinsic noise of the GMR We have also checked that the graphene signal on the GMR does not depend on frequency between 7 Hz and 125 Hz but is more noisy at low frequency because of the low frequency 1/f noise of the GMRs. From this figure, it appears that it could have been also interesting to work at even larger frequency. However we are concerned with the fact that at high frequency the modulation of the gate voltage induces current in graphene giving rise to an out-of-phase signal on the GMR sensors. By limiting the frequency below 200 Hz, we ensure that this contribution is negligible compared to the in-phase component due to the equilibrium orbital moment of graphene. The lowest detectable magnetic field is then simply related to the voltage noise measured on the GMR bridge $V_n = 4\mathrm{nV}/\sqrt{\mathrm{Hz}}$ knowing the

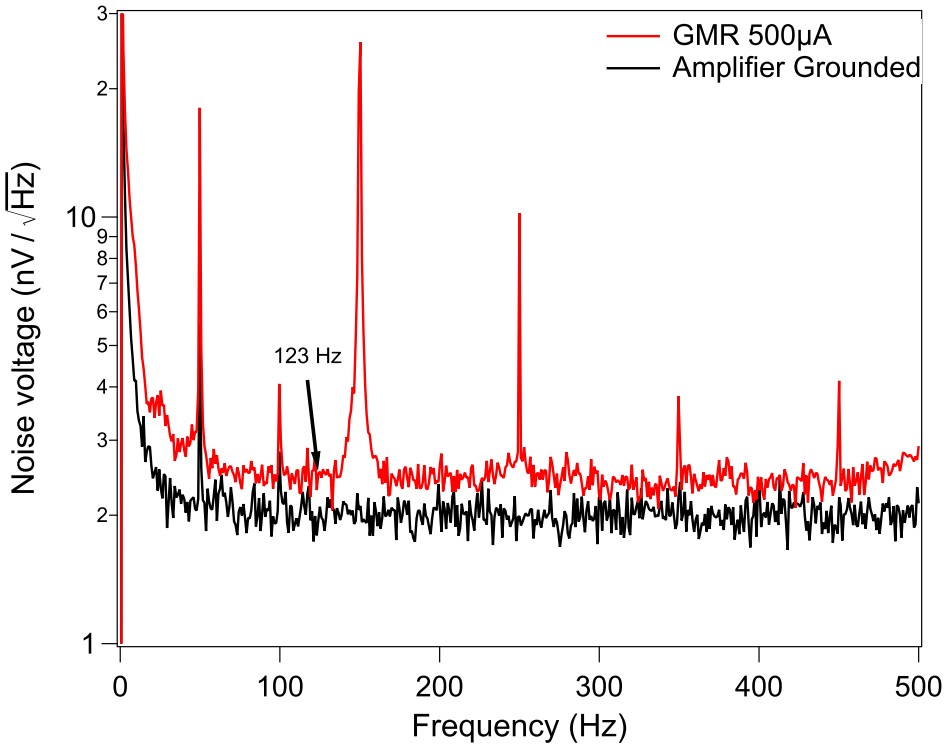

Figure 3.10: Noise spectrum of the short-circuited GMR probes and with 500μA through the GMRs (red). The peaks at odd multiple values of 50Hz come from the power supply of the building sector [17]. We highlighted 123 Hz because it is a typical value used in our experiments.

sensitivity of the GMRs, $s(B_{perp}) = 2500\ \Omega\,\mathrm{T}^{-1}$ shown in figures 3.5 and 3.8, and the DC current drive $I_{GMR} = 0.5\ \mathrm{mA}$ which is the maximum allowed value to keep the graphene device at $4.2\ \mathrm{K}$. When data is averaged over time τ the sensitivity reaches $\delta B = V_n/(2sI_{GMR}\sqrt{2\pi n\tau}) = 40\ \mathrm{pT}$ for $n = 100$, $\tau = 3\ \mathrm{s}$, at $B_{perp} = 0.1\ \mathrm{T}$. And $0.4\ \mathrm{nT}$ at $B_{perp} = 1\mathrm{T}$, taking into account of the decrease of the sensitivity of the GMRs with perpendicular magnetic field.

4 - Stack fabrication and measurement technique

In this chapter we describe the experimental techniques and fabrication details that are used through all the experiments performed during this thesis. We will discuss the most important details necessaries to understand the fabrication as well as how the principle of the measurement work.

4.1 . Samples fabrication

Although it can be found that each group has its own recipe for the fabrication of van der Waals hetero-structures, the basic steps are usually very similar. Here we present our version of the recipe derived from reference [54].

4.1.1 . Exfoliation

The process starts with the preparation of the silicon substrate needed to exfoliate the crystals. After cutting the wafer in easy to use and store chips, the procedure is to clean them in 3 consecutive ultrasonic baths in acetone, isopropanol and deionized water. Each bath lasts for 5 to 10 min. The exfoliation consists in the separation of the bulk crystal into its layers. For that, we use adhesive tape, deposit some pieces of the bulk crystal on the tape and then, by using another piece of tape, we glue and tear the second piece to get thinner flakes. Then we deposit these tapes on top of our silicon chips. Although the chips have to be cleaned once more before contacting the adhesive tape. For this, we need to do oxygen plasma tratment for around $20\mathrm{sec}$ as suggested in [54]. This gives the best results in terms of yield and size of the graphene crystals. In the case of BN, the procedure is the same except for the plasma cleaning. This is because we are not interested in few layer BN flakes. For thickness larger than $50\mathrm{nm}$, it is not necessary to use the plasma. Once the tapes are on the chips, we heat them up to $100^{\circ}\mathrm{C}$ for around $3\mathrm{min}$. Then, we let them cool down and separate the tapes from the chips.

4.1.2 . Transfer

To pick up the flakes, stack and deposit them on the GMRs we used a technique similar to [54]. The difference is the polymer used and consequently, the temperature values. We use Poly carbonate (PC). Due to its high adhesive power and relatively low melting point it has become a very useful tool in the assembly of van der Waals hetero-structures. In our case, the impossibility to heat the probes to high temperature, makes PC the only polymer which can be used. Depending on the concentration, PC's melting point is around 180°C and it can be removed with its solvent, chloroform, which does not affect the alumina layer on our chips.

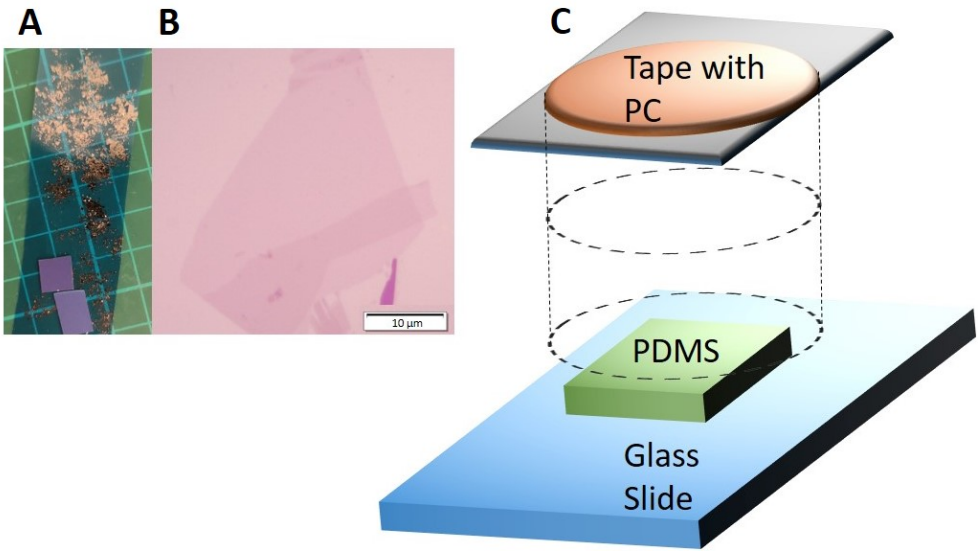

Figure 4.1: (A) Graphite crystals on a scotch tape. (B) Graphene flake on a SiO_2/SiO substrate. The monolayer is the part where optical contrast is the lowest. (C) Schematics of the device consisting of a PC layer on top of a PDMS cushion used to fabricate the stacks.

Typical used concentrations of PC in chloroform are between 5-10% in mass. The difference being that higher concentrations tend to be more plastic and easy to manipulate, but the melting point tends to increase with concentration. The procedure to pick up flakes is as follows: First, we touch the silicon substrate close to the region where the top BN is placed, leaving some space between the touching point and the flake, typically $100\mu\mathrm{m}$. Then, when we increase the temperature of the stage to $90°\mathrm{C}$, due to its thermal expansion, the film spreads it and covers the whole BN. Then, we stop heating and let the thermal contraction reduce the size of the contact zone. When the film retracts, it will pick up the BN flake. Once we have the BN flake on the film, we repeat the procedure but this time we carefully place the BN on top of the graphene we have selected. This time, it is not necessary to heat up to $90°\mathrm{C}$, as even room temperature is sometimes enough to pick up. Finally, we repeat the same procedure to pick up the bottom BN. Then we must deposit the stack on the GMRs. It is necessary to melt the PC film to do so. We slowly increase the temperature, slightly retracting the slide from the stage to keep the contact zone constant. This helps the PC film to break far from the flake to reduce the risk of picking it up again. At $180°\mathrm{C}$ we will see a dark thick circumference that indicates that the PC has broken. Then it is safe to slowly retract the slide to separate it from the stage.

Once the film is cold, we can take the chip and soak it into chloroform for 15min to clean the PC. Then, the film melts leaving few traces and the stack is

ready to pass to the contact fabrication. Contacts are made using a combination of electron beam lithography and metal deposition. Electrodes are usually made of one thin layer of around 10 nm of titanium or palladium and a thicker layer of gold. Pd is used in the cases where graphene needs to be connected through 1D contacts, to guarantee that the metal contacts the graphene. Pd is deposited using sputtering technique, which makes the flow of metal isotropic. Ti is usually used for the first layer of the gates. The reason being its good adhesion with non metallic surfaces. Ti is usually deposited using electron-beam vapor deposition as well as gold.

The fabrication methods described above are general for all of the samples in this manuscript. Nevertheless, for the fabrication of the moiré samples, we must add an extra consideration: moiré effects are noticeable at angles smaller than 2°, and increasing for smaller angles. So we must make sure that graphene and BN crystals are aligned and for this, we should look at the geometry of the crystals.

In the following, we will describe the two methods we used to fabricate the 2 moiré samples that we study and whose results will be shown below in chapter 6. We have called these samples M_A and M_B.

4.2 . Fabrication of the graphene/BN moiré samples

In a honeycomb lattice, one can have two type of endings: armchair or zigzag, both are shown in figure 4.2. Given this, an arbitrary edge in a flake can be a combination of multiple sections of different ending. However, long straight edges are formed by large series of the same type of ending or as a linear combination of both endings. In this way, a long straight edge will be either parallel to a lattice vector or to a linear combination of them.

Then, we first identified long straight edges in both graphene and hBN in each case. These edges follow the crystallographic axes of each honey-comb lattice. Therefore, by aligning these straight edges, one has equal probability that graphene and hBN are aligned or that their respective alignment are shifted by a 30° angle. In order to guarantee the alignment, two different methods were followed for the two samples M_A and M_B investigated .

For sample M_B, a flake of graphene with a long straight edge of about 45μm long was cut in three parts of roughly 20µm, 5µm and 20µm respectively. The first part was aligned and picked-up with a straight edge of a big flake of hBN. Then covered by a bottom misaligned hBN. The second and third parts were rotated with an angle of 30° with respect to the hBN edge, picked up with another part of the same top hBN flake and finally covered with a misaligned hBN. Raman spectroscopy measurements allowed us to determine which of the two samples is the one with the largest moiré constant by measuring the width of the 2D peak. This sample was selected and deposited on the top of the GMRs based magnetization detector, using the standard dry transfer techniques.

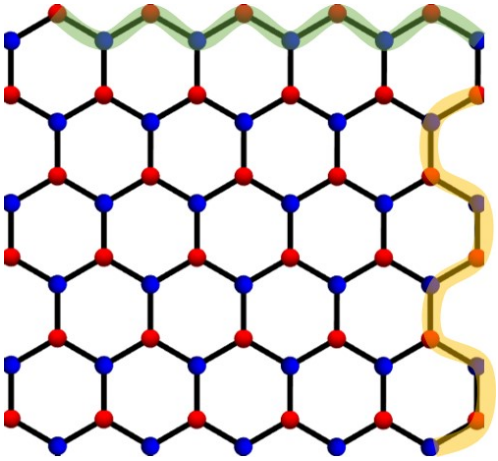

Figure 4.2: Representation of a graphene flake where the 2 types of borders are highlighted. Zigzag is highlighted in green, whereas armchair is in yellow

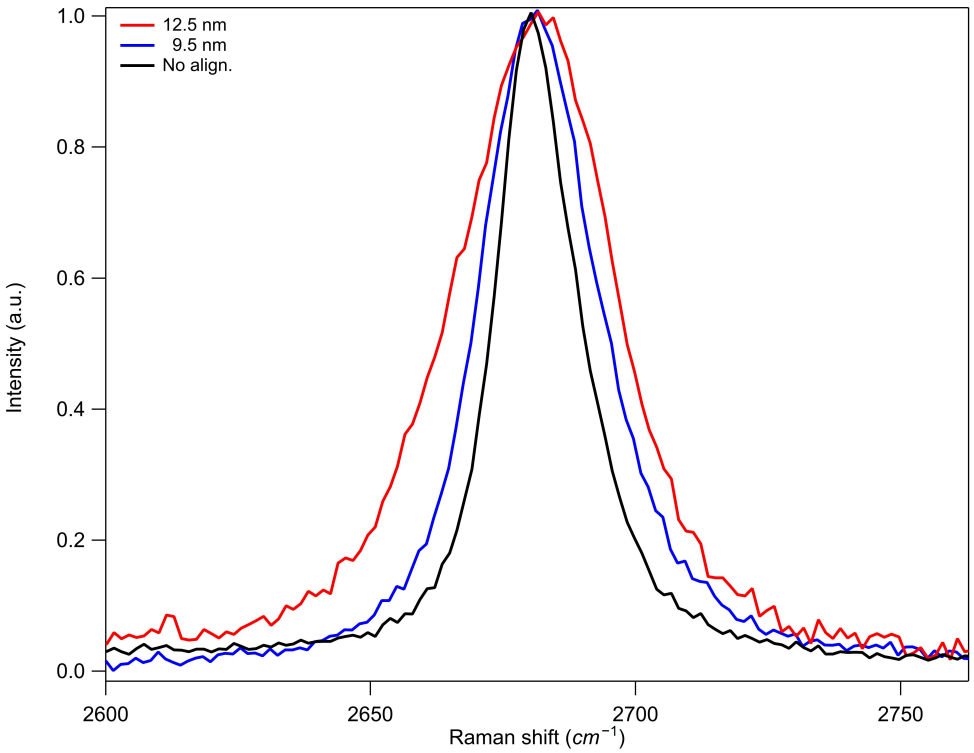

Figure 4.3: Signatures of the moiré potential on the width of the Raman 2D peak.

In the case of sample M_A, a large hBN flake was cut into two parts along

one main crystallographic edge (this was done by opening a narrow slit though the hBN flake using electron-beam lithography followed by reactive ion etching) A single graphene flake was then aligned along the straight edge of one of the halves of the hBN flake, and encapsulated beween this part and the other half previously rotated by $30°$. The presence of a long-range moiré pattern, was confirmed by Raman spectroscopy. For both samples these Raman experiments enabled us the determination of the moiré lattice parameters. According to [55], the FWHM of the 2D peak of the Raman spectrum of graphene varies linearly with the size of the moiré superlattice, a_M leading to the relation

$$\text{FWHM}_{2D} = 2.77 * a_M + 0.77. \tag{4.1}$$

From figure 4.3, we found the FWHM of the 2D peak to be 26.5cm^{-1} for M_A sample and 34.9cm^{-1} for M_B. From these values, using the relation given above relating the width of the Raman 2D peak to the moiré lattice, we can deduce for the 2 samples A and B, $a_M = 9.5 \pm 0.5\text{nm}$ and 12.5 ± 0.5 nm as well the twist angle θ between the hexagonal lattices of graphene and hBN acording to the relation

$$a_M = \frac{(1+\epsilon)a}{\sqrt{2(1+\epsilon)(1-\cos\theta)+\epsilon^2}}. \tag{4.2}$$

where $\delta = 0.017$ is the ratio between graphene and hBN lattice constants). We find $\theta_A = 1.1 \pm 0.1°$ and $\theta_B = 0.6 \pm 0.1°$.

4.3 . Set up and dimensions

We now look at the coupling between our sample and the sensors. For this, it is important to insist on the fact that the objective is to measure the stray field of the orbital currents. Because the GMRs are sensitive to the in-plane field, then, we must let this stray field have an in-plane projection as important as possible. This can be done by centering the part of the sample covered by the gate in between the GMRs, and adjusting the position of the graphene sample along the z axis perpendicular to the GMR, as shown in 4.4. There is a compromise to be done between the distance and the angle of the field lines on the GMR. On one side, the higher the sample is located, the smaller the intensity of the field (Biot-Savart $1/r$). On the other hand, a higher sample guarantees that the horizontal projection is larger.

In order to estimate the magnetic susceptibility of graphene, a geometrical model of the orbital current loop is needed. The easiest model one can imagine is the one of a current flowing along the edges of the gated region of graphene. This is equivalent to a thin rectangular loop carrying the orbital current. The edges parallel to the GMRs mostly contribute to the detected magnetic field. To illustrate better the dimensions and quantitatively estimate the relation of field and current, we used in this part the dimensions of the first sample that we measured

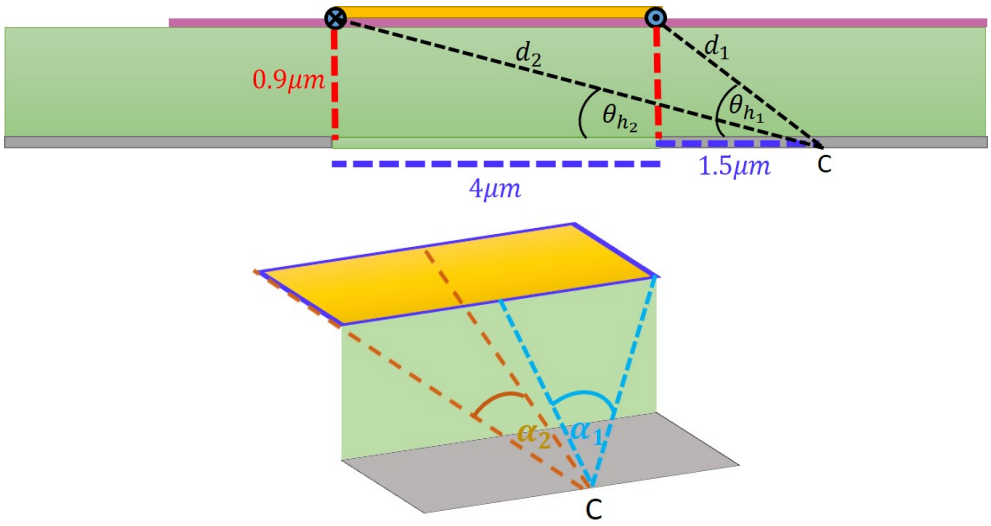

Figure 4.4: Front and lateral views of the sample with the definition of the angles θ_{h1} and θ_{h2} between the 2 edges of the gate electrode and the plane of the GMR. C is the center of symmetry of the GMR detector.

[17] (the other samples studied in this manuscript have similar geometries, except for M_B, which is smaller). From Biot-Savart law we can determine the horizontal component of the magnetic field detected by the GMR. This value at the point C, the center of the GMR, is computed from the distances from C to the parallel edges of the gated region: $d_1 = 1.75$ μ m and $d_2 = 5.57$ μ m as well as the angles $\theta_{h1} = 30.96^o$, $\theta_{h2} = 9.3^o$ $\alpha_1 = 76^o$, $\alpha_1 = 51.5^o$ shown in figure 4.4.

$$B_{GMR} = \frac{\mu_0 I_{orb}}{2\pi}\left[\frac{\sin(\theta_{h1})}{d_1}\sin(\alpha_1) - \frac{\sin(\theta_{h2})}{d_2}\sin(\alpha_2)\right] \tag{4.3}$$

from where we can find the coefficient relating the orbital current (or equivalently the magnetization per unit surface) to the field measured by the GMR sensor:

$$I_{orb} = m_{orb}/S = 22.3 \times B_{GMR} \text{ in A/T} \tag{4.4}$$

We also applied the same model to compare the experimental value of the magnetic field induced on the GMR by a rectangular gold loop (e-beam lithography and metal evaporation) which was deposited between the GMRs. The measurements of this loop were made during a previous work in the group [56]. The dimensions of the loop shown in figure 4.5 were $4 \times 8\mu\mathrm{m}$, corresponding to the right lithographic pattern. An AC modulation of the current through the loop was used to determined the response of the GMR to the field generated by the loop. A sensitivity of $4 \times 10^{-2}\mathrm{T\,A^{-1}}$ was obtained experimentally. When we applied the model of equation 4.3 for the dimensions and geometry of this loop, the estimated sensitivity was $5.2 \times 10^{-2}\mathrm{T\,A^{-1}}$, which agrees within 30% of the experimental value.

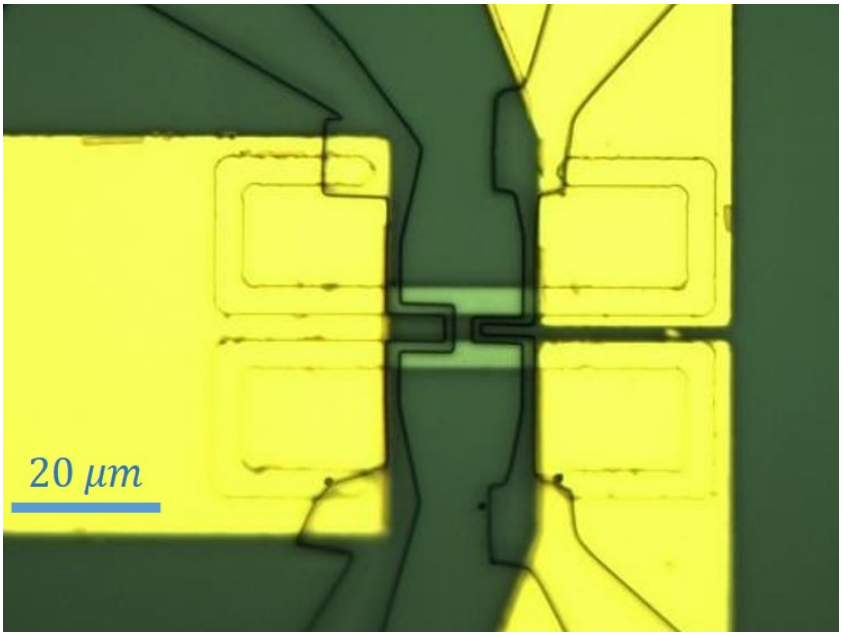

Figure 4.5: Lithography pattern of current loops fabricated to calibrate the GMRs sensors. Only the right one was operational. Adapted from [56].

4.4 . Extraction of the signal from the noise

Once we see how to eliminate the external field, we need to see how to discriminate our signal from 1) electronic noise and 2) from the magnetism coming from impurities in the alumina, for example. A way to address these problems is to apply an AC modulation on the gate voltage. First, let's talk briefly about the well known technique lock-in detection.

4.4.1 . Lock-in amplifier

Lock-in detectors are a very common equipment we can find in many laboratories. The reason for their popularity is their capability to measure a periodic signal buried into noise that can be several orders of magnitude larger. In order to do so, lock-in amplifiers use phase-sensitive detection to extract the part of the input corresponding to a specific frequency and phase, eliminating all other signals that have different frequencies [57, 58]. Lock-in detectors use a reference signal, mixed with the input, this means to multiply them and then to apply a low-pass filter. So we can model our input signal as:

$$V_{in} = V_s \sin(\omega_s t + \theta_s) + F_{Noise}(\{\omega\}) \tag{4.5}$$

where V_s is the amplitude of the periodic signal of frequency ω_s we want to measure, $\{\omega_i\}$ represents a set of all possible frequencies, in a simplified way to depict

noise as the contribution of many possible frequencies. The reference signal created by the lock-in has the form $V_{ref} = V_r \sin(\omega_r t + \theta_r)$. When V_s and V_{ref} are multiplied together, we can distinguish two parts:

$$\begin{aligned} V_{mixer} =& V_s V_r \sin(\omega_s t + \theta_s) \sin(\omega_r t + \theta_r) \\ &+ \sum_i V_r \sin(\omega_r t + \theta_r) F_{Noise_i}(\{\omega_i\}) \end{aligned} \tag{4.6}$$

where the second term contains the product of the reference and the noise. The first term of the right part can be written in a better way:

$$\begin{aligned} V_{PSD} &= V_s V_r \sin(\omega_s t + \theta_s) \sin(\omega_r t + \theta_r) \\ &= \frac{V_s V_r}{2} \left[\cos[(\omega_r - \omega_s)t + \theta_s - \theta_r] - \cos[(\omega_r + \omega_s)t + \theta_s + \theta_r]\right]. \end{aligned} \tag{4.7}$$

We are interested in having the exact same frequency in the signal and the reference, so the first term in 4.7 will become constant in time, and later, by applying a low-pass filter (which mathematically corresponds to averaging over a time $1/2\pi f_c$), all the AC components will average to zero. Particularly, the second term in equation 4.6 will give no contribution as the terms in the sum are the product of sine functions of different frequencies, so averaging them in time gives zero. The time constant in the lock-in determines the window for averaging. The the cut-off frequency is the frequency at which the signal is halved. These quantities are inversely proportional $\tau \sim 1/f_c$ and they determine the efficiency of the filtering. A larger time constant will led to narrow bandwidth but it requires longer measurements times.

Because of the design and planing of these experiments, we need now to generate the orbital magnetization in a way such that we can profit from the properties of the lock-in detectors. From the theoretical predictions, we expect OM on graphene to be strongly dependent on the chemical potential μ as shown in figure 2.4. It is a well known technology to control μ by applying a DC gate voltage between one electrode and graphene separated by a dielectric, forming a capacitor, and then sweeping this voltage to dope or undope graphene as the capacitor charges/discharges (details maybe in graphene). In addition to this, one can add modulation in series with the DC voltage. This means, to add an small AC voltage to the sweeping DC voltage. The reason to do this will be explained in the next section, but the idea behind this is that the lock-in will only measure the part of the signal that varies in time at the chosen frequency.

4.4.2 . Modulationg the chemichal potential of graphene

By considering graphene as one of the metallic plates of a parallel plate capacitor, we can design a set-up that allows us to add or remove charges from it. The principle is exactly the same as in a capacitor. The inset in figure 2.5 shows the schematic view of the capacitor. Graphene encapsulated between two Boron Nitride (BN) layers is connected by the sides following the 1D contact techniques.

We place an electrode on top of the upper BN which is going to determine the area of the capacitor. BN acts as the dielectric of the capacitor ($\epsilon_r \sim 3.6$). Then, by applying a potential difference between graphene and the electrode, we can dope graphene by adding negative charges, electron doping, or removing negative charges, hole doping.

4.4.3 . Measured signal

The input of our lock-in is going to be connected to the output of a differential pre-amplifier with gain $G = 100$. It then measures the potential difference between the 2 GMRs, ΔV_{GMR}, as shown in figure 3.6. Considering section 3.2, we will measure the horizontal field dependent variations of the resistance of the GMR, this means:

$$\Delta V_{GMR} = 2 \times I \times \delta GMR(B_M). \tag{4.8}$$

where the factor 2 takes into account the 2 probes. This δGMR, is the field dependent part and the field, B_M, is the horizontal projection of the stray field coming from graphene's magnetism:

$$\delta GMR(t) = \frac{\partial R}{\partial B_M} \delta B_M(t) \tag{4.9}$$

where the derivative is the sensitivity of the probes, typically in the order of $1 - 2.5\ \Omega\,\mathrm{mT}^{-1}$. In summary, the measured quantity is the change in resistance, $\delta GMR(t)$, at the frequency of modulation of the gate. We can write then:

$$\delta GMR(t) = \frac{\partial R}{\partial B_M} \frac{\partial (KM)}{\partial V_g} \delta V_g(t) \tag{4.10}$$

where $B_M = KM$, being K a geometrical constant that has been determined by assuming the path of the orbital current and by usign Biot-Savart's law. K was calculated in section 4.3. $\delta V_g(t) = \delta V_g(\omega, t)$ is the modulation of the gate voltage, at a frequency ω that is also the reference frequency of the lock-in.

So rephrasing equation 4.8 in terms of the gate voltage, at first order we have:

$$\Delta V_{GMR} = I \left[\frac{\partial R}{\partial B_M} \frac{\partial (KM)}{\partial V_g} \delta V_g \sin(\omega t) \right] \tag{4.11}$$

and by the principle of functioning of the lock-in, we know we will only recover the part of the signal oscillating at frequency ω, so the information we get from the lock-in is:

$$V_{lock-in} = IK \left[\frac{\partial R}{\partial B_M} \frac{\partial M}{\partial V_g} \delta V_g \right] \tag{4.12}$$

from where it is easy to extract the actual quantity of interest:

$$\frac{\partial M}{\partial V_g} = \frac{V_{lock-in}}{IK \left[\frac{\partial R}{\partial B_M} \delta V_g \right]}. \tag{4.13}$$

5 - Experimental results: McClure susceptibility in Graphene

In this part of the thesis, we will present the results obtained for a graphene monolayer. By using the measurement principle described in chapter 3 and 4, here we will present the measurement of graphene's orbital magnetic susceptibility. This chapter is taken from the article in reference [17].

5.1 . Detection of graphene's divergent orbital diamagnetism at the Dirac point

Orbital magnetism results from the quantum motion of electrons in a magnetic field. At low energy, this motion leads to the Landau spectrum, which is, in most two dimensional (2D) conductors, a harmonic oscillator-type spectrum with equally spaced levels separated by the cyclotron energy $\hbar\omega_c$ [11]. As long as the material is non superconducting, this spectrum causes a very small diamagnetic low-field susceptibility, that is usually hidden by spin contributions. However, some materials, such as graphene, can display extraordinarily large diamagnetism. This was predicted in the theoretical work of McClure [12], who showed that graphene is diamagnetic at half filling (at the so-called Dirac point), with a divergent zero field susceptibility

$$\chi_0 = \frac{\partial M}{\partial B} = -\frac{2e^2 v_F^2}{3\pi}\delta(\mu) \tag{5.1}$$

where v_F is the Fermi velocity, e is the electronic charge and the Fermi energy μ is zero at the Dirac point. This is all the more surprising because the density of states is zero at that point. The reason for this singular susceptibility stems from the electron-hole symmetric linear spectrum of Dirac relativistic electrons, giving rise to a Landau spectrum quantized as $\pm\sqrt{nB}$ where n is a positive integer. The diamagnetic sign of χ_0 is attributable to the existence of the zero-energy Landau level ($n = 0$), as mentioned in 2 (see also figure 5 of [19] and related comment). This peculiar level is known to result from the Berry phase [59] of π acquired by the wave function pseudo-spin upon a revolution around a Dirac cone in reciprocal space [35]. Therefore, the diamagnetic sign of the susceptibility at the Dirac point is a direct consequence of the π Berry phase. Indeed, it has been shown that slightly different models with a zero Berry phase lead to orbital paramagnetism at the Dirac point [19]. To summarize, the divergence reflects the linear spectrum and the diamagnetic signe reflects the non-trivial geometry of the eigenstates via the Berry phase [19].

However, despite these striking predictions, the singular orbital magnetism of a single graphene flake remains undetected. The reason for this lies in at least

three obvious experimental difficulties. First, the magnetic signal of an atomic monolayer is extremely small. Second, the McClure singularity, originally computed for an ideal system without disorder, at zero temperature and in the limit of zero magnetic field, is rounded when any of these conditions is relaxed [28, 60, 61, 62]. Finally, this orbital magnetism is expected to be hidden by the magnetism of spins originating from edges, vacancies, or impurities [63], which tends to become dominant at low temperature. This may explain why magnetization measurements have to date only been performed on a macroscopic number of graphene flakes. In one case [64], the focus was mainly on the spin paramagnetism of induced vacancy- and resonant states-type defects, which were found to depend on the chemical doping of the samples. A second set of measurements [65] did focus on the diamagnetism, and found diamagnetism larger than that of pure graphite by a factor of 3. The magnetization curves at high fields were found to be compatible with the $\sqrt{B}$ dependence predicted for the Dirac spectrum. However it was not possible to fix the doping in those experiments, nor could the residual contribution of paramagnetic spins along edges of the flakes be well controlled [66].

In the present experiment, by contrast, we measure the orbital moment of a single flake whose Fermi energy is precisely controlled.

This is achieved by implementing several sensitivity-enhancing features detailed in chapters 3, 4 and next section. As shown in figure 5.1, our experiment consists of graphene monolayer, encapsulated between two hexagonal boron nitride (hBN) 2D crystals, capacitively coupled to a top-gate electrode and positioned above a highly sensitive magnetic detector made of two giant magnetoresistance (GMR) strips (chapters 3,4 and next section) in a Wheatstone bridge configuration. One key asset is that whereas graphene's orbital magnetism responds to a field perpendicular to the graphene plane ("vertical" field), the GMR detectors are sensitive only to the in-plane-field, and thus detect the horizontal field generated by the orbital current loops in the graphene, (see 5.1), all the while being insensitive to the vertical component. A second feature is the addition of a small AC modulation to the DC gate voltage, which in turn modulates the magnetization with respect to gate voltage and thus the resistance of the GMR detector. Beyond increasing the sensitivity, this modulation technique makes gate-independent magnetic signals invisible. Thanks to those experimental implementations, we succeeded to detect the derivative with respect to gate voltage of the diamagnetic McClure peak at low magnetic fields. We have also measured the crossover to the de Haas-van Alphen magnetic oscillations at higher fields.

Figure 5.2 shows the gate voltage derivative of the field induced by the graphene sample on the calibrated GMRs as a function of V_g for perpendicular magnetic fields between 0.1 and 1.2 T. We found an antisymmetric peak centered at $V_g = -0.29$ V which was identified as the Dirac point from the measurement of the resistance of the sample $R(V_g)$, shown on 5.2b (and figure 5.10). At low magnetic fields the antisymmetric peak detected by the GMR is directly related to the derivative of

the McClure peak with respect to the chemical potential (controled by the gate voltage), as detailed in chapter 4. The experimental detection of this peak and its evolution with magnetic field are the central result of our work. Both the peak width and amplitude increase linearly with field, as shown in Figs. 5.2e and 5.2f. Above 0.6 T, $\partial M/\partial V_g(V_g)$ displays periodic oscillations in addition to the antisymmetric peak around the Dirac point. Those oscillations are related to the expected de Haas-van Alphen oscillations of the magnetization, as discussed below.

The magnetization, shown in figure 5.2c, is obtained by numerical integration of the curves in figure 5.2a. The peak amplitude translates to a few nanoTesla induced in the GMR plane by graphene's response to a 0.1 T perpendicular field. This illustrates the sensitivity of our experiment. The correspondence between this detected field, B_{GMR}, and magnetization is obtained by modeling the orbital magnetic moment as an effective current loop whose geometry is defined by the gated region of graphene 4.4. We find that positive magnetic fields produce a negative peak in magnetization, and vice-versa, which is consistent with the expected diamagnetic response of graphene [12]. This sign of the response was carefully settled via the sign of the response of the GMR sensor to a horizontal field of known orientation. (chapter 3).

We can assert that the signal cannot be attributed to gate-voltage-dependent magnetism of paramagnetic impurities, given the absence of temperature dependence between 4.2 and 40 K [67] (see 5.12). In addition, thanks to our gate-modulation technique, we can exclude spurious contributions from impurities or defects in alumina or graphene which would not depend on gate voltage. This contrasts with all previous measurements of graphene's magnetism, which were performed on large ensembles of flakes.

In the following we compare our results to theoretical predictions, taking into account the variations of chemical potential due to charge inhomogeneity, and ignoring the smaller broadening due to temperature (as detailed in next section).

Assuming a Gaussian distribution for the electrochemical potential μ'

$$P_\sigma(\mu') = \frac{1}{\sqrt{2\pi}\sigma} \exp - \left[\frac{(\mu'-\mu)^2}{2\sigma^2}\right] \tag{5.2}$$

yields a smoothed susceptibility

$$\chi(\mu) = \int P_\sigma(\mu')\chi_0(\mu')d\mu'. \tag{5.3}$$

Then, the $\delta-$peak of the susceptibility is broadened as

$$\chi_\sigma(\mu) = -\frac{2e^2 v_F^2}{3\pi} P_\sigma(\mu) \tag{5.4}$$

The full field and chemical potential dependence of the magnetization, including the oscillations, is given by the derivative $M = -\partial\Omega/\partial B$ of the disorder-averaged grand potential $\Omega_\sigma(\mu, B)$ (shown in next section):

$$\Omega_\sigma(\mu, B) = \int P_\sigma(\mu')\ \Omega_0\left(\mu - \mu', B\right) d\mu', \tag{5.5}$$

with

$$\Omega_0(\mu, B) = \frac{\epsilon_B^3}{4\pi^2\hbar^2c^2} \sum_p \frac{1}{p^{3/2}} \left[1 - 2S\left(2\sqrt{p}\frac{|\mu|}{\epsilon_B}\right)\right]. \tag{5.6}$$

The Landau levels at energies $\sqrt{n}\epsilon_B$, with $\epsilon_B = \sqrt{2e\hbar v_F^2 B}$, enter via the argument $\sqrt{p}|\mu|/\epsilon_B$ in the Fresnel function

$$S(x) = \int_0^x \sin\frac{\pi}{2}t^2 dt. \tag{5.7}$$

The predicted disorder-averaged magnetization is displayed in figure 5.3E. With increasing magnetic field, it evolves from a sole diamagnetic McClure peak of width σ at low field, to a broader peak with additional oscillations, centered at $\mu_n/\epsilon_B = \sqrt{n}$. figure 5.3D demonstrates how charge disorder induces rounding and attenuates the oscillations.

To compare these predictions to experiment, we have also to relate the gate voltage V_g to the chemical potential μ. Far from the Dirac point, this relation is quadratic, $V_g(\mu) - V_D = \alpha\mu^2\mathrm{sign}(\mu)$, with

$$\alpha = (e/C_g)/(\pi\hbar^2 v_F^2). \tag{5.8}$$

where V_D is the gate voltage at the Dirac point, and C_g is the geometrical capacitance per unit surface between graphene and gate, as determined from the V_g periodicity of the de Haas-van Alphen oscillations at high field, (detailed in next section). In contrast, close to the Dirac point, one can show that V_g varies linearly with μ, with a slope given by the standard deviation of μ disorder around the Dirac point, σ_0:

$$V_g(\mu) - V_D = 4\sigma_0\mu/\sqrt{2\pi}. \tag{5.9}$$

We find that the experimental data can be fit (see 5.4) using two constants, $\sigma_0 = 165\ K$ and $\sigma_\infty = 50\ K$, which describe the μ distribution at low and high doping respectively. The smaller value of σ_∞ is explained by the more efficient charge impurities screening at high doping. We note that the two constants can practically be determined independently, given the high sensitivity of the deHvA decay to disorder, and the large broadening of the McClure peak induced by magnetic field (of the order of ϵ_B) .

We find that $M(V_g)$ and $\partial M/\partial V_g$ depend on V_g, σ_0 and σ_∞, exclusively via the variables $V_g/\alpha\epsilon_B^2$, σ_0/ϵ_B and σ_∞/ϵ_B. In particular, the variation of the peak in $\partial M/\partial V_g$ width as $\alpha\epsilon_B^2$, shown in figure 5.2f, is directly related to this scaling originating from the Dirac Landau spectrum of graphene.

Next, we can compare the amplitude of the magnetization peaks measured at the Dirac point at 0.1 T and 0.2 T to the expected theoretical values. We find that the predicted value of the amplitude of the antisymmetric magnetization peak at the Dirac point $\frac{1}{B}\frac{\partial M}{\partial V_g}$ at low magnetic field, equal to $9.6 \times 10^{-6} A(TV)^{-1}$, is of the order of the experimental values although larger by a factor 2 to 2.6.

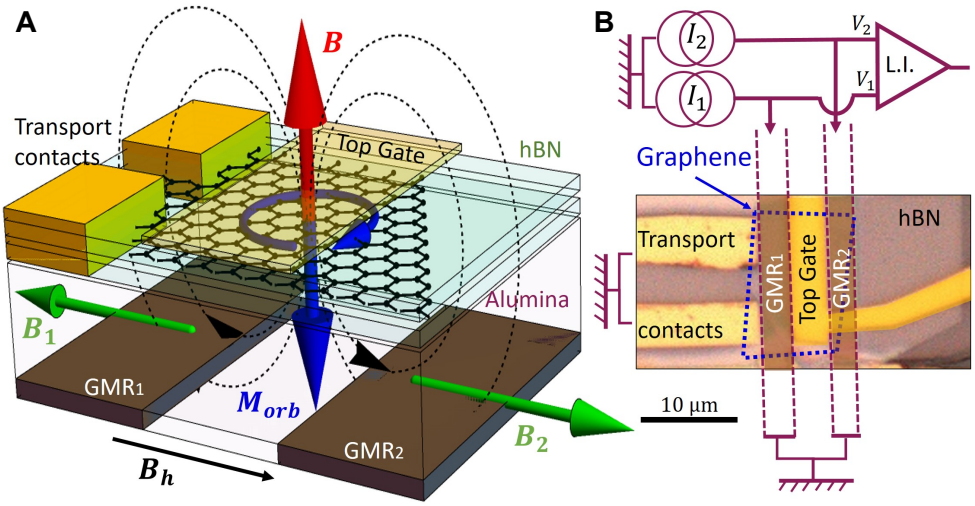

Figure 5.1: **A**: Principle of the experiment. The orbital magnetization can be viewed as a current loop generated by a vertical magnetic field and circulating around the graphene region covered by the gate electrode. It is detected by the two GMR detectors which measure the horizontal component of the field generated by this loop. The sensitivity is of the order of 0.1nT. **B**: Micrograph of the sample investigated, the gate voltage derivative of the orbital magnetization is measured via the difference between the dc current biased GMR resistances. The signal measured by a lock-in amplifier (L.I) is the ac component of the voltage difference $V_1 - V_2$ at the modulation frequency of the gate voltage. There is no current applied to the graphene sample during the magnetization measurements.

This is probably due to the over-simplified model of the Gaussian distribution of electrochemical potentials we have used. This value corresponds to a diamagnetic magnetization of two orders of magnitude larger than the Landau diamagnetism of a 2D free electron gas. Finally, deviations of the linearity between magnetization and magnetic field are expected when ϵ_B becomes much greater than σ_0, with a smooth crossover towards a $\sqrt{B}$ dependence, as showed in section 5.2. Since the calibration of the GMR sensor becomes delicate in high perpendicular magnetic fields due to the residual imperfect alignment of the magnetic field, these deviations from linearity cannot be checked in the field range above 0.5 T where they are expected to occur.

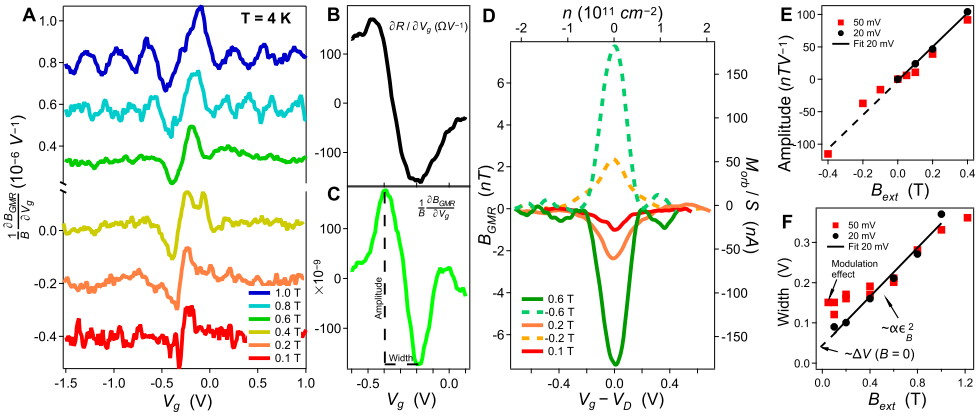

Figure 5.2: **a**: Detected modulation of the GMR detector's resistance with an ac gate voltage modulation of 20 mV, as a function of the DC gate voltage. The quantity plotted is $\frac{\partial B_{GMR}}{\partial V_g}$, deduced from the signal on the calibrated GMR sensor, divided by the applied vertical magnetic field B. Data are the average of 80 independent measurements. **b**: Derivative with respect to gate voltage of the two-point resistance of graphene measured through the side electrodes, in the region of the Dirac point, with a gate voltage modulation of 50 mV. **c**: For comparison purposes, GMR signal at -0.6 T using the same gate voltage modulation as in **b**. The GMR peak is much narrower. **d**: Numerical integration of the data plotted in **a**, yielding the magnetization per unit surface in nA (right axis), and the magnetic field B_{GMR} detected by the GMR device, in nT (left axis), as a function of the gate voltage. **e** and **f**: Field dependences of the peak maxima and widths, defined in **c**, for gate voltage modulations of 20 and 50 mV, and comparison with theoretical predictions. Deviations due to the excessive modulation amplitude are visible for a 50 mV modulation.

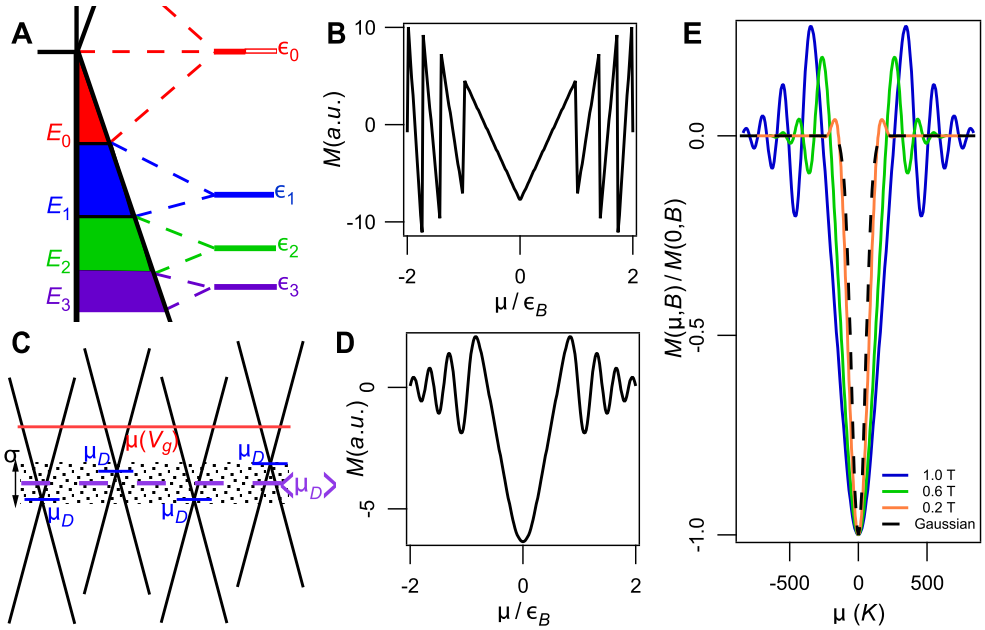

Figure 5.3: Calculated chemical potential dependence of the orbital magnetization of graphene in a finite magnetic field from (5.6), see also next section for more details. **a**: Evolution of the graphene spectrum in a magnetic field, (adapted from [19]). **b**: Without disorder, the magnetization, plotted as a function of the rescaled chemical potential μ/ϵ_B, exhibits discontinuities at the Landau levels energies $\sqrt{n}\epsilon_B$. **c**: Sketch illustrating the spatial distribution of electrochemical potentials $\mu' = \mu_D - \langle\mu_D\rangle$ where μ_D is the local Dirac point and $\langle\mu_D\rangle$ its spatial average. **d**: Rounding of $M(\mu/\epsilon_B)$ by a Gaussian chemical potential distribution with a variance $\sigma = 0.1\epsilon_B$. **e**: $M(\mu)$ for different magnetic fields for $\sigma = 50$ K. At low field the oscillations disappear and the magnetization displays a Gaussian diamagnetic peak at $\mu = 0$. This peak is broaden by magnetic field as soon as $\epsilon_B \geq \sigma$

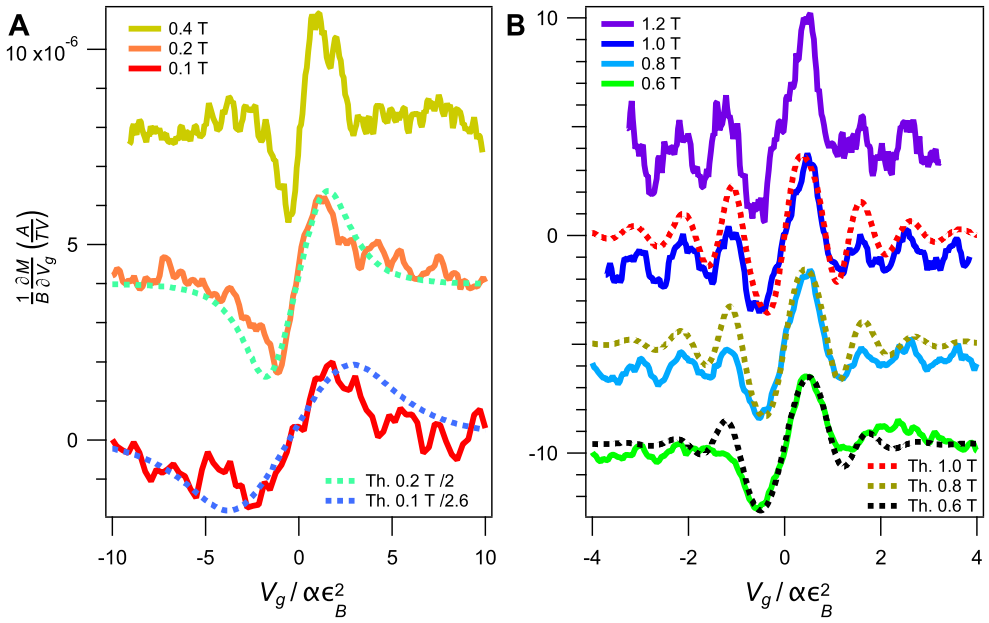

Figure 5.4: Fit of detected ac magnetization response to a gate voltage modulation of 50 mV, as a function of the dc gate voltage divided by $\alpha\epsilon_B^2 = 2\alpha e\hbar v_F^2 B$. Dashed lines show the theoretical gate dependence of $\partial M/\partial V_g$, with $\sigma_0 = 165$ K and $\sigma_\infty = 50$ K (relevant only for large field data in b), including the extra rounding effect due to the 50 mV ac gate modulation. The amplitude of the theoretical signal has been rescaled by a factor 1/2.6, respectively 1/2 at 0.1, respectively 0.2T to fit quantitatively the experimental data. The rescaling factors are closer to unity for higher fields but uncertainties on the calibration of the GMR at high field do not allow precise quantitative comparisons.

5.2 . Theoretical calculation of the susceptibility

We show some parts of the supplementary materials of the article in reference [17]. First in this part, we show a way to calculate graphene's orbital susceptibility derived by Gilles Montambaux and presented in [17].

The quantity we have measured is $\partial M/\partial V_g$, as a function of the gate voltage V_g. In this part we propose a theoretical derivation of this quantity. This is done in two steps, the dependence of the magnetization versus chemical potential $M(\mu)$ and the relation between μ and the gate voltage V_g. Special attention is given to the broadening due to a distribution of the electrochemical potential in the presence of disorder.

5.2.1 . Grand potential as a function of the chemical potential

Several alternative expressions for the field dependent part of the grand potential in graphene are found in the literature, including the original paper by McClure[12, 68, 69, 65]. Here we propose the following derivation.The electronic spectrum in a field is given by equation 2.19. with degeneracy $2eB/h$ per unit area. The grand potential Ω is a double integral of the density of states per unit of area $\nu(\epsilon, B)$ which can be written:

$$\nu(\epsilon, B) = \frac{2eB}{h} \sum_{n,\pm} \delta\left(\epsilon \pm \epsilon_B \sqrt{|n|}\right) \ . \tag{5.10}$$

A Poisson transformation leads to the Fourier decomposition of the density of states:

$$\nu(\epsilon, B) = \frac{2|\epsilon|B}{\pi\hbar^2 v_F^2} \left(1 + 2\sum_{p=1}^{\infty} \cos\frac{2\pi p\epsilon^2}{\epsilon_B^2}\right) \tag{5.11}$$

After a double integration, we obtain the oscillatory part of the grand potential for a clean sample and at zero temperature:

$$\Omega_0(\mu, B) = \frac{\epsilon_B^3}{4\pi^2\hbar^2 v_F^2} \Delta_0\left(\frac{\mu}{\epsilon_B}\right) \tag{5.12}$$

, with

$$\Delta_0(x) = \sum_{p=1}^{\infty} \frac{1}{p^{3/2}}[1 - 2S(2\sqrt{p}|x|)] \tag{5.13}$$

where $S(x)$ is the Fresnel integral :

$$S(x) = \int_0^x \sin\frac{\pi t^2}{2} dt \ . \tag{5.14}$$

This variation, first obtained by McClure (although in a different form) is recalled in figure 5.6-a. On an energy scale larger than ϵ_B, the function can be replaced by

a δ-function having the same total weight. The substitution $1-2S(|x|) \to \frac{4}{\pi}\delta(x)$ transforms eq. (5.12) into:

$$\Omega_0(\mu, B) = \frac{\epsilon_B^4}{12\pi\hbar^2 v_F^2}\delta(\mu) = \frac{e^2 v_F^2 B^2}{3\pi}\delta(\mu) \tag{5.15}$$

sometimes called the McClure peak.

At finite temperature, in the presence of elastic disorder, or with a distribution of the electrochemical potential around the average chemical potential (coinciding with Fermi energy at zero temperature), this expression has to be convoluted with one of the corresponding functions:

$$\begin{aligned} P_T(\mu) &= \frac{\beta/4}{\cosh^2 \beta\mu/2}\ , \\ P_D(\mu) &= \frac{T_D}{\mu^2 + (\pi T_D)^2}\ , \\ P_\sigma(\mu) &= \frac{1}{\sqrt{2\pi}\sigma} e^{-\frac{\mu^2}{2\sigma^2}}\ . \end{aligned} \tag{5.16}$$

Here we consider that the main source of broadening is due to the distribution $P_\sigma(\mu')$ for the electrochemical potential μ' assumed to be Gaussian with a standard deviation σ. which can be μ dependent. In graphene, the efficiency of the screening of charged impurities giving rise to the disorder potential increases indeed with doping, that is when moving away from the Dirac point. Therefore the fluctuation of μ' is expected to depend on μ: the standard deviation σ being a function $\sigma(\mu)$ which decreases with $|\mu|$, see figure 5.5. Here, we present the calculation of the grand potential, with a fixed value of σ.

$$\begin{aligned} \Omega_\sigma(\mu, B) &= \int_{-\infty}^{+\infty} P_\sigma(\mu')\Omega_0(\mu - \mu', B)d\mu' \\ &= \frac{\epsilon_B^3}{4\pi^2\hbar^2 v_F^2}\Delta_\sigma\left(\frac{\mu}{\epsilon_B}\right) \end{aligned} \tag{5.17}$$

with

$$\Delta_\sigma(x) = \sum_{p=1}^{\infty} \frac{1}{p^{3/2}} \int_{-\infty}^{\infty} \frac{e^{-y^2}}{\sqrt{\pi}} \left[1 - 2S\left(2\sqrt{p}|x + \frac{\sqrt{2}\sigma}{\epsilon_B} y|\right)\right] dy \tag{5.18}$$

This function is plotted in figure 5.6-b for $\sigma/\epsilon_B = 0.1$ which corresponds to $\sigma = 42$ K for $B = 1$ T.

In the limit $\sigma \gg \epsilon_B$, one recover the Gaussian decay

$$\Delta_{\sigma\gg\epsilon_B}(\mu/\epsilon_B) = \frac{\pi\epsilon_B}{3} P_\sigma(\mu) \ \longrightarrow\ \Omega_{\sigma\gg\epsilon_B}(\mu, B) = \frac{e^2 v_F^2 B^2}{3\pi} P_\sigma(\mu) \tag{5.19}$$

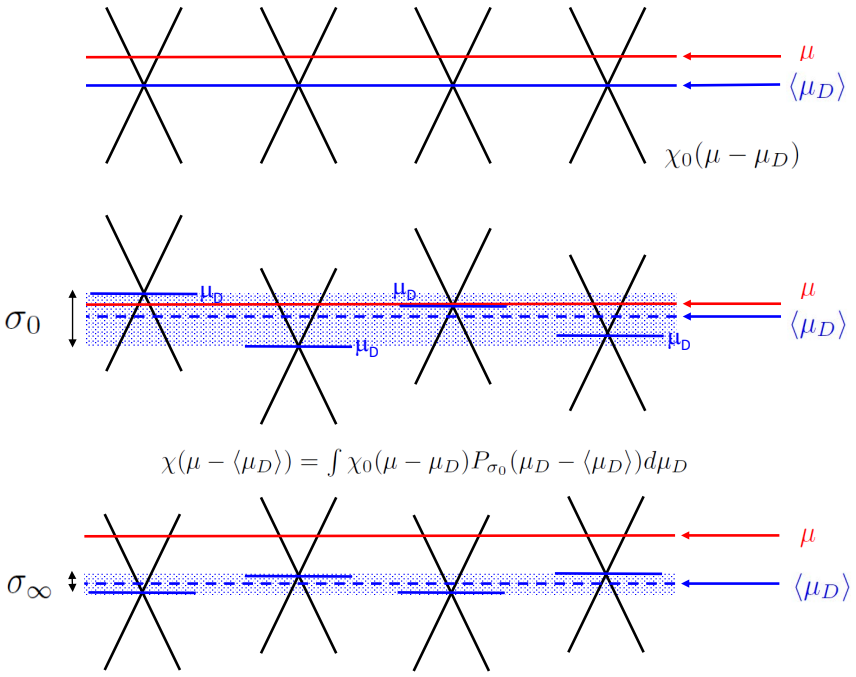

Figure 5.5: Schematic representation of the fluctuation of electrochemical potential $\mu' = \mu_D - \langle\mu_D\rangle$, measured with respect to average Dirac point $\langle\mu_D\rangle$. They are induced by a screened disorder potential produced by charge impurities which decreases when $\mu - \langle\mu_D\rangle$ increases: The standard deviation σ depends on μ.

or a decay as $P_T(\mu)$, $P_D(\mu)$ if temperature or elastic disorder are the main sources of broadening.

From the grand potential, we deduce the magnetization $M = -\partial\Omega/\partial B$ (here we compute $-\partial\Omega/\partial\epsilon_B$ noting that $\partial/\partial B = (\epsilon_B/2B)\partial/\partial\epsilon_B$). The dependence of this quantity versus chemical potential is displayed on figure 5.7. In principle all these calculations could also be done taking an explicit dependence of $\sigma(\mu)$.

5.2.2 . Non-linear field dependence of the magnetization

We discuss now the field dependence of the diamagnetic response, here at fixed chemical potential $\mu = 0$. In the presence of broadening, the field dependent part of the grand potential is given by :

$$\Omega(B) = \int P(\mu')\Omega_0(\mu', B)d\mu' \tag{5.20}$$

where $\Omega_0(\mu, B)$ and $P(\mu)$ are given by eqs. (5.12,5.13) and (5.16). Two limits are of special interest:

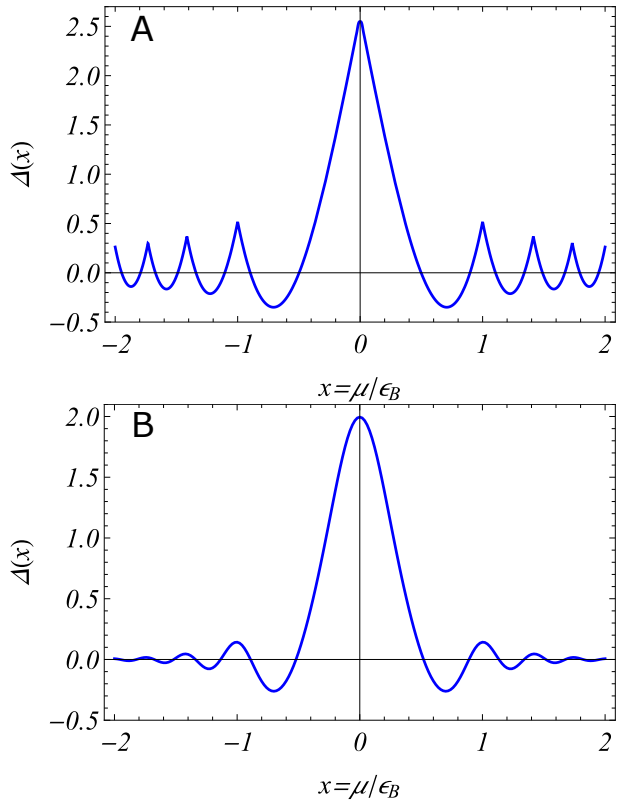

Figure 5.6: Functions $\Delta_0(x)$, and $\Delta_\sigma(x)$ for $\sigma/\epsilon_B = 0.1$.

When the broadening is large, that is T, T_D or $\sigma \gg \epsilon_B$,

$$\Omega(B) = P(\mu = 0) \int \Omega_0(\mu', B) d\mu' = \frac{e^2 v_F^2 B^2}{3\pi} P(\mu = 0) \tag{5.21}$$

leading to a quadratic field dependence of the grand potential as $B^2 \times \min(1/T, 1/T_D, 1/\sigma)$ and a magnetization linear in B. For the specific case of a Gaussian distribution of width σ, the grand potential reads in this limit:

$$\Omega_\sigma(B) = \frac{\sqrt{2} e^2 v_F^2 B^2}{6\pi^{3/2}\sigma} \tag{5.22}$$

In the opposite limit of a perfectly clean sample or very strong field, the field dependence becomes non-analytical [12] as :

$$\Omega(B) = \Omega_0(0, B) = \frac{\epsilon_B^3}{4\pi^2 \hbar^2 v_F^2} \zeta(3/2) = \frac{v_F e^{3/2} \zeta(3/2)}{\pi^2 \sqrt{2\hbar}} B^{3/2} \tag{5.23}$$

since $\Delta_0(0) = \zeta(3/2)$ and the magnetization is proportional to $\sqrt{(}B)$. Note that all limits can be summarized as

$$\Omega(B) \propto B^2 \times \min(1/\epsilon_B, 1/T, 1/T_D, 1/\sigma) \tag{5.24}$$

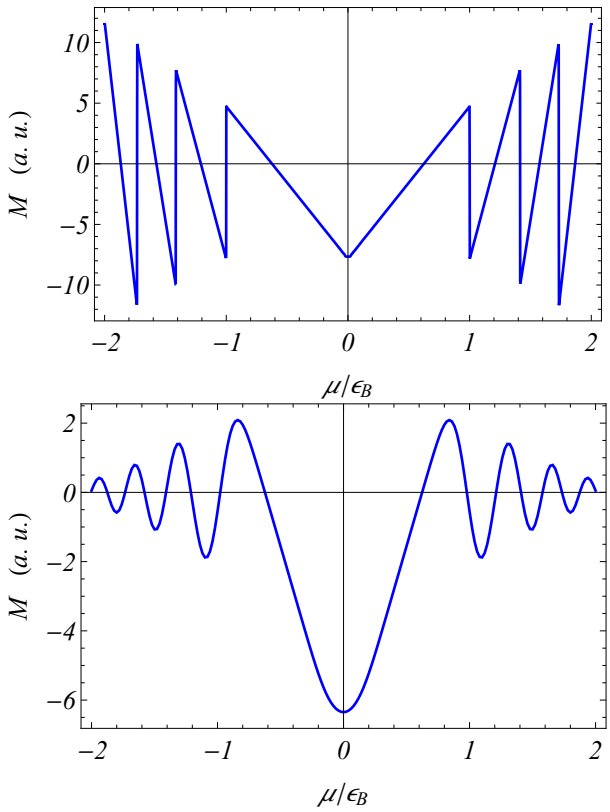

Figure 5.7: Magnetization as a function of μ/ϵ_B, for $\sigma = 0$ and $\sigma/\epsilon_B = 0.1$ independent of μ.

The non-linear field dependence of the magnetization is difficult to observe [65]. Authors in [65] have investigated deviations from the linearity at moderate magnetic field. A description of the interpolating regime has been proposed by [65] using a Langevin function. We stress here that the correct behavior (5.20) deviates significantly form a Langevin function, in particular in small field.

5.2.3 . Gate voltage $V_g(\mu)$

It is of fundamental importance to find the relation between V_g and μ given that in our experiment the control variable is precisely the gate voltage. We start by modeling the action of V_g as the one of a capacitance per unit surface relating V_g to the charge density in graphene: $V_g \times C_g = en$:

$$V_g = \frac{en}{C_g} = \frac{e}{C_g \pi} k^2 = \alpha \ \text{sign}(\mu - \mu_D)(\mu - \mu_D)^2, \tag{5.25}$$

with $\alpha = e/(C_g \pi \hbar^2 v_F^2)$. In the model of a Gaussian distribution of μ', this relation takes the following form, assuming that C_g is the geometrical capacitance between

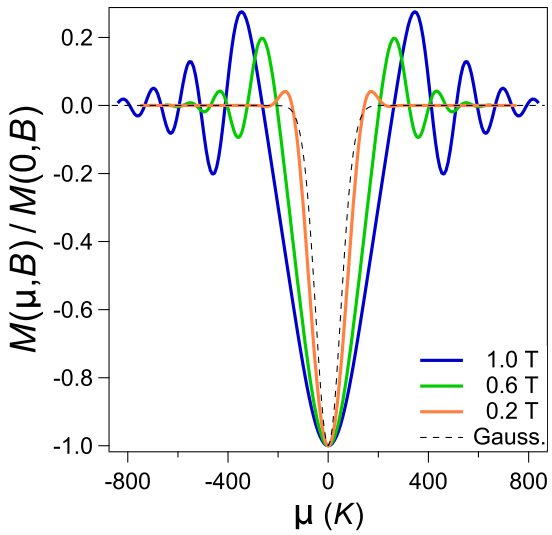

Figure 5.8: Theoretical magnetization (normalized to its value at $\mu = 0$) as a function of μ expressed in kelvins. The plot shows the broadening of the peak with increasing magnetic field.

graphene and the gate and therefore independent of μ:

$$V_g(\mu) = \frac{\alpha}{\sqrt{2\pi}\sigma} \int_{-\infty}^{\infty} \text{sign}(\mu - \mu')(\mu - \mu')^2 \exp\left(-\frac{\mu'^2}{2\sigma^2}\right) d\mu' \tag{5.26}$$

After integration, we get:

$$V_g(\mu) = \alpha \times \text{Erf}\left(\frac{\mu}{\sqrt{2}\sigma}\right)(\mu^2 + \sigma^2) + \frac{4\alpha}{\sqrt{2\pi}}\mu\sigma \times \exp\left(-\frac{\mu^2}{2\sigma^2}\right) \tag{5.27}$$

where Erf is the error function: $\text{Erf}(x) = \frac{2}{\sqrt{\pi}} \int_0^x e^{-t^2} dt$.

It is easy to generalize equation 5.27 to the case where σ depends on μ. It leads then to the two following expressions, respectively valid in the limits of low and large μ compared to σ_0:

$$\begin{aligned} V_g(\mu) &= 4\sigma_0\mu/\sqrt{2\pi} \text{ for } \mu \ll \sigma_0 \\ V_g(\mu) &= \alpha\mu^2 \text{ sign}(\mu) \text{ for } \mu \gg \sigma_0 \end{aligned} \tag{5.28}$$

In graphene, the efficiency of the screening of charged impurities giving rise to the disorder potential increases with doping, that is when moving away from the Dirac point. Therefore the fluctuations of μ' are expected to depend on μ: the standard deviation σ being a function $\sigma(\mu)$ which decreases with $|\mu|$. We denote σ_0 the value of $\sigma(\mu)$ close to the Dirac point and σ_∞ its limiting value far from the Dirac point. Experimentally our data give rise to $\sigma_0 \simeq 165K$ which is much larger than

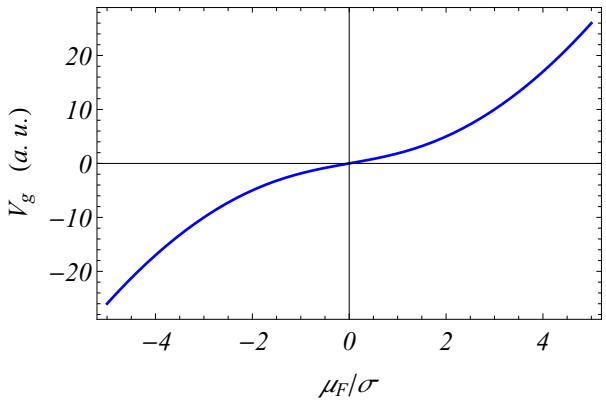

Figure 5.9: Relation between the gate voltage and the chemical potential, assuming that σ is independent of μ. Note the linear dependence of $V_g(\mu)$ at low μ compared to σ.

$\sigma_\infty \simeq 50K$ determined from the damping of de Haas-van Alphen oscillations at large $\mu \gg \sigma_0$. This is due to the formation of electron-hole puddles in the vicinity of the Dirac point [70, 71].

In order to describe experimental data we consider only these two values σ_0 which determines the width and amplitude of the McClure peak and the value σ_∞. These 2 parameters are sufficient to describe our experimental data in the whole range of gate voltage and magnetic field we have investigated.

5.3 . Additional data

Here we show some plots with additional information. For example, figure 5.10 shows the resistance of the sample as a function of the gate voltage. This measurement allowed us to obtain the position in gate voltage of the Dirac point. We also show the odd behavior of the measured magnetization as a function of the magnetic field in figure 5.11. Finally, we show the evolution of the derivative of magnetization as a function of temperature in figure 5.12. Here, in blue we have $\partial M/\partial V_g$ at $T = 4\mathrm{K}$. We did not observe a considerable change in the behavior of the curve up to $T = 40\mathrm{K}$ (curve in green). However, at $T = 60\mathrm{K}$, the amplitude of the signal that we obtained was considerably reduced (curve in red).

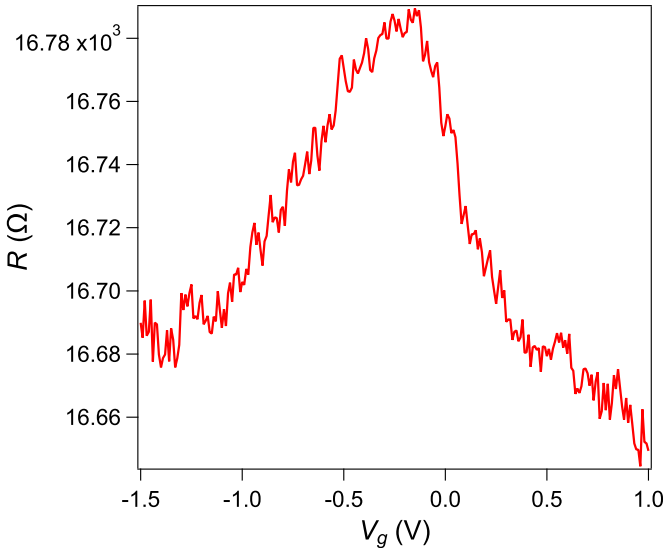

Figure 5.10: Resistance as a function of the gate voltage for the studied sample. The charge neutrality point is found at around -0.2 V.

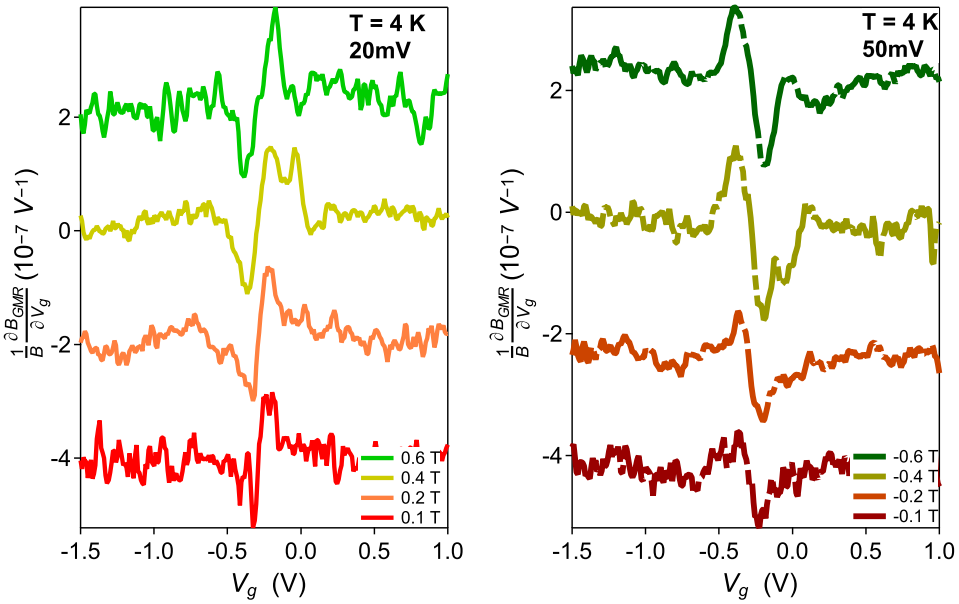

Figure 5.11: Derivative of the magnetization as a function of the gate voltage for different positive (left) and negative (right) fields.

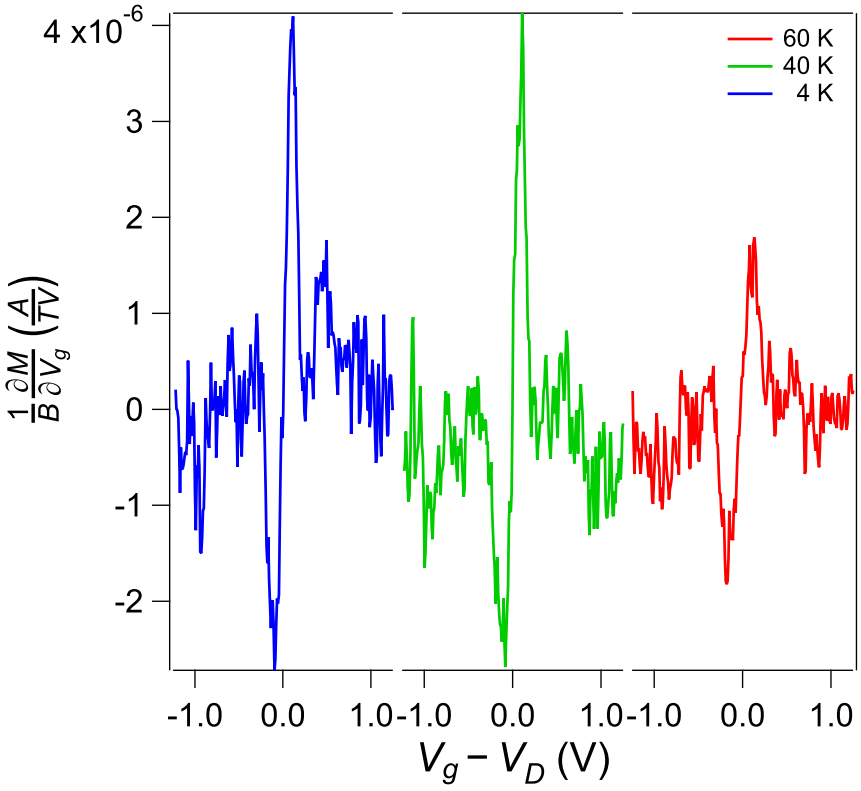

Figure 5.12: Derivative of the magnetization as a function of gate voltage for the same magnetic field. We can notice that the peak amplitude does not vary between 4.2 and 40 K but is reduced at 60 K.

5.4 . New measurements of the McClure peak: lower disorder

We present here the results of the magnetism of a different sample, named M_A. It consists of an encapsulated graphene flake between two BN crystals, with one of the BN crystals aligned with graphene at $1.1°$. This gives a moiré superlattice whose size is of around $9.5\mathrm{nm}$. Its fabrication is mentioned in section 4.2. According to the literature [72, 73], for this moiré size, there is small relaxation on the atomic positions and so, the gap opening at charge neutrality is negligible when compared with disorder. This allows us to treat the magnetism at the Dirac point in the same way as in the previous sections.

As shown in figure 5.13, the magnetization close to Dirac point features the diamagnetic McClure peak discussed in previous sections. This peak broadens with magnetic field and de Haas-van Alphen (dHvA) oscillations appear with increasing doping. Figure 5.13 shows both the derivative of the magnetization and the integrated curve as a function of the gate voltage for the M_A sample, in a perpendicular magnetic field of 0.2 T. The amplitude of the detected signal B_M is 15 nT, at the Dirac point. This is approximately equivalent to an orbital current of 350 nA. A direct comparison with the estimations given in the beginning of chapter 3 is not accurate and should be made with caution. The reason is that the rounding effects discussed there (equation 6.6 uses a thermal rounding) and here are different in nature and thus, give different results. However, if we take the disorder parameter σ_0 as an effective temperature T_{eff} at the McClure peak in equation 6.6, then the experimental data is of the same order of magnitude as expected (by a factor 2).

This data can be precisely described by the theoretical formulas derived analytically in section 5.2, (particularly equations 5.17 and 5.18) where the magnetization was derived from the magnetic field dependence of the grand potential of graphene at a chemical potential fixed by the gate voltage.

As before, disorder is modeled by a gaussian distribution of chemical potential μ whose standard deviations σ_μ decreases with its average, due to screening effects which are more efficient at large doping. The magnetization was shown to be a universal function of the variables μ/ϵ_B, σ/ϵ_B. The McClure peak at low field has a width $\sigma_0 = 80 \pm 5K$ and a characteristic energy scale of $\sigma_\infty = 20 \pm 5K$ for the damping of dHvA oscillations at larger doping, which are both twice smaller than in our previous sample from section 5.1 and indicate a better quality of the present samples. The dashed curve in figure 5.13A shows the theoretical fits for $\partial M/\partial V_g$ using those parameters.

Figure 5.13C shows the evolution of the magnetization with Landau level filling factor for different field values. These data show the increase of the dHvA oscillations relative to the McClure response as magnetic field increases. The magnetization is renormalized by the applied magnetic field, which in the linear regime is the magnetic susceptibility $\chi = M/B$. The low field apparent increase of χ with B, is an artefact due to the field modulation which broadens the McClure

peak. This effect becomes negligible when the intrinsic McClure peak broadening, proportional to B, exceeds the gate voltage modulation.

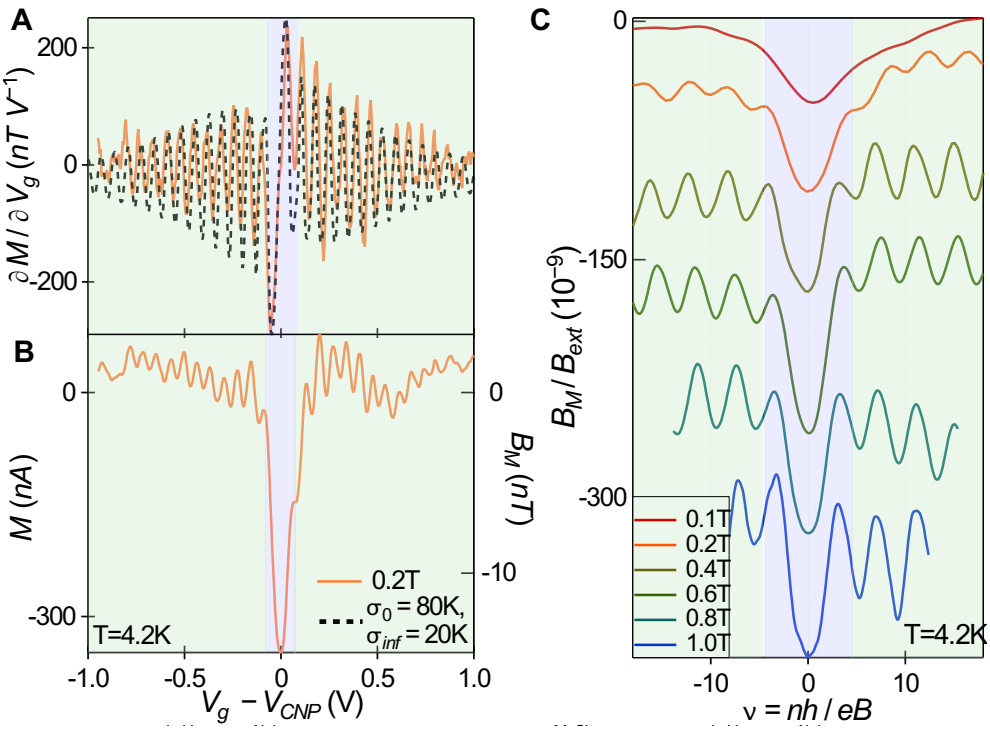

Figure 5.13: Sample M_A. **(A)** Solid line: derivative of the magnetization as a function of the gate voltage close to the charge neutrality point for a field of 0.2T. The curve is the average of 10 independent measurements. Dashed line: theoretical gate dependence of $\partial M/\partial V_g$. The low-energy and high energy disorder standard deviations σ_0 and σ_∞ were determined from the width of the McClure Dirac and the decay of deHVA oscillations. They are respectively 80K and 20K . **(B)** Magnetization per unit surface obtained by numerical integration of the data in (A) with, on right axis, units of the equivalent measured magnetic field by the GMR detector. **(C)** Evolution of the McClure peak and dHvA oscillations for different applied magnetic fields in dimension less units. On the y axis the detected magnetic signal on the GMR detector is normalized by the applied field. On the x axis the Landau levels filling factor is deduced from the carrier density $n = C_g V_g/e$ where C_g is the capacitance per unit surface of the gate.

6 - Orbital paramagnetism in graphene with a moiré potential

6.1 . Introduction

This section has been taken from the article in preparation: Singular paramagnetic orbital magnetism in Graphene with a moiré potential [74]. It will be submitted soon to a indexed journal but for now, we present a preliminary version.

As we mentioned in chapter 1, the orbital susceptibility can be decomposed in the contributions from the isolated bands and the interband contributions. For the isolated bands, the orbital susceptibility is proportional to the curvature of the energy dispersion relation (i.e. the inverse effective mass of carriers). This is known as the Landau-Peierls result [11, 75].

In multiband systems, in the other hand, the coupling induced between Bloch wave functions of different bands by the magnetic field gives rise to new effects. The zero field susceptibility is then not only determined by the curvature of the bands, but also by geometrical properties of Bloch functions such as the Berry curvature in reciprocal space [23, 19, 20, 21]. As an example of this, there is the divergent diamagnetism of undoped graphene at the Dirac point, predicted by McClure [12] and whose experimental evidence is discussed in the previous chapter. It was subsequently related to the π anomalous geometrical Berry phase at this point and to the existence a zero energy Landau level in magnetic field [40].

It is also known that orbital magnetism can be paramagnetic rather than diamagnetic. From general principles, the sum rule indicates that for a tight binding model, the integral of the susceptibility the full range of energy in a bounded spectrum must be null. This means that, if Landau diamagnetism is possible within this bound, then necessarily the susceptibility must be positive for some other value of the energy inside this interval. In particular, graphene is expected to exhibit a paramagnetic plateau [76, 19, 20, 21], when doping is increased both on the electron and hole sides. It was also predicted that orbital susceptibility is paramagnetic due to electron-electron interactions, for doped graphene [77], however this phenomenon will not be discussed in this manuscript.

In addition, logarithmic paramagnetic divergences when the Fermi energy coincides with saddle points of the graphene band structure [19], as shown in figures 2.4, 6.1. This is the consequence of a more general result: paramagnetic orbital susceptibility singularities behaving like the logarithmic van Hove (vH) singularities in the density of states (DOS) were predicted at saddle points of the band structure of any 2D crystalline materials by Vignale [18]. From equation 6.10, the susceptibility follows *grosso-modo* the product of the DOS and the curvature of the band in x and y, this means $\chi \sim -g(E)/m_x m_y$ (see equation 1.15). As

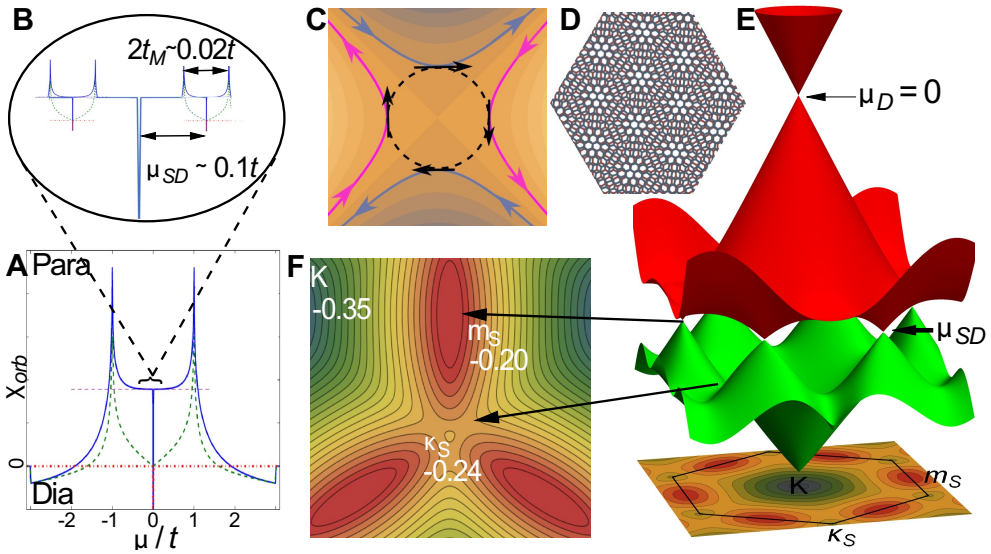

Figure 6.1: (**A**) Orbital susceptibility of graphene. Diamagnetic divergent susceptibility is expected at $\mu = 0$ and paramagnetic divergences at the saddle points at $\mu = \pm t$. (**B**) Schematics of the expected orbital susceptibility of a graphene/hBN moiré at low energy as function of the chemical potential. (**C**) Schematic explanations of the existence of paramagnetic currents in the reciprocal space close to a saddle point in a 2D crystal (from [18]. (**D**) Schematic representation of a moiré lattice obtained with the superposition of two honey-comb lattices of different periods. (**E**) Mini-band structure obtained from the diagonalisation of the low energy hamiltonian of graphene in the presence of a moiré potential of amplitude $t_M = -23mev$. The two highest energy hole bands are represented below the main graphene Dirac point. (**F**) Iso-energy lines in the vicinity of a satellite Dirac point of the second hole band (H2). Close to the κ_s point in the MBZ, an A_1 saddle point is identified.

it was introduced in chapter 1, the intuitive physical explanation of the paramagnetic sign lies in the coexistence of effective masses (m_x and m_y) of opposite signs at the saddle points. In magnetic field, carriers follow diamagnetic hyperbolic trajectories in reciprocal space centered around those points. Tunneling between these trajectories (also called magnetic breakdown [31]) gives rise to quasi-circular paramagnetic trajectories around the saddle points, see figure 6.1.

However, reaching these saddle points in pure graphene requires doping to unattainable Fermi levels of the order of the nearest neighbor hoping energy t=2.7 eV. In practice, this means applying gate voltages of around 10^3 V, if we would like to electrostatically control doping (using BN as dialectric for example).

We show in the following how, by inducing a large wavelength moiré periodicity in graphene aligned to an hBN crystal, we can reach such saddle points in the band structure at reasonable doping and detect the expected singular paramagnetic orbital response.

The moiré lattice parameter of graphene on hBN, a_M, is much larger than the size of the unit cell of graphene, a, see equation 4.2. The moiré potential leads to the formation of low energy minibands centered around each Dirac point in figure 6.1D), and the occurrence of satellite Dirac points (SDP) (at $\mu_S \simeq \pm t/10$). These SDP accessible by applying moderate gate voltages were observed experimentally by several groups including [78, 55].

These SDP are surrounded by saddle points whose associated vH singularities were detected via DOS measurements [78]. The presence of saddle points were also revealed in electron focusing experiments [79] and more indirectly in magnetic field dependent patterns in Josephson junctions [80].

Field dependent peaks in photo-emission spectra[81] as well as in thermoelectric Hall measurements[82] were interpreted as related to orbital magnetization singularities at those low energy vH singularities.

In the following sections we first discuss the general properties of graphene in a moiré potential and then present the results of the magnetism of two samples where the effects of the moiré superlattice are important. We explore a wide range of chemical potential on each one of them. These experiments reveal the paramagnetic susceptibility peaks predicted long ago by Vignale at saddle points of the moiré band structure.

6.2 . Graphene in a moiré potential

In the recent years, the interest for assembled stacks of van der Waals structures has gained a lot of intensity because of the versatility of fabrication and the possibilities of modifying the electronic properties of these 2D materials. It is now possible to stack and combine materials at will enabling to increase the quality of the samples thanks to encapsulation and, on the other hand, to create systems with new properties and potential applications. Many examples can be named, starting

from the well-known twisted bilayer graphene (TBG), where exotic properties have been found [83, 84]. Boron Nitride (BN) has been used as the ideal substrate for graphene. It has many interesting properties: it is atomically flat, it has a huge band gap and it has the same structure as graphene except for a small difference in the size of the lattice. It is precisely this difference that can give rise to a set of features that are not present in isolated graphene (either suspended or on SiO2).

The physical simple explanation is the following: due to the difference in size of the (otherwise) identical lattices, the structure can form an effective moiré superlattice. This means that a geometrical pattern with a larger periodicity emerges from the two original lattices. This superlattice can be modeled as a superpotential which periodicity is given by the size of the moiré lattice. So, the electrons in graphene (the ones that are involved in the electronic properties) feel the usual potential owing to its own lattice but on top of that, they can feel the potential due to the BN substrate. The easiest way to model and understand this is by considering that graphene and BN are two rigid lattices. The small difference in lattice constant in real space will produce a periodic arrangement of the atoms when considering both graphene's and BN's atoms. The lattice parameter of this new superlattice is given by the places where the pattern repeats itself.

Reference [85] gives a clear way to understand and calculate the size of this superlattice, and here we sumarize it as follows: We start from the two identical honeycomb lattices, the BN lattice can be written as an expansion of the graphene lattice. Calling $\vec{a_i}$ the lattice vectors of graphene, BN lattice vectors can be written as $\vec{b_i} = \mathbf{M}\vec{a_i}$, where $\mathbf{M} = (1+\epsilon)\mathbf{I}$, $\epsilon = \frac{a_{BN}-a_g}{a_g}$ and $\mathbf{I}$ is the identity matrix. Moreover, if we want to include the relative rotation of the two lattices, we apply the rotation matrix

$$\mathbf{R} = \begin{bmatrix} \cos\theta & -\sin\theta \\ \sin\theta & \cos\theta \end{bmatrix},$$

so the BN vectors are written $\vec{b_i} = \mathbf{M}\ \mathbf{R}\ \vec{a_i}$. Then, starting in a position where we have AA stacking (white circles in figure 6.2), the displacement $\vec{\delta}$, from the position of an atom of hBN, $\vec{r}_{BN}$, and the graphene atom $\vec{r}_g$ is given by.

$$\vec{\delta} = \vec{r}_{BN} - \vec{r}_g = (1 - \mathbf{R}^{-1}\ \mathbf{M}^{-1})\vec{r}_{BN}. \tag{6.1}$$

If $\vec{\delta}$ is exactly equal to a graphene lattice vector $\vec{a_i}$, this means that the shift of the two lattices has arrived to the point that we are again in an AA stacking (see the other green circles), given a full spacial period of the moiré lattice $\vec{a}_M$.

$$\vec{\delta} = \vec{a_i} = (1 - \mathbf{R}^{-1}\ \mathbf{M}^{-1})\vec{a}_M$$

or equivalently

$$\vec{a}_M = (1 - \mathbf{R}^{-1}\ \mathbf{M}^{-1})^{-1}\vec{a_i} \tag{6.2}$$

and one of the moiré lattice vectors will be given by

$$\vec{a}_{M1} = \begin{bmatrix} 1 - \frac{\cos\theta}{1+\epsilon} & \frac{\sin\theta}{1+\epsilon} \\ -\frac{\sin\theta}{1+\epsilon} & 1 - \frac{\cos\theta}{1+\epsilon} \end{bmatrix}^{-1} \begin{bmatrix} a_g \\ 0 \end{bmatrix}$$

and the norm $a_M = |\vec{a}_M|$ is

$$a_M = \frac{(1+\epsilon)a}{\sqrt{2(1+\epsilon)(1-\cos\theta)+\epsilon^2}}.$$

Then, exactly as in the case of a crystal, we can define the reciprocal lattice vector of the moiré

$$\vec{G}_{Mi} \cdot \vec{a}_{Mj} = 2\pi\delta_{ij}. \tag{6.3}$$

Recalling the fabrication of our moiré samples in section 4.2, the moiré length of the two samples investigated in this thesis are $a_{M_A} = 9.5 \pm 0.5\text{nm}$ and $a_{M_B} = 12.5 \pm 0.5\text{nm}$, which corresponds to misalignments of $\theta_{M_A} = 1.1 \pm 0.1°$ and $\theta_{M_B} = 0.6 \pm 0.1°$.

6.3 . Effective Hamiltonian with moiré periodic potential

In this part, we present details about the model used to describe the band structure of the moiré system. It contains the work done essentially by Jean Noel Fuchs and Frederic Piéchon, and is part of an article in preparation [74]. We will briefly discuss how we obtained the bands structure of the moiré system. We used the approach described in [78, 86]. We start from the effective massless Dirac Hamiltonian, H_0, that is used to describe graphene at low energies in a single valley. We then add a scalar periodic potential V, which represents the effect of the substrate, BN, on graphene. The moiré potential has the periodicity of the moiré structure and is 6-fold symmetric. Here, we consider the only the first order perturbation to graphene's lattice and neglect all the terms that break AB symmetry, following the reference [78]. These symmetry breaking terms are responsible of opening gaps in the band structure [73] that have been observed experimentally [72, 55]. The Hamiltonian is then:

$$H = H_0 + V = v\boldsymbol{p}\cdot\boldsymbol{\sigma} + t_M \sum_{m=0}^{5} e^{i\boldsymbol{G}_m\cdot\boldsymbol{r}}, \tag{6.4}$$

where $\boldsymbol{\sigma}$ are the Pauli matrices describing the sublattice pseudospin of the honeycomb lattice and $\boldsymbol{b}_m = b\{\cos(m\pi/3), \sin(m\pi/3)\}$ are reciprocal lattice vectors with norm G, given by:

$$G \simeq \frac{4\pi}{3a_M}, \tag{6.5}$$

with a_M the moiré length. The momentum operator is the usual $\boldsymbol{p} \to -i\hbar\boldsymbol{\nabla}$ in 2D (it is shifted such that K now plays the role of the reciprocal space origin Γ_S). This formulation is equivalent to the one presented in [86, 85] if we consider only the first correction to the linear effective hamiltonian of graphene.

Figure 6.2 shows a schematic view of the moiré lattice. The graphene lattice, in green, sits on top of the BN, in orange and red. In the background one can see

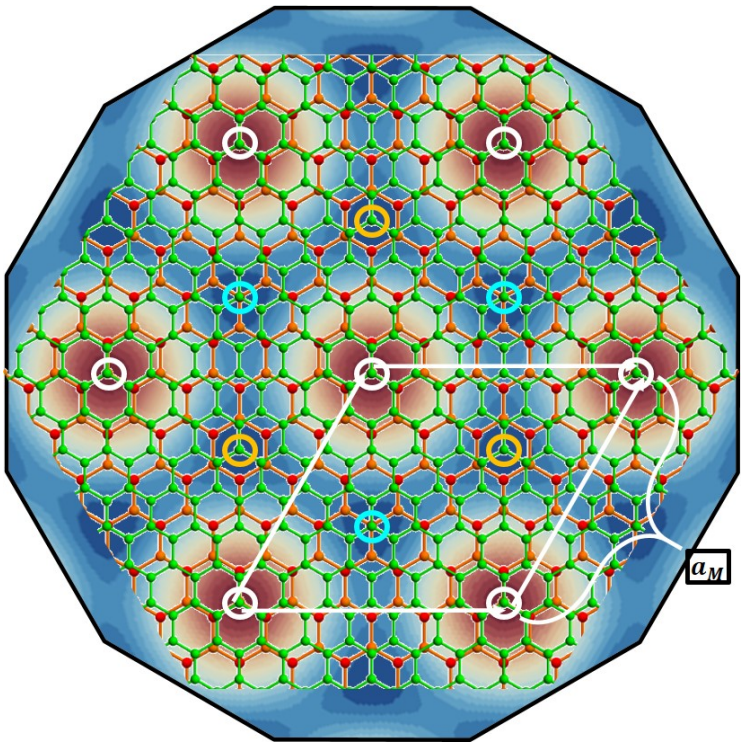

Figure 6.2: Schematics of the moiré superlattice when both graphene and BN are considered rigid. The circles show the regions where the stacking between atoms is special: AA zones are in white, AB in sky blue and the zones where an A graphene atom sits on the center of the BN hexagon in orange (this region is the equivalent of an BA stacking because three equidistant B graphene atoms are the closest here to A atoms of BN). In the background, the potential is ploted as color code. Red (blue) zones represent regions where the potential is negative (positive).

the periodic potential given by the second term in equation 6.4 for $t_M = -23\mathrm{meV}$. Figure 6.2 also shows regions in red represent the minima of the potential. As said before, the potential is modeled in such a way that it reproduces the periodicity of the moiré pattern, however, if we look at the detailed picture, the potential shows a C6 symmetry (inherited from graphene) while the actual moiré superlattice, does not. It has C3 symmetry in real space, inherited from BN. However, this simple hamiltonian is enough to understand our results, as it is studied in reference [78]. A much more precise modelization of this system is developed in reference [73] where the full hamiltonian in [86] and the relaxation proposed in reference [87] are taken into account.

The amplitude of the potential was obtained experimentally as it is explained below. The sign was settled by comparing the transport measurements with the theoretical curves of the density of states calculated in [86]. Thus, a negative sign is given to the potential. This results in a potential where the minima form a triangular lattice, as shown in figure 6.2. This choice of sign is the same one made also in [81].

We can write the potential in terms of the eigenvectors of H_0. These are plane wave spinors $|\vec{k}, s\rangle$, where $s = \pm$ is the sign of the energy $\epsilon^0_{\vec{k},s} = s\hbar v_F k$. The potential then takes the form:

$$\langle \vec{k}', s'|V|\vec{k}, s\rangle = t_M \delta_{s,s'} \sum_{m=0}^{5} \delta_{\vec{k}', \vec{k}+\vec{G_m}}.$$

To calculate the band structure of the moiré system, we use a code written by Fuchs and Piechon [88]. For this, we are only interested in the lowest energy bands, so we limit the calculation by imposing a cutoff in energy. This means that the matrix elements of the potential will only consider $\vec{k}'$ vectors such that, for each $\vec{k}$ in the mini Brillouin zone, $\vec{k} - \vec{k}'$ is a reciprocal lattice vector and $|\vec{k} - \vec{k}'| \leq 2|G|$. This means that for each sign of the energy s, there are 19 states. In total, for each $\vec{k}$ in the moiré Brillouin Zone (mBZ), the diagonalized Hamiltonian has 38 bands. The 6 lowest energy bands are the ones represented in figures 6.5. A 3D representation is also given in figure 6.3.

The hamiltonian in equation 6.4 yields the band structure shown in figures 6.3 and 6.5. We can observe at zero energy, the usual graphene's Dirac cone but the most interesting feature is the emergence of small replicas of this linear behavior. At slightly higher doping (slightly less than $\pm$ 0.2 eV in chemical potential for perfect alignement), because of the action of the moiré potential, secondary Dirac peaks appear. Hamiltonian 6.4 can be seen as replicating the Dirac cone, placing one replica in each one of the moiré harmonics (see section 6.3). Therefore, by increasing the chemical potential, these cones will eventually cross, generating the secondary Dirac points. As we see in figure 6.3, at the borders of the mBZ, the crossing with the neighboring cones alters the band structure in at least two important ways: 1) The emergence of the secondary Dirac cones at the positions

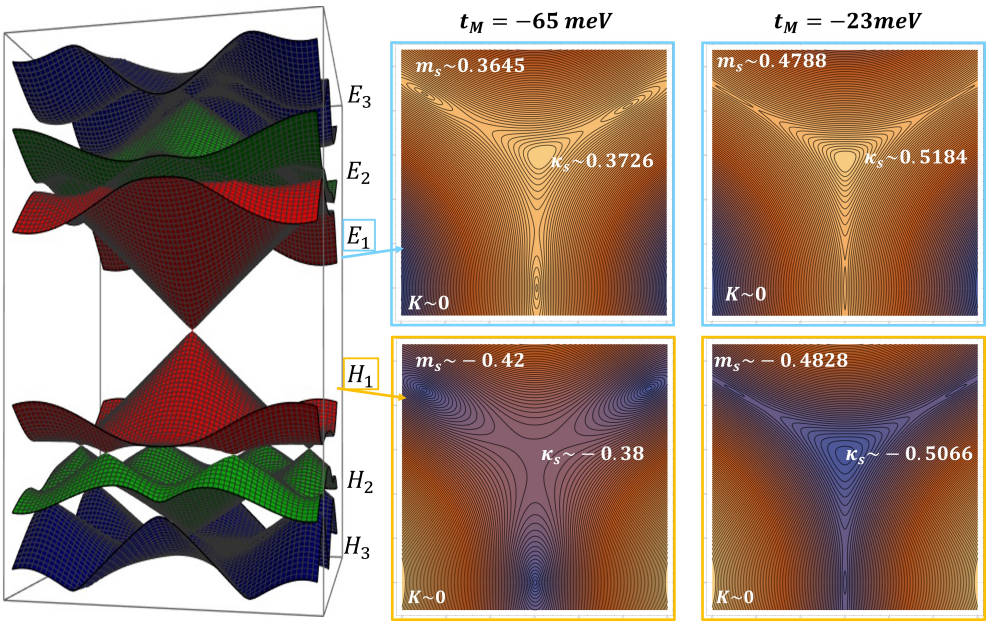

Figure 6.3: 3D representation of the band structure of graphene with a moiré potential obtained from equation 6.4. For two different amplitudes of the moiré potential, the saddle point in the first hole band H1 exhibits a C3 symmetry saddle point which splits into 3 A1 points around κ_S when the amplitude of t_M decresases.

where the bands cross and 2) the appearance of van Hove singularities. We have chosen to extend the traditional notation of the high symmetry points of graphene to the mBZ. This means that in the mBZ corner of the hexagons are called κ_s and the midpoint of the sides are called m_s. See figure 6.1.

We show, also in figure 6.3, the contour plot of the two lowest energy bands for two different potential amplitudes, $t_M \sim -65\text{meV}$ and $t_M = -23\text{meV}$. In the band H_1, we can distinguish the formation of a saddle point of symmetry C_3 for high potential amplitudes. However, it is unstable and it splits into 3 A_1 saddle points for lower values of the potential amplitude.

6.4 . Moiré samples and magnetic detection

We fabricated samples where the hBN and Graphene lattices are nearly aligned, leading to the maximum value of the G/hBN moiré super-lattice parameter as described in section 4.2. We investigated two different samples M_A and M_B. Then, Raman spectroscopy was used to verify the alignment as well to determine the lattice parameters yielding $a_{M_A} = 9.5nm \pm 0.5$ nm and $a_{M_B} = 12.5 \pm 0.5$ nm corresponding to 1° and 0.6° mismatch angles.

The magnetization experiments were performed using the technique described in [17] and discussed in chapters 3 and 4. The encapsulated samples are deposited on a magnetization detector which consists in a pair of highly sensitive gian magnetoresistance (GMR) probes, described in chapter 3. The key point of using these sensors is that whereas the orbital magnetism in the system is generated in response to the perpendicular external field, the GMRs are only sensitive to the in-plane components of the stray field created by the orbital currents. Connecting the two GMR strips in a Wheatstone bridge configuration, as in figure 3.6, and modulating the gate voltage eliminates most of the spurious magnetic contributions from the environment and yields the V_g derivative of the magnetization of graphene below the gate between the GMR probes, as it was mentioned in chapter 4. Two additional electrodes outside the GMR detection zone allow for transport measurements and an independent determination of the main and satellite Dirac points positions. The calibration of the GMRs sensors coupled to M_A and M_B, (respectively 2.5 and 1 Ω/mT), leads to in-plane sensitivity of detection of the order of 1 nT for an applied perpendicular field of 0.1 T.

6.5 . Satellite Dirac spectra, diamagnetic and paramagnetic singularities

We now turn to the higher doping regime. Figure 6.4A shows the 4-terminal resistance of sample M_A in a wide range of gate voltage. The satellite Dirac peaks at $V_g = -16$ V and $V_g = +15.5$ V symmetrical with respect to the main Dirac peak are clearly visible. figure 6.4B, shows the magnetization response at 0.2 T in the same range of gate voltage, using a 100 mV modulation. This strong V_g modulation increases the detection sensitivity at high gate voltage because the chemical potential scales as $\sqrt{V_g}$ but damps the previously discussed diamagnetic McClure response and dHvA oscillations.

In the high doping region of interest here, in particular in the region where the SDP are found in the resistance measurement, we find a series of three antisymmetric peaks, compatible with the expected orbital magnetism of the moiré as shown below. The integrated trace displayed in figure 6.4C clearly features a diamagnetic peak (red arrow) in the hole doped region at $V_g = -17$ V surrounded by two paramagnetic peaks (black arrows). In the electron doped region, we also detect a diamagnetic peak at the SDP but only one clear paramagnetic

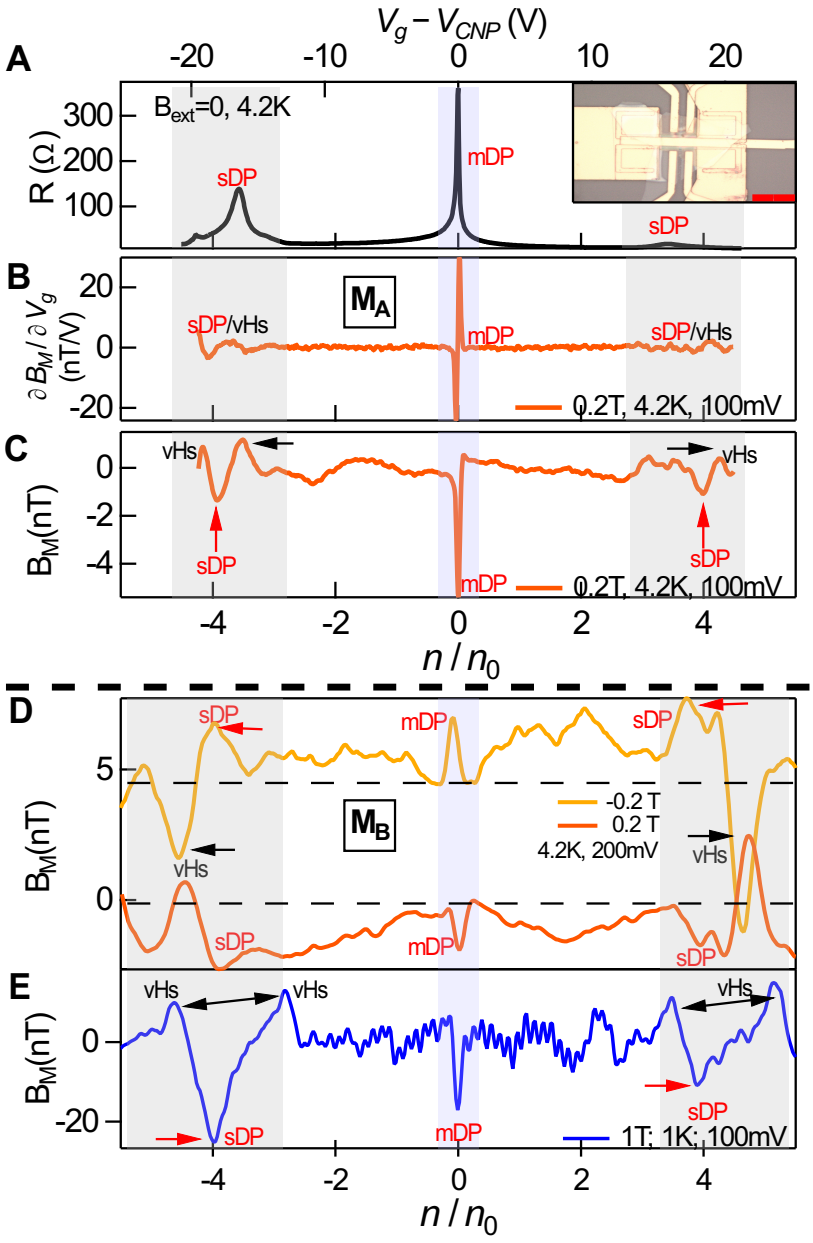

Figure 6.4: **(A)** 4 terminal resistance of sample M_A. **(B)** Derivative of the magnetization as a function of the gate voltage and carrier density (renormalised to n_0) for a large doping range in an external magnetic field of 0.2T for the same sample. **(B)** Magnetization (in units of the magnetic field detected on the GMRs) obtained by numerical integration of the data in (C). Close to the region of the secondary Dirac peaks we observe diamagnetic peaks (right arrows)surrounded by paramagnetic peaks (black arrows). **(D)** GMR data measured on the sample M_B. Numerically integrated magnetization as a function of the carrier density (renormalised to n_0) $\pm$0.2 T and 1 T **(E)**.

peak. From the value of moiré lattice parameter (determined from the Raman spectra, see section 4.2 figure 4.3) we find that the gate voltage positions of the diamagnetic peaks correspond, as expected, exactly to a carrier density of 4 n_0 where n_0 is the number of carriers per moiré cell, (the factor 4 comes from spin and valley degeneracies). The peak positions differ slightly from those observed on the resistance measurements shown in figure 6.4A, a discrepancy we attribute to the different sample region probed in the resistance measurements.

Indeed, since the geometry of the two experiments (transport and magnetism) is different, we may be seeing a slightly different effective moiré length (of about $0.5\mathrm{nm}$) in each experiment. Another possible explanation for this discrepancy might be the possible inhomogeneous strain that is present in the sample. In any case, the difference in the position in doping between magnetization and resistance measurements can be explained by considering the error bars of the calibration of the moiré-length/FWHM relation (see figure S2 in the suplementary information of [55]).

We assign the paramagnetic peaks to the expected magnetic orbital response at the saddle points of the moiré miniband structure. Using the capacitance of sample M_A, we determine the energy splitting between the paramagnetic and diamagnetic peaks and thefore the expected positions of the VHS, to be of the order of 20 meV. This number yields an estimate of the amplitude t_M of the moiré potential [18] and figure 6.1.

Figure 6.4 also presents equivalent data on sample M_B.There, as well dHvA oscillations are attenuated by the gate voltage modulation of 100 mV and invisible at (± 0.2 T) , but are visible at 1 T due to their larger period. At high hole and electron doping one clearly identifies, three peaks of similar amplitude. The position of the diamagnetic satellite peaks are consistent with transport data (shown in SM) and with a moiré period larger than that of sample M_A. There as well, the diamagnetic peaks at the SDP are surrounded by paramagnetic singularities expected from vHS at the saddle points of the band structure.

The data taken at lower field, at ± 0.2 T display peaks of opposite sign, approximately at the same positions and with 5 times smaller amplitude than the 1T data which is consistent with a linear field dependent magnetization. However, in contrast with the 1 T data, the inner smaller paramagnetic peaks are nearly undetectable at $\pm 0.2T$. We note that at 1T the magnetic energy scale ϵ_B is equal to 30 mV i.e. of the order of the moiré potential, which means that the miniband spectrum is modified in a non perturbative way at this field. This can explain that the data at 1T is significantly different from the the lower field data. In the following, we discuss possible explanations for these asymmetries in amplitude of paramagnetic singularities on either side of satellite Dirac peaks. We note that these asymmetries were also observed in vH singularities detected through DOS experiments [78].

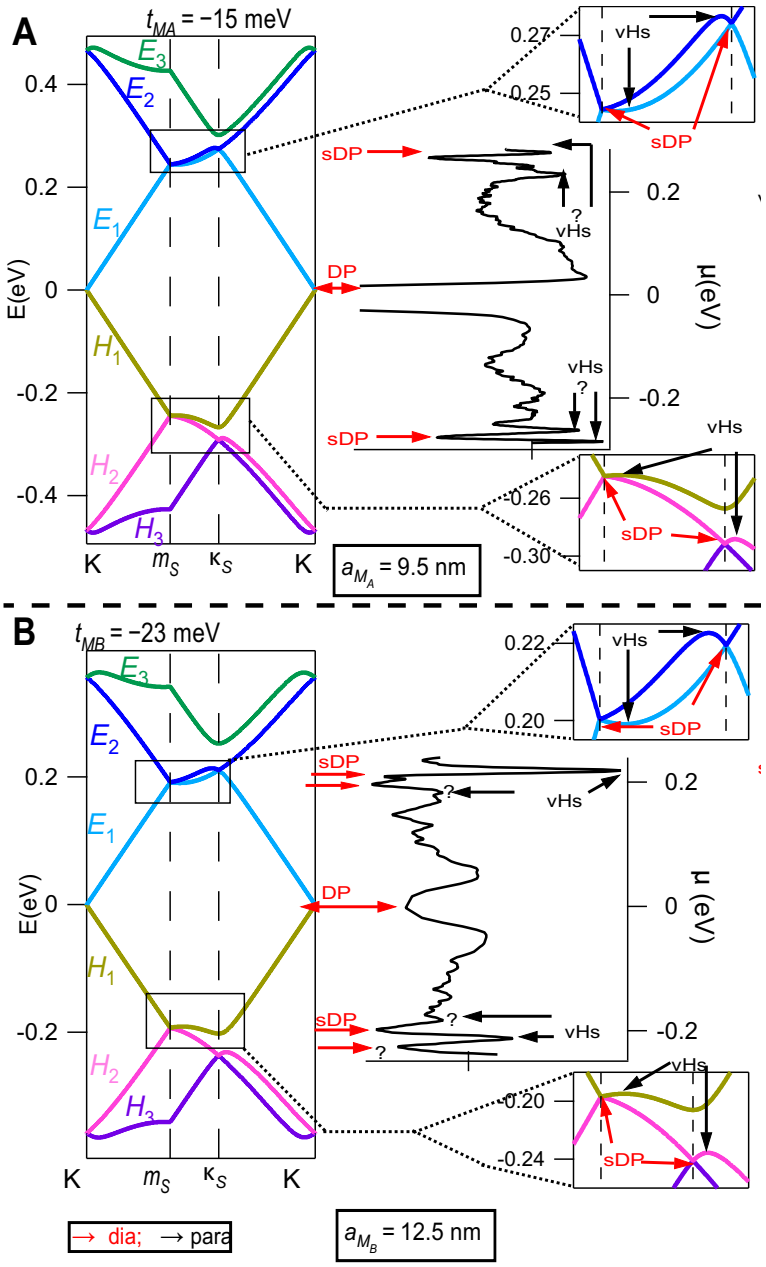

Figure 6.5: **(A)** and **(B)** Magnetization data on samples M_B and M_A measured at 0.2 T plotted as a function of the chemical potential given in eV. (We note due to the $\sqrt{V_g}$ dependence, the energy width of satellite Dirac points is smaller than the width of the main Dirac point.) The difference between the chemical potential of the SDP of the samples M_B and M_A is directly related to their different periodicity $a_M = 12.5nm$ nm and 9.5 nm respectively. Experimental data are compared to cuts along the κ_S, m_S axis of the moiré band structure calculated for different values of t_M matching the position of the observed diamagnetic peaks (red arrows) and paramagnetic peaks (black arrows) of both samples.

6.6 . Comparison with a simple theoretical model

Computations of moiré spectra rely on specific modelisations of the moiré potential [78, 86, 87, 85]. In the following, we propose to use the simplest model which reproduces the positions and amplitudes of the different susceptibility peaks at the Dirac and saddle points which are the primary focus of our experimental measurements. This model initially derived in [78] is the same model we described above in section 6.3. The miniband spectrum, folded into the moiré Brillouin zone, can be easily calculated within this approximation as shown in section 6.3. The amplitude of the moiré potential affect the number and position of the Dirac satellite points as well as the symmetry of the saddle points. These features also depend on the minibands considered on electron or hole doping sides, [78, 86, 81] and section 6.3. When increasing the amplitude of the moiré potential, t_M one finds a clear electron- hole asymmetry of the energy minibands spectrum determined by the sign of t_M. This is illustrated in figure 6.5 showing cuts along the κ_S, m_S axis of the three lowest moiré electron and highest hole bands around the Dirac point. For negative values of t_M the bands of the moiré minibands are wider on the hole compared to the electron side.

Whereas crossings occur essentially between the first and the second bands on the electron side, they also occur between the second and third band on the hole side. These crossings determine the number and position of the satellite Dirac points in the reciprocal space. For small values of t_M these crossings occur both at κ_S and m_S points for the first two electron bands, see the bands in figure 6.5 and 6.6, for example. These points are separated by ordinary saddle points giving rise to logarithmic vH singularities, shown in 6.6. These saddle points connecting 2 valleys are called A_1 following [89].

By contrast, the first hole miniband H_1 below the main Dirac peak does not exhibit a Dirac point at κ_S but instead a C_3 saddle point which can be viewed as the merging of three A_1 saddle points. C_3 saddle points are characterized by energy varying as a cubic function of the wave-vector (2nd order curvature cancels in all directions) yieding a plateau surrounded by 3 maxima separated by 3 valleys at 120 degrees (see figure 6.3, 6.7 as well as [89], for the classification of saddle points). When $|t_M|$ is small, one can note the presence of an extra shallow dip at κ_S (black arrow in figure 6.5 on the H1 band) probably due to the coupling between that band and the lower energy bands crossing at κ_S.

Coming back to experiments, in figure 6.5 we attempt to match, for both samples, the position of the measured diamagnetic and paramagnetic satellite peaks with their expected positions in the moiré band structure, taking t_M as an adjustable parameter.

The calculated bands which best match the experimental positions of the different peaks are obtained for $t_M = -15\ meV$ and $t_M = -23\ meV$ for samples M_A and M_B as shown in figure 6.5. These values are obtained directly from measuring the distance between diamagnetic and paramagnetic peaks in figure 6.5. For

these values of t_M we expect crossings between the E1 and E2 bands both at κ_S and M_S points yielding 2 families of satellite Dirac points. Since these crossings occur at different energies, a splitting of the diamagnetic satellite McClure peak is expected and is compatible with what is measured experimentally in figure 6.5 on the electron side for bands E1 and E2. Larger splittings observed on the hole side correspond to the crossings between H2 and H3.

Moreover scrutinizing the shape and curvature of the minibands figure 6.5, 6.6 and 6.7, we can understand the asymmetry of the positions and amplitudes of the paramagnetic singularities, clearly more pronounced on the high doping sides of SDPs (bands E2 and H2). From one side, the curvature in the bands E1 and H1 is strongly asymmetric. More precisely, the curvature following the $m_s - \kappa_s$ axis or is around 100 and 70 times smaller than the perpendicular direction, for samples M_A and M_B respectively. By contrast, in bands E2 and H2 the curvature is similar in the two perpendicular directions. On the other hand, saddle points in bands E1 and H1 are closer to the secondary Dirac point, and given their finite width, diamagnetic and paramagnetic contributions tend to cancel whereas the paramagnetic peaks in E_2, H_2 are further in energy from the SDP and can be resolved. This asymmetry is enhanced by disorder and by a high value of modulation. This explains why the outer paramagnetic peaks around the satellite Dirac points are more intense than the inner ones.

At present our experiments are not accurate enough to investigate in detail the shape of paramagnetic singularities, but we can nevertheless compare the typical amplitudes of the measured magnetization singularities to theoretical predictions. To this end, we first compare the theoretical ratio between the diamagnetic peaks at the main at satellite Dirac points with the experimental values. According to reference [17, 12] the orbital magnetic susceptibility of graphene at the Dirac point, χ_D, depends on the square of the Fermi velocity and the disorder standard deviation σ_0 according to:

$$\chi_D = -\frac{\sqrt{2} v_{F_D}^2 e^2}{3\sigma_0 \pi^{3/2}} \tag{6.6}$$

It was pointed out in [78] that the satellite Dirac cones (at the m_S points of the moiré hexagonal Brillouin zone) are anisotropic, with elliptical cross sections leading to an effective Fermi velocity: $v'_{F_S} = \sqrt{v_{sx} \times v_{sy}}$. These anisotropic components of the Fermi velocity along the principal axis of the elliptical energy cross sections in the vicinity of SDP are $v_{sx} = v_{F_D}$, the original Fermi velocity of graphene and

$$v_{sy} = \frac{\sqrt{3} a_M t_M}{2\pi\hbar}, \tag{6.7}$$

the reduced transverse velocity originating from the moiré potential. We then assume that the susceptibility, χ_S, at secondary diamagnetic peaks, is similar to the McClure susceptibility of graphene in Eq.6.6 replacing v_{F_D} by $\sqrt{v_{sx} \times v_{sy}}$ and the amplitude of disorder σ_0 by σ_s, of the order of $4.5\mathrm{meV}$ and $5\mathrm{meV}$ for samples

M_A and M_B respectively. This leads to the susceptibility ratio for the diamagnetic peaks

$$r_{dia} = \chi_S/\chi_D = 3\frac{v_{sy}\sigma_0}{v_{F_D}\sigma_s}. \tag{6.8}$$

Where the factor 3 comes from considering the 3-fold degeneracy of m_s points. The values obtained are $r_A = 0.28$ and $r_B = 0.52$, for samples M_A and M_B, of the order of 2-3 times the experimental values 0.09 and 0.33. For these estimations we have not taken into account the contribution of Dirac points at the κ_S points.

These experimental values have been obtained from the results obtained at 0.2 T. The amplitude of the secondary diamagnetic peaks were obtained from the plots in figure 6.4 for both samples. The main diamagnetic peaks were taken from figure 5.13, for M_A, and a similar *low-modulation* curve for sample M_B. We estimate the value of the parameter σ_S also from experimental results. This parameter has the same meaning of σ in section 5.1 and 5.2 in monolayer graphene, i.e., it is the standard deviation of the gaussian distribution of the chemical potential. As it was also mentioned in section 5.1 and 5.2, σ is a measure of the disorder associated to the presence and screening of charged impurities. We find that σ_S is larger than σ_{inf} describing the damping of the de Haas-van Alphen oscillations. It is possible that the moiré potential introduces extra disorder not present in pure graphene. In the case of these samples, we can measure the width of the derivative of the secondary diamagnetic peaks and extract the value of σ_S, as it is shown in figure 6.8.

Turning to the paramagnetic susceptibility peaks, we can estimate their amplitude from the miniband spectrum determined in our simple model by the parameters t_M and a_M. The DOS and the susceptibility both depend on the product $\alpha_x\alpha_y$ of the curvatures of the energy bands at the saddle points. As an exemple, for the E2 band which has the highest curvatures at the A_1 saddle points (see figure 6.7), these values are α_x = 4.7 $t_M a_M^2$ and α_y -1.5 $t_M a_M^2$, instructive to compare with the inverse of the free electron mass m_e. We find, α_x = -3.13 α_y = 100 m_e^{-1} and 265 m_e^{-1} for respectively samples M_A and M_B.

In order to go further and compare these findings to the experiments we have also to consider the effect of disorder and degeneracy of saddle points. From the value of the ratio σ_S/t_M estimated experimentally to be of the order of 0.15, we find that the amplitude of the paramagnetic magnetization at A_1 saddle points is expected to be of the same order of magnitude as the diamagnetic peak at the SDP in agreement with our experimental results. In order to obtain σ_S, we approximate the diamagnetic secondary peak as a gaussian. Then, the distance between the maximum and the minimum of the derivative of a gaussian is 2σ, see figure 6.8.

We present tables 6.1 and 6.2 to summarize the parameters that are involved in the estimation of the amplitudes of the peaks. They contain the numerically calculated curvatures, velocities and ratios for the bands E1, E2, H1, H2 for both samples. These parameters appear in equations 6.6, 6.7 and 6.23. Here we have expressed the velocities in units of graphene velocity v_F. The parameter α, which

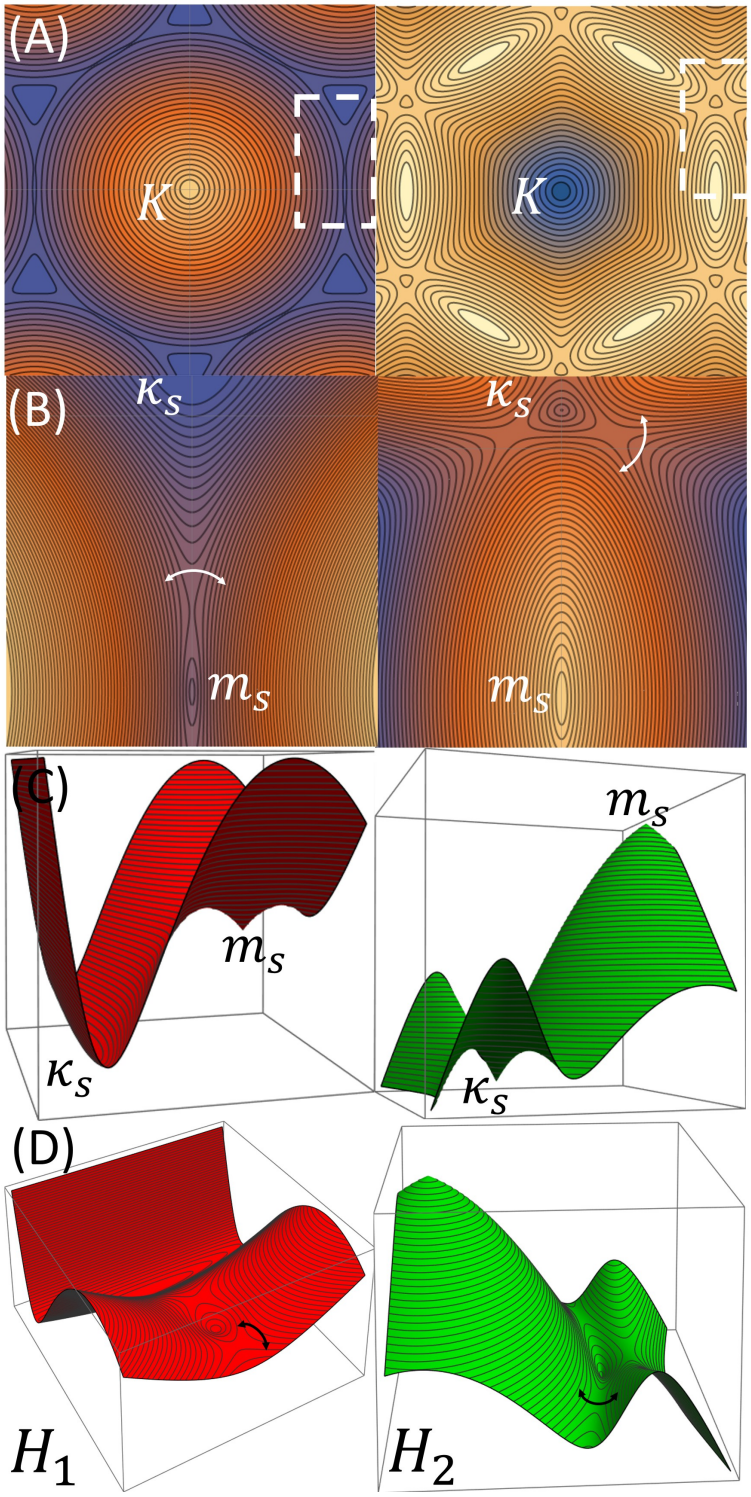

Figure 6.6: (A) Contour plot of bands H_2 (left) and H_1 (right) in the mini Brillouin zone for $t_M = -23\mathrm{meV}$. (B) Zoom around κ_s and m_s points. (C) and (D) 3D representation of the bands close to κ_s and m_s. The curved double arrow indicates the saddle point.

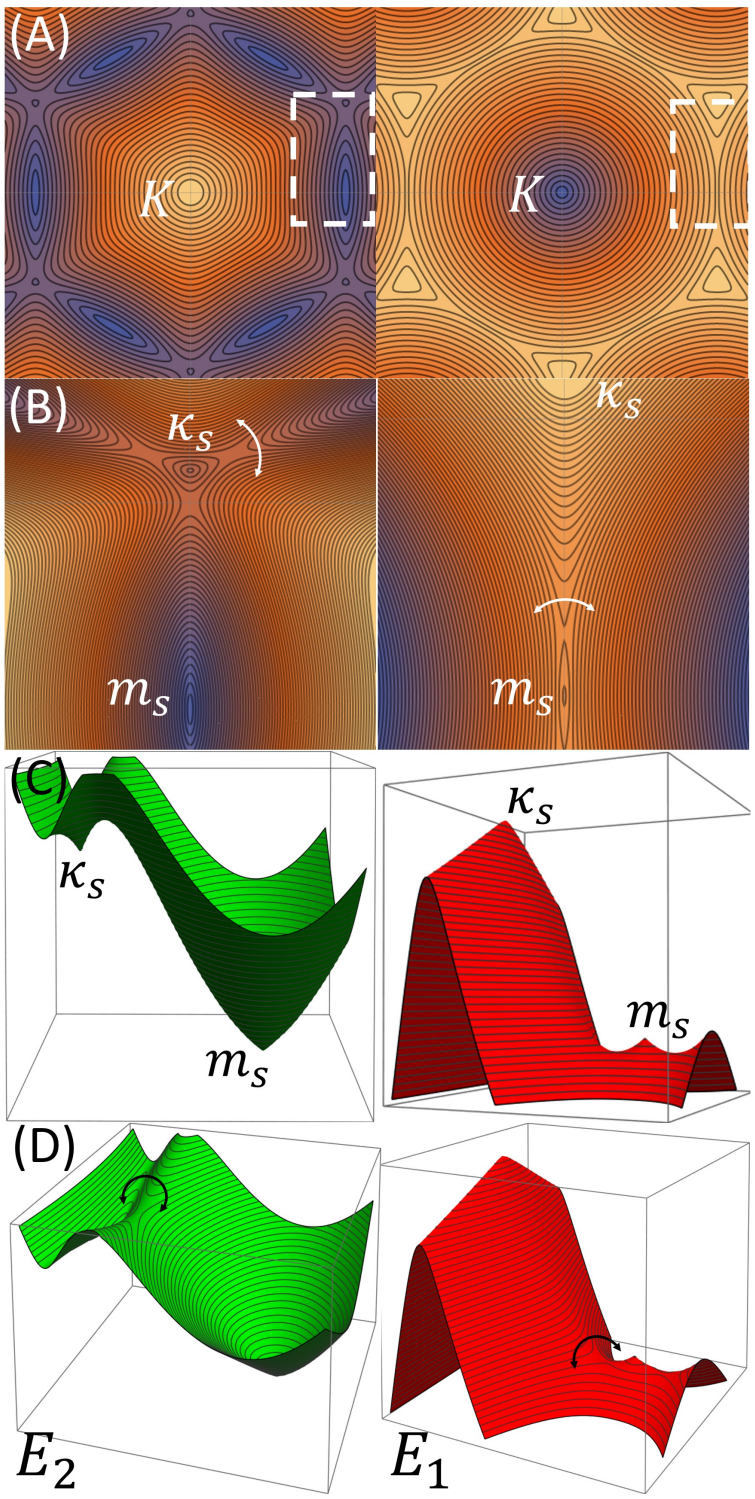

Figure 6.7: (A) Contour plot of bands E_1 (left) and E_2 (right) in the mini Brillouin zone for $t_M = -23\mathrm{meV}$. (B) Zoom around κ_s and m_s points. (C) and (D) 3D representation of the bands close to κ_s and m_s. The curved double arrow indicates the saddle point.

is the inverse of the effective mass, is shown in units of $v_F/\hbar G$. The values of v'_{F_s} and α are the geometrical averages of these values in the x and y directions. This means that $v'_{F_s} = \sqrt{v_{sx} \times v_{sy}}$ and $\alpha = \sqrt{\alpha_x \times \alpha_y}$.

The values in these tables allow us to compare the amplitudes of the different peaks we have found and give an estimate of the relation between them. These data support the comparison of the amplitudes of the observed peaks that we mentioned early. Additionally, we can define the ratio between paramagnetic 1.15,(and below in 6.23) and diamagnetic 6.6 susceptibilities by

$$r_{p/d} = \frac{v_F G \hbar \sigma_s}{4t_M^2} \sim 1. \tag{6.9}$$

M_A	v_{sx}	v_{sy}	v'_{F_s}	α_x	α_y	α	$\alpha v'^2_{Fs}$	$\lvert t_M \rvert \alpha / v'^2_{F_s}$
E_1	1	0.07	0.26	-150	1	12	0.85	6.1
E_2	1	0.07	0.26	25	-7	13.2	0.92	6.6
H_1	1	0.07	0.26	200	-1	14	0.98	7
H_2	1	0.07	0.26	23	-10	15	1.1	7.6

Table 6.1: Theoretical parameters for sample M_A, with $t_M = -15\mathrm{meV}$.

M_B	v_{sx}	v_{sy}	v'_{F_s}	α_x	α_y	α	$\alpha v'^2_{Fs}$	$\lvert t_M \rvert \alpha / v'^2_{F_s}$
E_1	1	0.1	0.32	-70	1	8.4	0.84	5.4
E_2	1	0.1	0.32	16	-5	8.9	0.89	5.7
H_1	1	0.15	0.38	60	-1	7.7	1.16	3.3
H_2	1	0.15	0.38	12	-6	8.5	1.3	3.6

Table 6.2: Theoretical parameters for sample M_B, with $t_M = -23\mathrm{meV}$.

In addition, we can also summarize the parameters extracted and used in the comparisons from the experimental point of view in tables 6.3 and 6.4. The values of $\Delta\mu_{i_{E,H}} \equiv |\mu_{para,i} - \mu_{dia,i}|_{E,H}$ (in meV) are obtained from the distance in energy between the chemical potential of the paramagnetic and corresponding diamagnetic peaks for each band (when they are visible). The subindices i indicates the band for each side of the doping: E_1, E_2, H_1, H_2. The value of σ_S, from the distance in energy between maxima and minima of the chemical potential derivative of the secondary diamagnetic peaks. The amplitudes of the magnetization M_i (in nT) are measured directly from the curves of the magnetization. All the values are obtained at an external field of $0.2\mathrm{T}$. From the amplitudes given in these tables, we can calculate the experimental $r_{p/d}$. For all the peaks, these ratios are between 0.3 and 1.8, the same order of magnitude of the theoretical ratio 1 introduced in equation 6.9.

M_A	$\Delta\mu_1$	$\Delta\mu_2$	σ_S	$\lvert M_{CNP}\rvert$	$\lvert M_{sDP}\rvert$	$\lvert M_{para-1}\rvert$	$\lvert M_{para-2}\rvert$
$E_{1,2}$	N.A.	12	4.8	15	1.3	0.5 $\pm$ 0.5	0.5 $\pm$ 0.5
$H_{1,2}$	13	>10	5	"	1	1.2$\pm$ 0.5	1 $\pm$ 0.5

Table 6.3: Experimental parameters for sample M_A. $\Delta\mu_i = |\mu_{para,i} - \mu_{dia,i}|$ and σ_S are given in meV. The amplitudes of the magnetization at charge neutrality point M_{CNP}, at the secondary Dirac points M_{sDP}, and the paramagnetic peaks $M_{para-1,2}$ are given in nT.

M_B	$\Delta\mu_1$	$\Delta\mu_2$	σ_S	$\lvert M_{CNP}\rvert$	$\lvert M_{sDP}\rvert$	$\lvert M_{para-1}\rvert$	$\lvert M_{para-2}\rvert$
$E_{1,2}$	N.A.	23	4	5.6	1.8	N.A.	3.3
$H_{1,2}$	N.A.	14	5	"	1.7	N.A.	1.7

Table 6.4: Experimental parameters for sample M_B. $\Delta\mu_i = |\mu_{para,i} - \mu_{dia,i}|$ and σ_S are given in meV. The amplitudes of the magnetization at charge neutrality point M_{CNP}, at the secondary Dirac points M_{sDP}, and the paramagnetic peaks $M_{para-1,2}$ are given in nT.

We finally note that the large miniband curvatures due to the large period of the moiré potential contrast with the curvatures at the saddle points of the 2D original atomic lattice [18], and exclude any sizable contribution of Pauli magnetism at vH singularities. The Pauli susceptibility χ_P is indeed expected to vary as $\chi_P = \mu_B^2 \rho(\epsilon)$ where $\mu_B = e/m_e$ is the Bohr magneton, yielding a ratio between the orbital and spin susceptibility $\chi_{Orb}/\chi_P = \alpha_x \alpha_y m_e^2$ of the order of 10^4, whereas this ratio is of the order of 1 for the 2D square lattice.

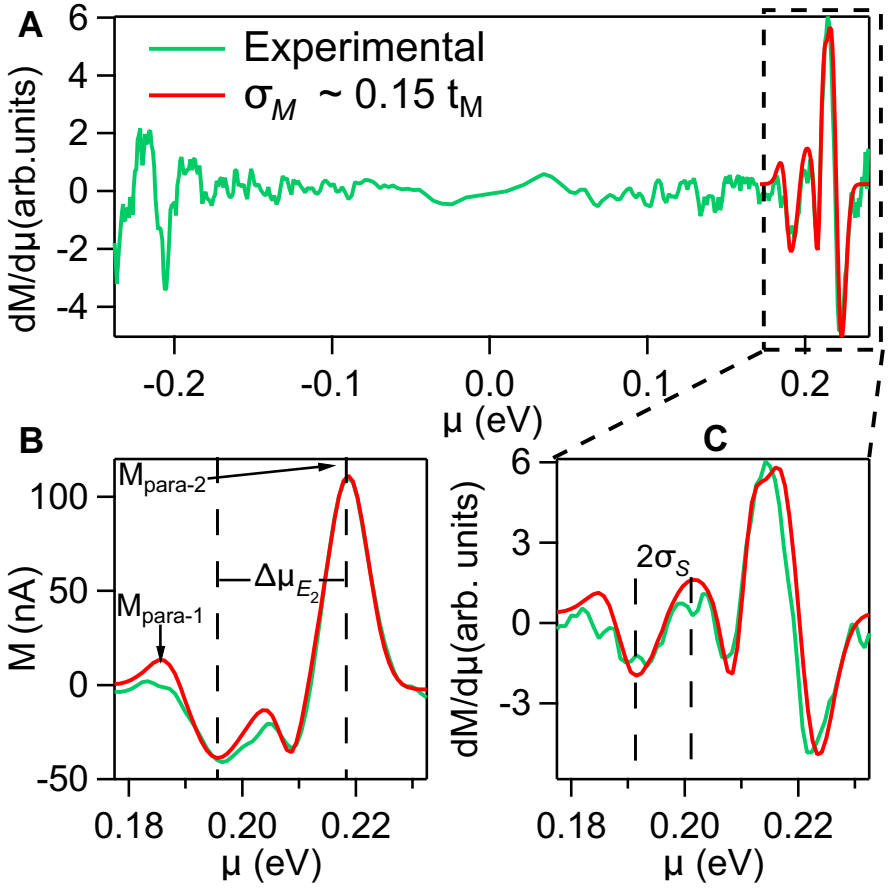

Figure 6.8: (A) In green, derivative of the magnetization as a function of the chemical potential for sample M_B. In red, derivative of the model of 4 peaks (2 paramagnetic and 2 diamagnetic) constructed in the secondary Dirac zone. (B) Integral of the zone in a dashed rectangle in figure (A) as well as the integral of the model. (C) Zoom of the rectangle zone in figure (A). The experimental curve gives a value of $\sigma_S = 4\mathrm{meV}$ approximately.

6.7 . Theoretical calculation of the orbital paramagnetism

Landau-Peierls susceptibility for a saddle point A1

Landau-Peierls susceptibility can be written as [21]:

$$\chi_{LP} = \frac{e^2}{12\hbar^2}\int_{BZ} g'(E_k)\left(\frac{\partial^2 E_k}{\partial k_x^2}\frac{\partial^2 E_k}{\partial k_y^2} - \left(\frac{\partial^2 E_k}{\partial k_x \partial k_y}\right)^2\right)\frac{d^2k}{4\pi^2} \tag{6.10}$$

The dispersion relation in the vicinity of a van Hove singularity varies depending on the type of singularity [89]. Our vHs are going to be treated as type A1, despite the theoretical possibility of hosting a C3 type. This means that the dispersion takes the form

$$E = \alpha(p_x^2 - p_y^2) \tag{6.11}$$

where α represents the inverse of a mass $\alpha = 1/2m$. By inserting 6.11 into 6.10, we can see that the term in between parenthesis in the integral is constant and equal to $4\alpha^2\hbar^4$. In this way, equation 6.10 reduces to calculate the integral of the derivative of the density of states. This later can be written as

$$\rho(\epsilon) = \int \delta(\epsilon - \epsilon(\vec{p}))\frac{d^2p}{4\pi^2} \tag{6.12}$$

with $\delta(\epsilon)$ the Dirac delta function. We can invert the order and integrate first, so the integral in energy can be written as

$$N(\epsilon) = \int \Theta(\epsilon - \epsilon(\vec{p}))\frac{d^2p}{4\pi^2} \tag{6.13}$$

where $\Theta(\epsilon)$ is the Heaviside function. In Cartesian coordinates, and using 6.11, it takes the form

$$N(\epsilon) = \int_{\alpha(p_x^2 - p_y^2)<\epsilon} \frac{dp_x\, dp_y}{4\pi^2} \tag{6.14}$$

In order to integrate the density of states, a cutoff energy must be introduced, it is $\epsilon_c = \alpha p_c^2$. Also, it is convenient to pass to polar coordinates (p, θ). So, by taking $p_x = p\cos(\theta)$, $p_y = p\sin(\theta)$, we get for the dispersion relation of 6.11:

$$E = \alpha(p_x^2 - p_y^2) = \alpha p^2\cos(2\theta) \tag{6.15}$$

and so the integrated density of states can be written as

$$N(\epsilon) = \frac{4}{4\pi^2}\int_0^{\pi/4} d\theta \int_0^p pdp \tag{6.16}$$

with the condition that $\alpha p^2\cos(2\theta) < \epsilon$. The factor 4 in front of the integral appears because there are 4 zones of integration. So, integrating p in this limit

$$N(\epsilon) = \frac{\epsilon}{2\pi^2\alpha}\int_0^{\pi/4} \frac{d\theta}{\cos(2\theta)}. \tag{6.17}$$

Because of the divergence of the integral at $\theta = \pi/4$, here we must introduce the cutoff. This takes the form

$$\theta_c = \frac{1}{2}\arccos\frac{\epsilon}{\epsilon_c} \simeq \pi/4 - \frac{\epsilon}{\epsilon_c} \tag{6.18}$$

and so 6.17 becomes

$$N(\epsilon) = \frac{\epsilon}{2\pi^2\alpha}\int_0^{\theta_c}\frac{d\theta}{\cos(2\theta)}. \tag{6.19}$$

from where we can find

$$\lim_{x\to 0}\int_0^{\pi/4-x}\frac{d\theta}{\cos(2\theta)} = \frac{1}{2}\ln\frac{1}{x} \tag{6.20}$$

so that the integrated density of states is

$$N(\epsilon) = \frac{\epsilon}{4\pi^2\alpha}\ln\frac{2\epsilon_c}{|\epsilon|} \tag{6.21}$$

and so taking the derivative with respect to the energy, we find

$$\frac{\partial N}{\partial\epsilon} = \rho(\epsilon) = \frac{1}{4\pi^2\alpha}\ln\frac{B\epsilon_c}{|\epsilon|}, \tag{6.22}$$

and by re-inserting this and 6.11 in equation 6.10, we get

$$\chi(\epsilon) = \frac{e^2\hbar^2}{12\pi^2}\alpha\ln\frac{B\epsilon_c}{|\epsilon|} \tag{6.23}$$

with $B \simeq 2/\mathrm{e}$, with e the Euler's constant. This is in agreement with the result obtained by Vignale [18].

6.8 . Additional data

In this section we will present some additional data that can help us support our conclusions from the previous sections. We start by presenting the derivative of the resistance from sample M_B. This allows us to directly compare the positions (in gate voltage) of the main and secondary Dirac peaks with the corresponding diamagnetic peaks. At CNP, we see in the resistance a positive derivative. In magnetization, it has associated a negative derivative. It corresponds to the McClure peak. At higher doping, we see in resistance the positive derivatives corresponding to the secondary Dirac peaks. In magnetization, we see various derivatives corresponding to both seconday McClure peaks and paramagnetic peaks. When this magnetization curve is integrated, it gives the curve shown in figure 6.4D for 0.2 T.

We now consider on the same data the effects of modulation and integration. Figure 6.10 compares the integrated curve of data in 6.9 with data taken obtained for a smaller range of gate voltage and with a smaller modulation. It also shows

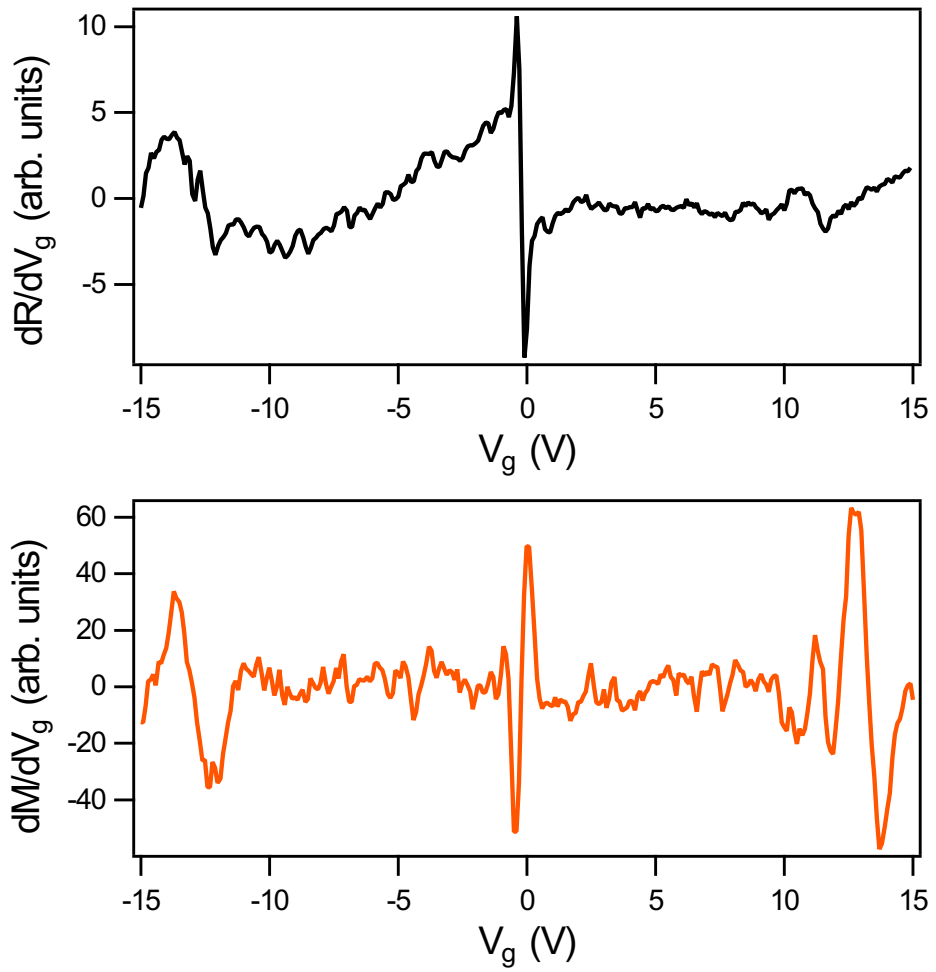

Figure 6.9: Top: derivative of the resistance as a function of the gate voltage for sample M_B. Bottom: derivative of the magnetization as a function of the gate voltage for the same sample.

the effect of performing the integration by separating the curve in 3 pieces. We can notice that the higher modulation allows us to obtain a smoother curve with less noise, but certain structures get rounded in a non-negligible way. Also, when integrating over the full range of gate voltage, we may accumulate errors that can result in the distortion of some small features. This might be taken as additional explanation on why it is more difficult for our experiment to observe the inner paramagnetic peaks in vHs related to bands E_1 and H_1, as compared to E_2 and H_2.

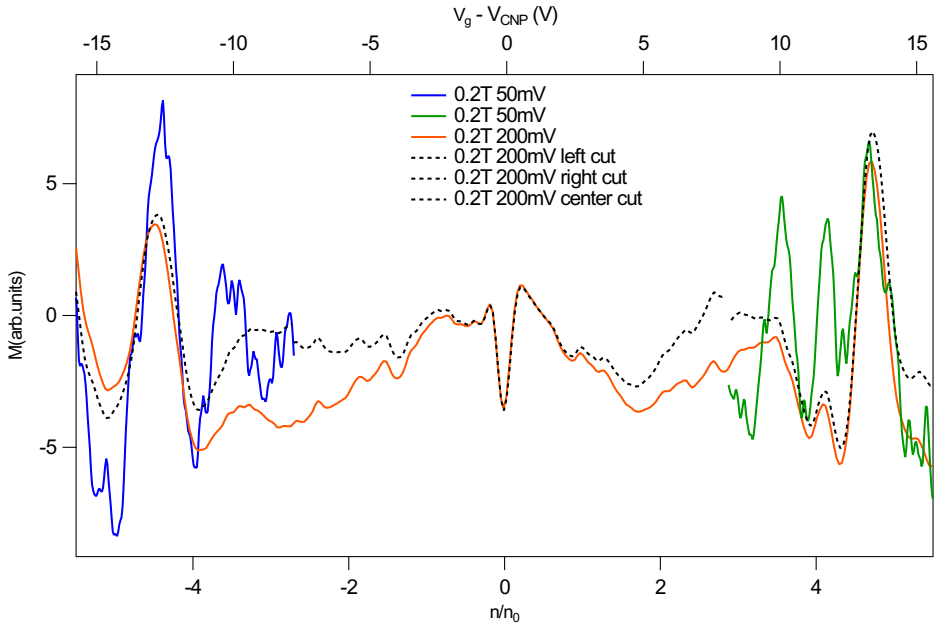

Figure 6.10: Comparison of the magnetization of sample M_B, between different modulations, for an external field of $0.2\mathrm{T}$. In orange, the curve at $200\mathrm{mV}$ integrated in the full range of gate voltage it was measured (-15.5 to 15.5 V), the same shown in figure 6.4. In blue, the electron's (left) SDP region measured at $50\mathrm{mV}$ and integrated in a range between -16 to -8 V. In green, the hole's (right) SDP region measured at $50\mathrm{mV}$ and integrated in a range between 8 to $16\mathrm{V}$. In dashed black, the integration of the data at $200\mathrm{mV}$ was separated in 3 regions: left (-16 ; -8)V, center (-8 ; 8)V and right (8 ; 16)V.

7 - Orbital magnetism in AB bilayer graphene

The present chapter is dedicated to the experimental study of the orbital magnetism of bilayer graphene (BLG).

Earlier, in chapter 1, we discussed briefly how different shapes in the band structure lead to very interesting and different forms of the orbital susceptibility. In this regard, a particular mention should be addressed to bilayer graphene, whose band structure presents all the aforementioned peculiarities within energy ranges that should be experimentally accessible. However, for this to be realized, the energy resolution of the measurement techniques need to be able to separate these features, and the amplitude of disorder has to be small enough. Although from its early experimental years it has been an interesting system to study, nowadays the study of bilayer graphene has gained momentum thanks to the improvement in fabrication that has led to cleaner samples. There is a number of examples of recent works focused on BLG, for example [90, 91], just to name a few. In most of these cases, the key property that makes BLG so valuable is the possibility to create a band gap, by applying an electric displacement field and at the same time, to precisely control the chemical potential through two gates. This relative simplicity in the fabrication makes the experiments reproducible and BLG a good experimental platform.

Before going into the detail, let us start from some general concepts.

7.1 . General properties of bilayer graphene

As the name already suggest, BLG is formed by two layers of graphene. These layers are coupled together by van der Waals forces that arise between the p_z orbitals in the monolayer. The crystaline structure of BLG follows that of monolayer graphene, this means that it is formed by two honeycomb lattices one on top of the other. We can consider BLG as a triangular lattice, whose basis is composed by 4 atoms (see figure 7.1). The most stable configuration of these two layers is the so called Bernal or AB stacking. This corresponds to a configuration in which the atoms sub-lattice A_2 in the top layer (2) are located directly on top of atoms of sub-lattice B_1 in the bottom layer (1). The atoms of sub-lattice B_2 are located on the center of the hexagons of layer 1. A graphic representation of the structure of bilayer graphene is shown in figure 7.1. Bilayer graphene's lattice vectors are the same as in the monolayer, with the difference that this time the unit cell contains 4 atoms, instead of 2. Figure 7.1a shows a possible definition of lattice vectors starting from a site where A2 and B1 atoms are located. Similarly yhan for the case of monolayer graphene, we can construct the tight binding model for bilayer graphene. As we are interested in the low energy behavior, it is sufficient to consider an effective Hamiltonian close to the K points. The effective tight

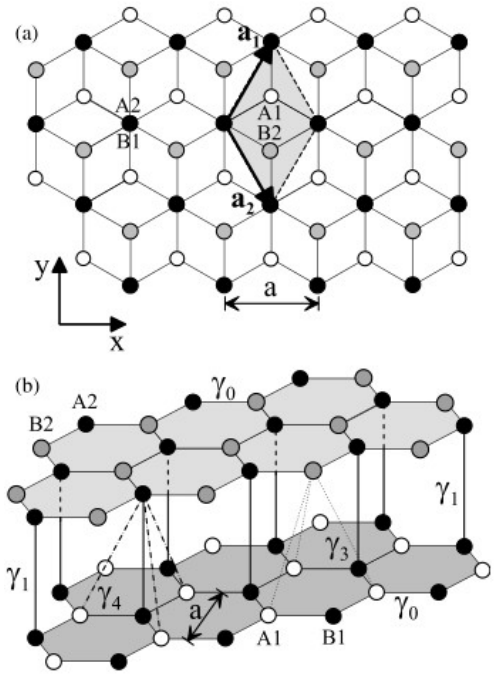

Figure 7.1: Schematic views of the lattice structure of bilayer graphene. (a) top view and (b) lateral view. Solid black dots correspond to dimer sites whereas gray and white are the non-dimer sites. Adapted from [92]

binding Hamiltonian close to the K point is [92]:

$$\hat{H}_{BLG} = \begin{bmatrix} \epsilon_{A1} & v\pi^\dagger & -v_4\pi^\dagger & v_3\pi \\ v\pi & \epsilon_{B1} & \gamma_1 & -v_4\pi^\dagger \\ -v_4\pi & \gamma_1 & \epsilon_{A2} & v\pi^\dagger \\ v_3\pi^\dagger & -v_4\pi & v\pi & \epsilon_{B2} \end{bmatrix} \tag{7.1}$$

where we introduced the velocities $v_i = \sqrt{3}a\gamma_i/2\hbar$. The quantities γ_i represent the hopping parameters between the different pair of neighboring atoms. For example, $\gamma_0 \sim 3\text{eV}$ is the hopping integral between nearest neighbors in one layer. $\gamma_1 \sim 0.38\text{eV}$ relates atoms A_2 and B_1. $\gamma_3 \sim 0.38\text{eV}$ connects sites B_2 and A_1 whereas $\gamma_4 \sim 0.14\text{eV}$ relates sites A_2 and A_1 [92, 93]. Quantities $\epsilon_{A,B/1,2}$ are the on-site energies, each for one of the 4 sites per unit cell considered, which are not necessarily equal. What is physically relevant is not so much their values but their differences. We define the quantities U, Δ',δ_{AB}, as [94]

$$U = \frac{1}{2}\left[(\epsilon_{A1} + \epsilon_{B1}) - (\epsilon_{A2} + \epsilon_{B2})\right] \tag{7.2a}$$

$$\Delta' = \frac{1}{2}\left[(\epsilon_{A2} + \epsilon_{B1}) - (\epsilon_{A1} + \epsilon_{B2})\right] \tag{7.2b}$$

$$\delta_{AB} = \frac{1}{2}\left[(\epsilon_{A1} + \epsilon_{A2}) - (\epsilon_{B1} + \epsilon_{B2})\right] \tag{7.2c}$$

where U describes the asymmetry between to the two layers, Δ' accounts for the difference in energy between the dimer and non-dimer atoms, and finally δ_{AB} accounts for the difference in sites A and B in each layer [92]. In the simplest case, we can consider $v_4 = 0$ and the on-site energies only causing asymmetry in layers $\epsilon_{A1} = \epsilon_{B1} = -U/2$ and $\epsilon_{A2} = \epsilon_{B2} = U/2$. Then the Hamiltonian can be exactly solved. The eigenenergies are

$$\begin{aligned} E_{h,e} = &\pm \left[\frac{\gamma_1^2}{2} + \frac{U^2}{4} + \left(v^2 + \frac{v_3^2}{2}\right)p^2 + (-1)^\alpha\sqrt{\Gamma}\right]^{1/2}, \\ &\text{with} \\ \Gamma = &\frac{1}{4}(\gamma_1^2 - v_3^2p^2)^2 + v^2p^2[\gamma_1^2 + U^2 + v_3^2p^2] \\ &+ 2\xi\gamma_1v_3v^2p^3\cos(3\varphi), \end{aligned} \tag{7.3}$$

where $\xi = \pm 1$ accounts for the valley and φ is the polar angle of the momentum $\vec{p} = p\cos\varphi\vec{u}_x + p\sin\varphi\vec{u}_y$. α distinguishes the bands of lower energy of non-dimer sites ($\alpha = 1$) from those of higher energy of dimer sites ($\alpha = 2$).

From equation 7.3 we see that there is symmetry between the bands of holes and electrons (notice the $\pm$ that refers to holes and electrons respectively). At very low energy, in the range of 2eV, γ_3 has a remarkable effect on the band structure. As we can see in figure 7.1, γ_3 is the hopping parameter that relates non-dimmer sites. This skewed interaction has trigonal symmetry and makes the band structure

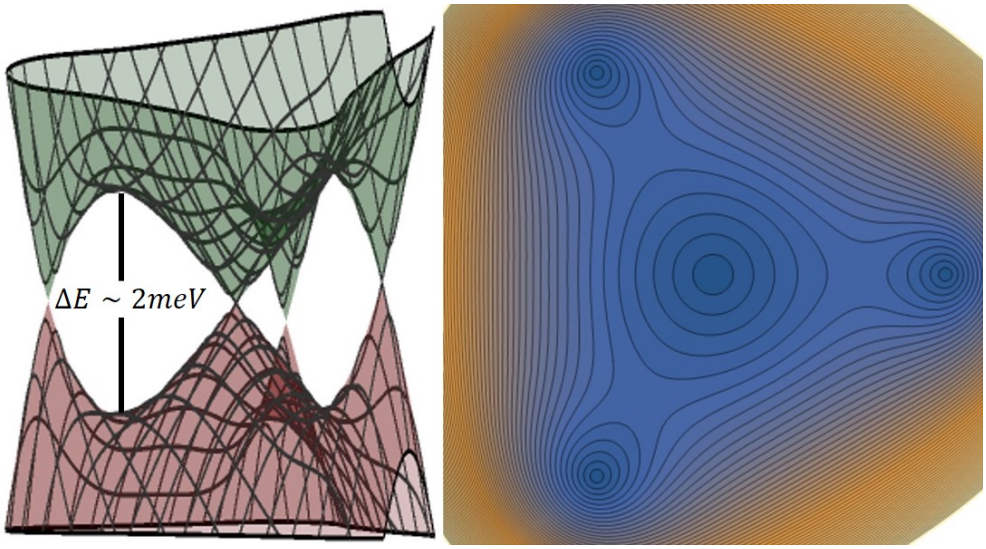

Figure 7.2: Schematichs of the bands of bilayer graphene at low energy, with $\gamma_3 \neq 0$.

follow this symmetry at low energy, where the last term of equation 7.3 is more important. This behavior is known as trigonal warping. As it is shown in figure 7.3, the contact between the two lowest electron and hole bands, at the K points are made at 4 Dirac points. The 3 exterior Dirac points have a Berry phase of π whereas the central one has a Berry phase of $-\pi$, giving the total of 2π that has been already studied as the responsible of the absence of the 0^{th} step in the Hall conductivity, which is a Direct consequence of bilayer's $n = 0$ Landau level. From an experimental point of view, it would be interesting to explore the orbital magnetization of a bilayer graphene in the energy range of these trigonal warping effect, because we can think that the diamagnetic signal coming from these 4 Dirac points will add up, giving a signal 4 times bigger than the one in monolayer graphene. Additionally, as figure 7.3b suggest, 3 saddle points can appear while going from one Dirac point to the next one. This, as mentioned before, would be accompanied with van Hove singularities and orbital paramagnetism. In order to be able to observe such peaks, we should have an energy resolution in the order of $1\mathrm{meV}$ and a sample whose disorder energy scale is smaller than that. As shown in figure 7.3, the difference in energy between the 4-Dirac points and the saddle point is around $1\mathrm{meV}$. If the energy scale of disorder is of similar value, then the signal coming from the Dirac points and vHs will be rounded, overlapping and hiding the smallest contributions.

However, it is worth mentioning that this phenomenon is important only at very low energies. For slightly higher energies, the term on $\sim \sqrt{v^2p^2}$ dominates and then, bilayer graphene follows a quadratic dispertion relation $E \sim p^2$. Furthermore, by neglecting the hopping interaction γ_3 for an instant, bilayer graphene's

orbital diamagnetism is still quite interesting. Because it is composed by two layers of graphene, BLG inherits the strongly diamagnetic behavior at the charge neutrality point. In particular, the orbital susceptibility of bilayer graphene was calculated in the 80s in the context of the understanding of the magnetism of graphite intercalated compounds [95, 96]. In the limit when $\gamma_3 \to 0$ it takes the form [60]:

$$\chi = g_v g_s \frac{e^2 v^2}{4\pi c^2 \gamma_1} \theta(\gamma_1 - |\epsilon|) \left(\log \frac{|\epsilon|}{\gamma_1} + \frac{1}{3} \right). \tag{7.4}$$

The out of plane interaction in BLG characterized by the hopping parameter γ_1 modifies the $\delta(\mu)$ divergence of monolayer graphene and the susceptibility exhibits a logarithmic divergence. It was also shown [95, 96] that when the only term considered is nearest-neighbors interaction, or in this case $\gamma_1 \to 0$, the susceptibility reduces to the one of monolayer, as it is expected from what would be 2 decoupled monolayers.

Another remarkable property of BLG is the possibility of opening a band gap by applying an electric displacement field. From equation 7.2a, the parameter U reflects the difference in energy between the layers. If $U \neq 0$, this means that the inversion symmetry is broken and a gap is open. By the means of a displacement field, the inversion symmetry is broken. It was first experimentally observed in [97]. In this experiment the BLG was inserted between two gates, top and bottom, allowing independently the 2-layer doping control. Figure 7.4 shows the schematic set up of a BLG in between two gates. Generally, by placing BLG in a region of electric field perpendicular to the plane, there is a spatial asymmetry in the perpendicular direction, due to an imbalance of the charge induced on each layer. This is caused by the finite thickness of BLG [98, 92]. This effect is enhanced by adding a second gate [99, 97], so BLG is in a region of two added electric fields, which work as 2 capacitors in series. The asymmetry is related to the average electric displacement field, and the gap is proportional to this average [97]. This gap has been shown to depend on the induced difference of tension $|V_1 - V_2|$ between the two layers of BLG. By the means of two electrostatic gates, it is possible to control this voltage and simultaneously control the total excess charge on BLG.

$$\begin{aligned} U \sim \overline{D} &= \frac{1}{2}(D_t + D_b) = \frac{\epsilon}{2}\left(\frac{V_b}{d_b} + \frac{V_t}{d_t}\right) \\ n = Q_{tot}/eS &= C_1 V_1/eS + C_2 V_2/eS = \frac{\varepsilon_0}{e}\left(\frac{\varepsilon_{r2} V_t}{d_1} + \frac{\varepsilon_{r2} V_t d_2}{d_2}\right) \end{aligned} \tag{7.5}$$

This has been achieved experimentally [97] and has been compared with theoretical models as it can be seen in figure 7.5. The relation between the displacement field and the gap generated is shown in figure 7.5 from [97].

When thinking in terms of the orbital susceptibility, the possibility of a controlled gap opening seems very interesting. Recovering the $\gamma_3 \neq 0$ and a non-zero

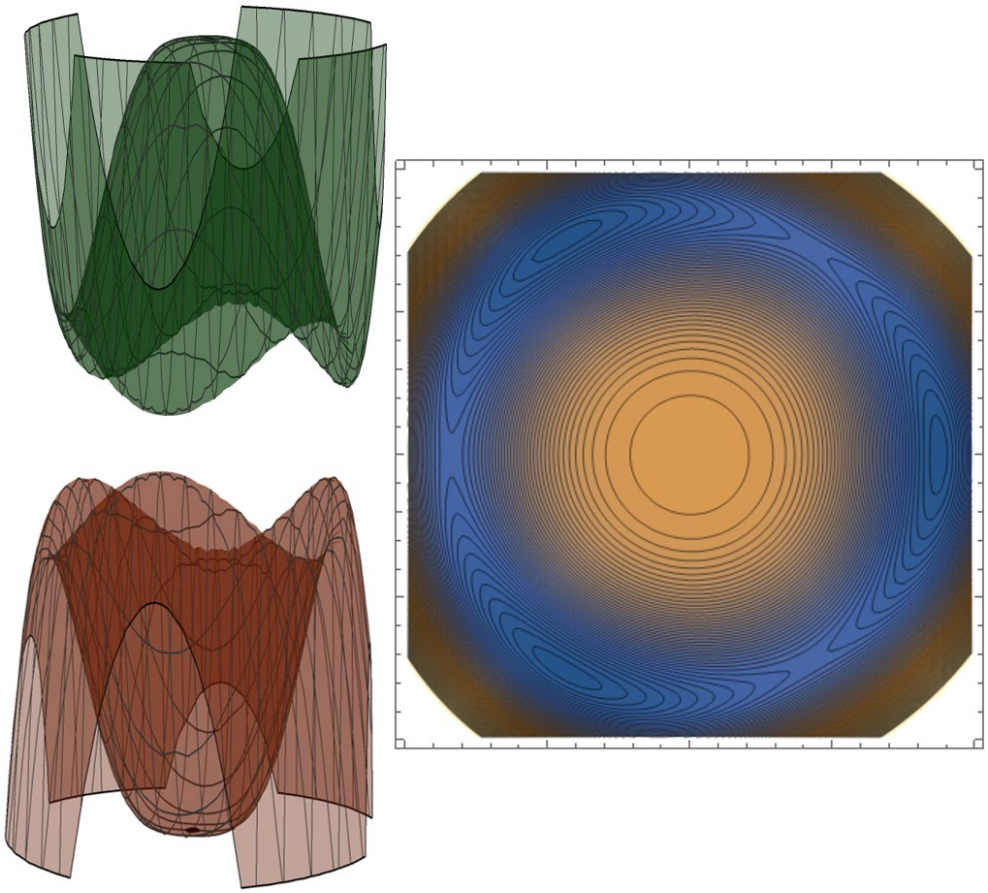

Figure 7.3: Schematics of the bands with $U = \gamma_1$ and $\gamma_3 \neq 0$.

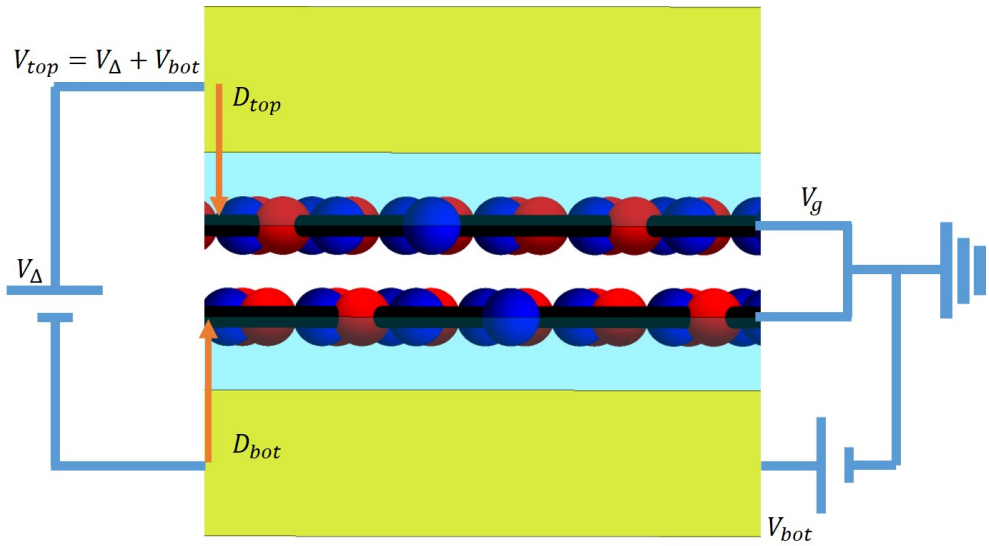

Figure 7.4: Schematics of the connection of bilayer graphene with two gates.

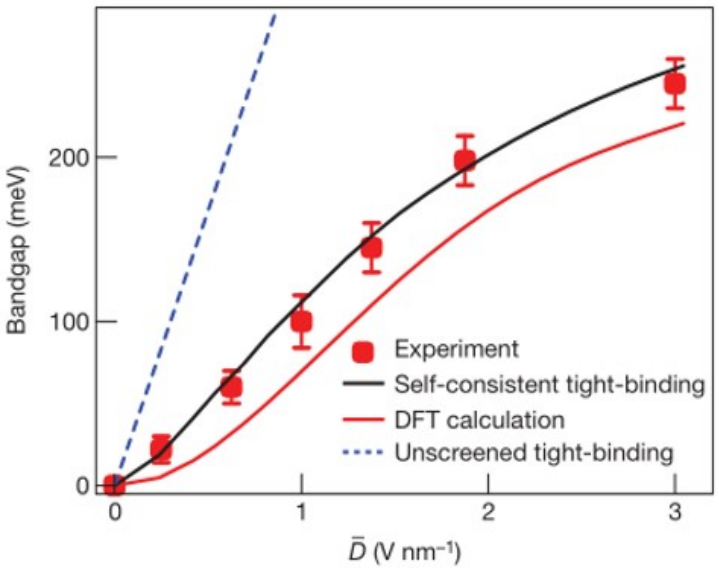

Figure 7.5: Relation between the average electric displacement field applied to a bilayer graphene sample and the energy of the open gap. Adapted from [97].

gap $U \neq 0$, the band structure for the lowest bands in BLG shows a Mexican hat shape. However, because of the trigonal warping, the saddle points are preserved. Koshino [100] calculated the behavior of susceptibility for different gap values. Inside the gap, the magnetic response continues to be diamagnetic but instead of a peak, the susceptibility is constant, forming a diamagnetic plateau. When the chemical potential reaches the saddle points, where the density of states diverges, then the orbital susceptibility diverges with a positive sign, and exhibits a paramagnetic peak. The explanation is the same as the one given in 6. As mentioned there, electron trajectories are hyperbolas close to the saddle points. When these diamagnetic trajectories are close enough, tunneling can appear between trajectories, giving a resulting closed orbit whose sign is paramagnetic. As it was calculated by Koshino [100], by increasing the bandgap, the diamagnetic pic becomes a plateau that gets smaller and wider by increasing the gap, and the paramagnetic contributions increase. [60].

The band structure, density of states and the orbital magnetic susceptibility is shown in figure 7.6 where 3 values of the gap energy have been considered: 0, $0.2\gamma_1$ and $0.5\gamma_1$. According to [92], this means energies of the order of 0, $60\mathrm{meV}$ and $150\mathrm{meV}$ respectively. From the results given in [97], this corresponds to values of the average displacement field of approximately 0, 70 and $150\ \mathrm{V\,nm^{-1}}$, respectively.

7.2 . Preliminary results on susceptibility of a bilayer graphene

In this section we present preliminary results on the evolution of the orbital magnetism as a function of the induced gap. The objective is to follow the behavior of the McClure diamagnetic peak, with increasing electrical displacement field, and if possible, the appearance of paramagnetic peaks at the edge of the gap region.

Our sample consisted of an encapsulated Bernal-stack bilayer graphene. The size of the gated zone in this sample is $15\mu\mathrm{m}$ by $4\mu\mathrm{m}$ approximately, similar to the monolayers discussed in chapter 5. No intentional alignment with the BN crystals was done to be able to neglect the effects of moiré superlattices. As it was described in chapter 4, it was fabricated using the traditional dry transfer techniques. This sample was then dropped on top of the GMRs chip, where previously a gold electrode was deposited to be used as the electrode of the bottom gate. It was designed using electron beam lithography, and the purpose was to fill the space between GMRs and get a flatter region. This electrode was measured in the AFM and it was found to correct the step of about $60\mathrm{nm}$ that exists between the GMRs. Once the sample was in place, a gold top gate was deposited in a way that it covers the same region of the sample over the bottom gate. Also, 1D contacts where patterned in order to have access to transport measurements in parallel with the magnetization. To avoid having a current in parallel with the gaped bilayer zone, the gate electrode was used as a mask to delimit the zone of bilayer to keep and then, the rest of it was etched away using standard RIE techniques. This was done because we wanted to reduce as much as possible the contribution from BLG to transport or magnetism that is not affected by the two gates. In particular, if part of BLG is not affected by the two gates, then this part will not be gaped and current will still flow through it, giving always a signal regardless the electric field. Unfortunately, the contact of one of the electrodes was lost when etching away the bilayer graphene that was not in between the gates.

Figure 7.7 shows the 2-probe resistance as a function of top and bottom gate voltages. The linear yellow zone that crosses diagonally the plot indicates the charge neutrality point. It evolves linearly following the electric displacement field as it is expected. It allows us to find the values of gate voltage where to look for the signatures of the orbital magnetism of BLG. Figure 7.8 shows the same information but for larger values of the two gates outside the zone in 7.7. Figure 7.8a shows the resistance for the longitudinal direction, whereas 7.8b shows the transverse direction. 7.8a seems to indicate that for electric fields bigger than $0.39\mathrm{V\,nm^{-1}}$, the value of the resistance reaches a plateau and does not increase more with increasing electric field. This may be the indication of the existence of a conducting channel in parallel that cannot be gaped with the electric field. Evidence of this kind of behavior has been presented in [101] paper. There, this channel appears as the boundary between AB and BA regions in the same bilayer crystal. The coexistence of these two stacking types in Bernal-stack BLG should not be shocking, because the two types are energetically equivalent and its presence

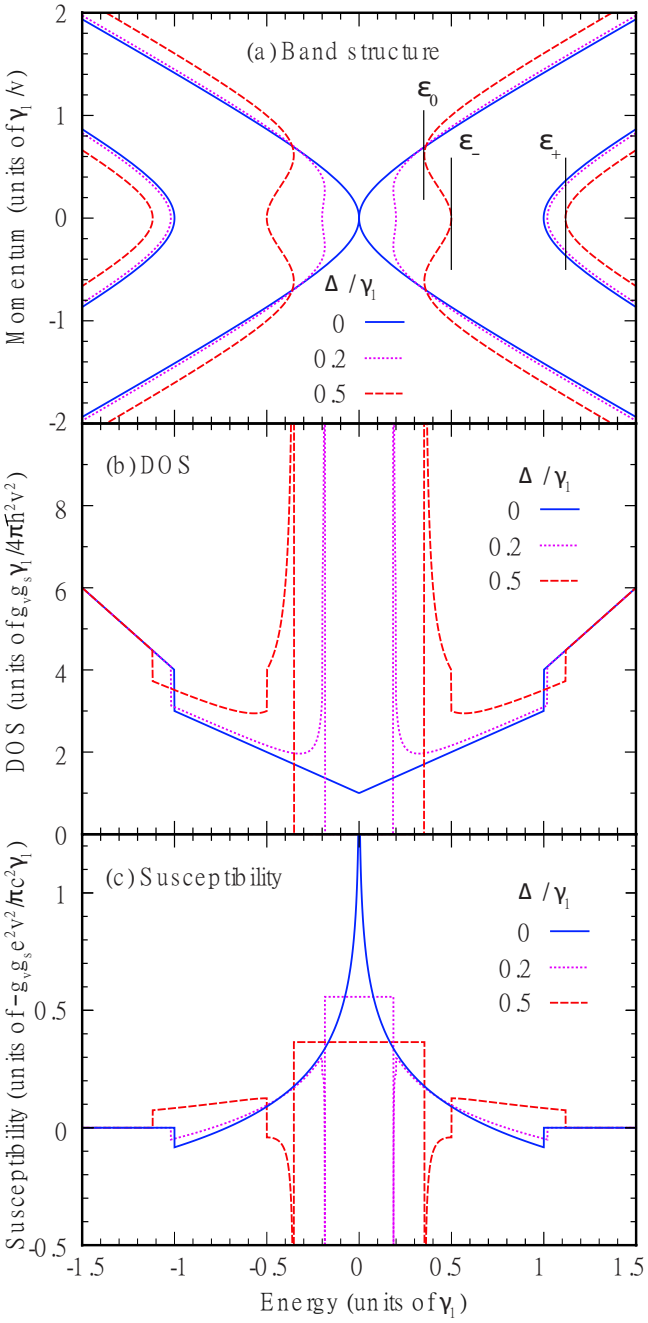

Figure 7.6: Top: Band structure for bilayer graphene showing the lowest 4 bands and their evolution when the interlayer energy difference is 0, $0.2\gamma_1$ and $0.5\gamma_1$. The calculations give a gap that is approximately equal to the interlayer energy difference. Middle: Density of states calculated from the band structure. The DOS diverges at the points where the band structure shows saddle points. Bottom: corresponding orbital susceptibility for the same cases as previous. Adapted from [100].

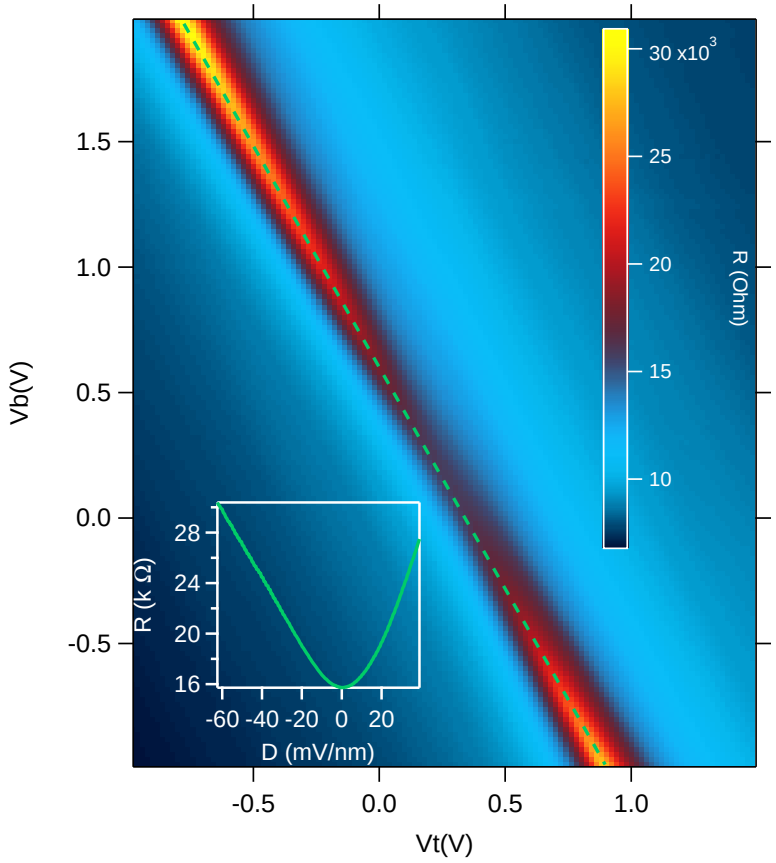

Figure 7.7: Resistance as a function of both top gate voltage and bottom gate voltage. The yellow zone with a green dashed line indicates the zone of charge neutrality point. Transverse to this line lies the points where the gap is constant. The inset shows the evolution of the resistance at CNP, as a function of the perpendicular electric field.

could be explained perhaps by strain on the sample during the fabrication process. In between an AB and a BA zones, the stacking must pass through AA stacking. This must be the responsible of the remaining conduction as it has been shown that AA region do not open a gap with electric field [102]. Figure 7.9 shows the resistance and its derivative as a function of the gate voltage for BLG in a perpendicular magnetic field of $1\mathrm{T}$. The oscillations of the resistance that appear at slightly higher doping are the Shubnikov-de Haas oscillations. As it is shown in figure 7.9A and 7.9B, they appear clearer in the derivative and are barely visible in the direct 2-probes measurement or in the integral.

Figure 7.10 show the evolution of the McClure peak for a bilayer graphene as a function of the electric displacement field applied using the two gates. All the curves in this plot were obtained at constant magnetic field of $0.2\mathrm{T}$. As it can

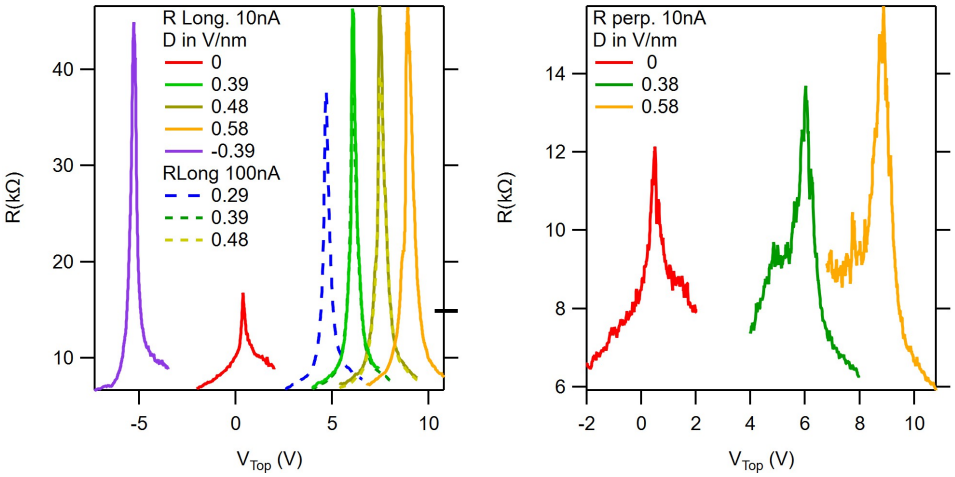

Figure 7.8: 2-probe resistance as a function of the top gate voltage, for different values of the bottom gate voltage. The two plots show two directions of the measurements: longitudinal (left) and transversal (right).

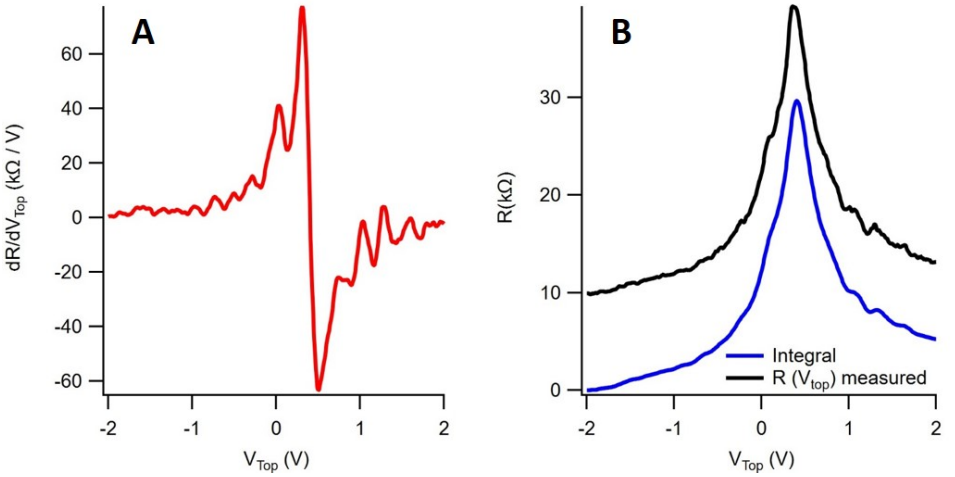

Figure 7.9: (A) Derivative of the resistance as a function of the top gate voltage for bilayer graphene. Shubnikov-de Haas oscillations are visible from $B = 1$T. (B) 2-probe measurement of the resistance as a function of gate voltage in black. The blue curve is the integral of the left red curve.

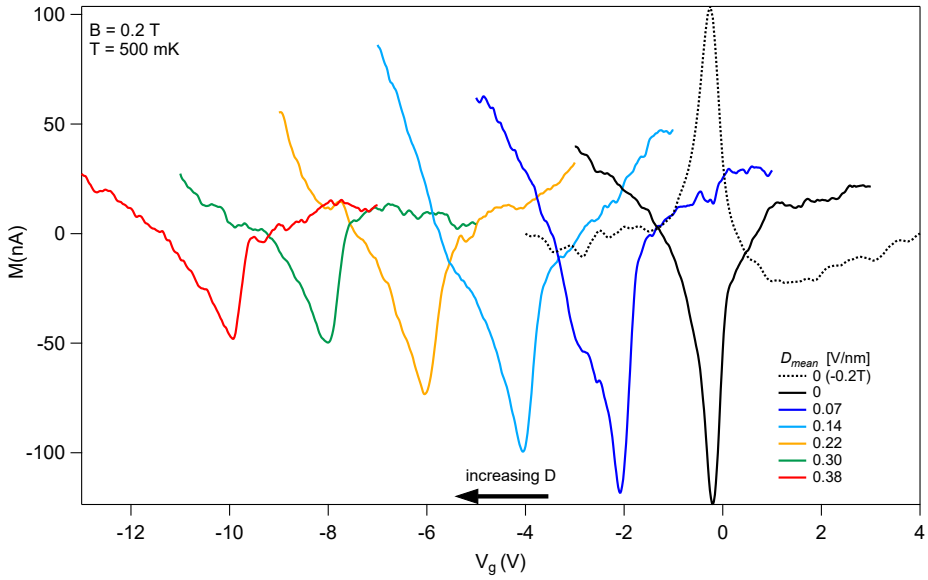

Figure 7.10: McClure peak for bilayer graphene for different values of the displacement field. Temperature in these measurements is in the order of 500mK.

be seen from the plot, when the electric field is zero, the McClure peak is the sharpest and highest. This can be interpreted as the whole crystal contributing to the orbital magnetization, without the effects of the induced gap. As the electric field increases, we see a broadening of the peak and a diminution of its amplitude. We can interpret this as the starting of a gap opening in the zones of BLG compatible with this AB and BA. However, the diamagnetic behavior, even if small and broad, persist even at average displacement fields of around $\overline{D} \sim 0.5\mathrm{V\,nm^{-1}}$. The expected signal for a gaped bilayer graphene is a rectangular shape, where the diamangetic part reaches a plateau as wide as the gap, and that is delimited by the paramagnetic peaks coming from the van Hove singularities. This behavior was not observed in this sample. What is seen instead is the mentioned persistent diamagnetic peak. One possible explanation of this behavior (similar to the saturation of the resistance described above) could also be related to the formation of boundary states between AB and BA regions. As a matter of fact, if the presence of the gap is not uniform in the sample, there will always be regions with negative susceptibility cancelling smaller positive contributions. Therefore the paramagnetism of the van Hove singularities cannot be seen. Another possibility may be related to disorder. In the case of high disorder, the electric field necessary to see the effects of the gap might be even larger than the range that was used here. More studies are required in order to answer the question whether bilayer graphene is a good system to search for orbital paramagnetism, and whether trigonal warping effects are distinguishable using this measurements technique or even, if other

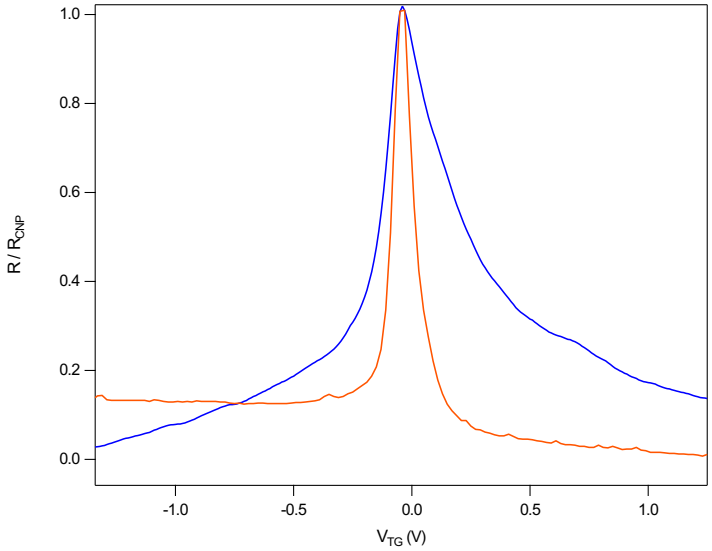

Figure 7.11: Normalized 2-probe resistance of the BLG sample (blue) in comparison with the moiré sample M_A (in orange).

phenomena as VHE can be investigated using this platform.

Finally, we show (as an illustrative figure) a comparison between the McClure peaks that we were able to measure for monolayer and bilayer graphene. In the case of samples M_A and B_1, the size of the sample and the geometry and sensibility of the GMRs is similar. However, a large difference in the width of the peaks can be observed. This put on evidence the nature of their respective singular behavior, being the monolayer the sharpest and tallest because the divergence is ideally a Dirac delta and the bilayer being a logarithmic function.

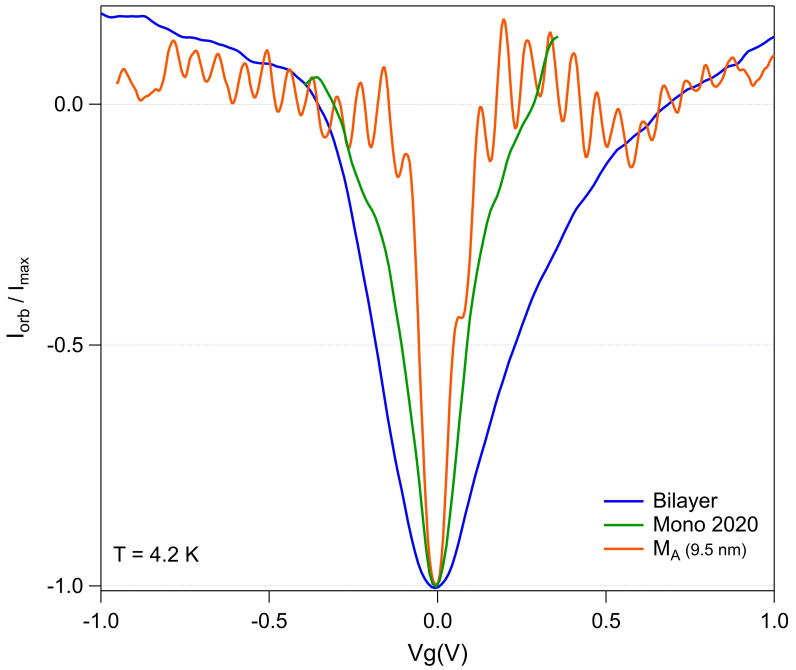

Figure 7.12: Orbital magnetism of three of the samples studied in this thesis, at charge neutrality point, in an external magnetic field of $0.2\mathrm{T}$. The magnetization has been normalized to compare the width of these peaks. The bilayer, in blue, shows the widest peak (FWHM $\sim 0.4\mathrm{V}$). Whereas between the two monolayers, one can directly measure a factor 2 of the widths (~ 0.2 vs $\sim 0.1\mathrm{V}$), which is in agreement with the parameters of the model of disorder discussed in chapter 5.

8 - Conclusions

In this thesis, we have studied the orbital magnetism of three related but different systems based on graphene. First, an encapsulated monolayer graphene. Then, two samples of encapsulated monolayer graphene with a moiré potential where the moiré pattern comes from the alignment between graphene and the boron nitride substrate. Finally, a sample consisting of encapsulated AB bilayer graphene. Through the means of a combination of highly sensitive giant magneto-resistant (GMR) probes with the chemical potential control through the gate voltage modulation, we have opened a new way to measure the orbital magnetization in 2D materials.

In the case of the first monolayer graphene, we have detected the McClure singularity of low-field orbital magnetization of a single graphene monolayer at the Dirac point, which is the signature of the π Berry phase of electronic wave functions in graphene. We studied the evolution of this singular peak as a function of magnetic field. We were able to observe the crossover between the McClure diamagnetism at CNP and the de Haas - van Alphen oscillations at higher doping, when the magnetic field is strong enough. We also study the role of disorder in the rounding this singularity and showed the experimental results of a second sample in which this disorder is reduced. We presented a model that allows us to reproduce our data in a quantitative way, taking into account this disorder. The results of this part of the work were published in the reference [17].

In the case of the the orbital magnetization of graphene in a moiré potential, our measurements have shown evidence of a rich set of magnetic singularities of the orbital magnetization in the vicinity of SDP. These consist of diamagnetic peaks at the satellite Dirac points surrounded by paramagnetic peaks which can be associated to the van-Hove singularities of the DOS at the saddle points of the mini-band structure induced by the moiré potential. These experiments therefore confirm the long standing theoretical predictions on the existence of paramagnetic orbital magnetism in 2D materials at Van Hove singularities which in the case of the graphene/hBN moiré investigated here, exceeds by far the Pauli susceptibility. These results form part of an article in preparation.

In the last system studied, we focused on the orbital magnetism of bilayer graphene. We have obtained results concerning the diamagnetic divergence of this system, which is predicted to be a logarithmic divergence. We have also explored the evolution of this diamagnetic peak as a function of the perpendicular electric field that was applied between a top and bottom gates. This perpendicular electric field has been shown to open a gap in BLG, and the theoretical prediction states that the diamagnetic response tends to decrease for higher electric field. Then, the appearance of paramagnetic peaks at the border of the gap is expected.

The preliminary experimental results showed a decrease and broadening in the

diamagnetic peak as the electric field increased. However, no sign of the paramagnetic peaks has been found yet. This might be related to the presence of conducting channels that are present and prevent the gap for forming. More experiments exploring the magnetism in bilayer graphene are necessary in order to obtain conclusive results about the evolution of the magnetism with electric field.

We believe that our results prove the suitability of our method to explore a large variety of systems. For example, the possibility to study valley currents in BLG raises also great interest as a future project. Specially since our set up allows for the measurements of equilibrium orbital currents and non-local transport in the same sample. This kind of experiments should also enable the investigation of interband-induced Berry curvature anomalies [23, 20] as well as Coulomb interaction effects in 2D materials such as graphene and its bilayer [103, 77].

Another notable example is twisted bilayer graphene at the magic angle, which is known to have flat bands [83] and host thrilling properties due to interactions. An anomalous quantum Hall effect is then expected to appear as the result of Coulomb interactions leading to valley symmetry breaking [104, 105, 106] and formation of orbital current loops in zero magnetic field. They are detectable via the orbital magnetic moments they would generate as recently shown in [15]. The possibility to generate flat bands with a periodic array of strain has been also predicted [107, 108, 109].

It is also interesting that the typical amplitude of the paramagnetic susceptibility peaks we have measured is of the same order of magnitude than the values predicted for graphene bilayer moirés close to the magic angle [110]. This singular paramagnetic orbital magnetism is shown to possibly lead to the emergence of new kinds of correlated phases when the sample is imbedded in a plasmonic cavity. Our results also motivate the extension of this work to graphene twisted bilayers with larger moiré periods in which field periodic orbital currents are expected [111].

Moreover, in the supplementary materials of [17], data on a strained sample was presented. On this sample it was possible to detect a gate dependent GMR signal at zero magnetic field. This preliminary result suggest that more controlled situations like in [112] can be combined with our set up and investigated.

Finally, we expect that the kind of measurements we have performed could also be used to reveal the expected ballistic loop currents along edges of 2D topological insulators [9, 113, 114, 115].

Bibliography

[1] Dongwook Go et al. “Orbitronics: Orbital currents in solids”. In: *EPL (Europhysics Letters)* 135.3 (Aug. 1, 2021), p. 37001. doi: 10.1209/0295-5075/ac2653.

[2] Võ Tin Phong et al. “Optically Controlled Orbitronics on a Triangular Lattice”. In: *Physical Review Letters* 123.23 (Dec. 6, 2019), p. 236403. doi: 10.1103/PhysRevLett.123.236403.

[3] Dongwook Go et al. “Toward surface orbitronics: giant orbital magnetism from the orbital Rashba effect at the surface of sp-metals”. In: *Scientific Reports* 7.1 (Sept. 25, 2017), p. 46742. doi: 10.1038/srep46742.

[4] B. Andrei Bernevig, Taylor L. Hughes, and Shou-Cheng Zhang. “Orbitronics: The Intrinsic Orbital Current in p -Doped Silicon”. In: *Physical Review Letters* 95.6 (Aug. 1, 2005), p. 066601. doi: 10.1103/PhysRevLett.95.066601.

[5] Sayantika Bhowal and Giovanni Vignale. “Orbital Hall effect as an alternative to valley Hall effect in gapped graphene”. In: *Physical Review B* 103.19 (May 12, 2021), p. 195309. doi: 10.1103/PhysRevB.103.195309.

[6] Luis M. Canonico et al. “Orbital Hall insulating phase in transition metal dichalcogenide monolayers”. In: *Physical Review B* 101.16 (Apr. 29, 2020), p. 161409. doi: 10.1103/PhysRevB.101.161409.

[7] Luis M. Canonico et al. “Two-dimensional orbital Hall insulators”. In: *Physical Review B* 101.7 (Feb. 26, 2020), p. 075429. doi: 10.1103/PhysRevB.101.075429.

[8] Leandro Salemi et al. “Orbitally dominated Rashba-Edelstein effect in noncentrosymmetric antiferromagnets”. In: *Nature Communications* 10.1 (Dec. 2019), p. 5381. doi: 10.1038/s41467-019-13367-z.

[9] Taiki Yoda, Takehito Yokoyama, and Shuichi Murakami. “Orbital Edelstein Effect as a Condensed-Matter Analog of Solenoids”. In: *Nano Letters* 18.2 (Feb. 14, 2018), pp. 916–920. doi: 10.1021/acs.nanolett.7b04300.

[10] Annika Johansson et al. “Spin and orbital Edelstein effects in a two-dimensional electron gas: Theory and application to SrTiO 3 interfaces”. In: *Physical Review Research* 3.1 (Mar. 24, 2021), p. 013275. doi: 10.1103/PhysRevResearch.3.013275.

[11] LD Landau. “Diamagnetismus der metalle”. In: *Zeitschrift für Physik* 64.9 (1930). Publisher: Springer, pp. 629–637.

[12] J. W. McClure. “Diamagnetism of Graphite”. In: *Physical Review* 104.3 (Nov. 1, 1956), pp. 666–671. doi: 10.1103/PhysRev.104.666.

[13] L. P. Lévy et al. “Magnetization of mesoscopic copper rings: Evidence for persistent currents”. In: *Physical Review Letters* 64.17 (Apr. 23, 1990), pp. 2074–2077. doi: 10.1103/PhysRevLett.64.2074.

[14] Philippe Bourges, Dalila Bounoua, and Yvan Sidis. “Loop currents in quantum matter”. In: *Comptes Rendus. Physique* 22 (S5 May 11, 2022), pp. 7–31. doi: 10.5802/crphys.84.

[15] C. L. Tschirhart et al. “Imaging orbital ferromagnetism in a moiré Chern insulator”. In: *Science* 372.6548 (June 18, 2021), pp. 1323–1327. doi: 10.1126/science.abd3190.

[16] Chun-Chih Tseng et al. “Anomalous Hall effect at half filling in twisted bilayer graphene”. In: *Nature Physics* 18.9 (Sept. 2022), pp. 1038–1042. doi: 10.1038/s41567-022-01697-7.

[17] J. Vallejo Bustamante et al. “Detection of graphene’s divergent orbital diamagnetism at the Dirac point”. In: *Science* 374.6573 (Dec. 10, 2021), pp. 1399–1402. doi: 10.1126/science.abf9396.

[18] G. Vignale. “Orbital paramagnetism of electrons in a two - dimensional lattice”. In: *Physical Review Letters* 67.3 (July 15, 1991), pp. 358–361. doi: 10.1103/PhysRevLett.67.358.

[19] A. Raoux et al. “From Dia- to Paramagnetic Orbital Susceptibility of Massless Fermions”. In: *Physical Review Letters* 112.2 (Jan. 14, 2014), p. 026402. doi: 10.1103/PhysRevLett.112.026402.

[20] Arnaud Raoux et al. “Orbital magnetism in coupled-bands models”. In: *Physical Review B* 91.8 (Feb. 23, 2015), p. 085120. doi: 10.1103/PhysRevB.91.085120.

[21] Arnaud Raoux. “Magnétisme orbital et aspects géométriques de la théorie des bandes”. PhD thesis. Université Paris - Sud, 2017.

[22] Di Xiao, Junren Shi, and Qian Niu. “Berry Phase Correction to Electron Density of States in Solids”. In: *Physical Review Letters* 95.13 (Sept. 22, 2005), p. 137204. doi: 10.1103/PhysRevLett.95.137204.

[23] Di Xiao, Ming-Che Chang, and Qian Niu. “Berry phase effects on electronic properties”. In: *Reviews of Modern Physics* 82.3 (July 6, 2010), pp. 1959–2007. doi: 10.1103/RevModPhys.82.1959.

[24] Di Xiao et al. “Coupled Spin and Valley Physics in Monolayers of MoS 2 and Other Group-VI Dichalcogenides”. In: *Physical Review Letters* 108.19 (May 7, 2012), p. 196802. doi: 10.1103/PhysRevLett.108.196802.

[25] L. P. Lévy. *Magnétisme et Supraconductivité*. Paris: EDP Sciences, 1997.

[26] Hidetoshi Fukuyama and Ryogo Kubo. “Interband effect on magnetic susceptibility. I. A simple two-band model”. In: *Journal of the Physical Society of Japan* 27.3 (1969). Publisher: The Physical Society of Japan, pp. 604–614.

[27] Hidetoshi Fukuyama and Ryogo Kubo. “Interband Effects on Magnetic Susceptibility. II. Diamagnetism of Bismuth”. In: *Journal of the Physical Society of Japan* 28.3 (1970), pp. 570–581. doi: 10.1143/JPSJ.28.570.

[28] Hidetoshi Fukuyama. “Theory of orbital magnetism of Bloch electrons: Coulomb interactions”. In: *Progress of Theoretical Physics* 45.3 (1971). Publisher: Oxford University Press, pp. 704–729.

[29] I. I. Rabi. “Das freie Elektron im homogenen Magnetfeld nach der Diracschen Theorie”. In: *Zeitschrift fr Physik* 49.7 (July 1928), pp. 507–511. doi: 10.1007/BF01333634.

[30] Neil W. Ashcroft and N. David Mermin. *Solid state physics*. New York: Holt, Rinehart and Winston, 1976. 826 pp.

[31] Morrel H. Cohen and L. M. Falicov. “Magnetic Breakdown in Crystals”. In: *Physical Review Letters* 7.6 (Sept. 15, 1961), pp. 231–233. doi: 10.1103/PhysRevLett.7.231.

[32] L.D. Landau, E.M. Lifshitz, and L.P. Pitaevskii. *Course of Theoretical Physics: Statistical Physics, Part 2 : by E.M. Lifshitz and L.P. Pitaevskii*. vol. 9. 1980.

[33] M. O. Goerbig. “Electronic properties of graphene in a strong magnetic field”. In: *Reviews of Modern Physics* 83.4 (Nov. 3, 2011), pp. 1193–1243. doi: 10.1103/RevModPhys.83.1193.

[34] P. R. Wallace. “The Band Theory of Graphite”. In: *Physical Review* 71.9 (May 1, 1947), pp. 622–634. doi: 10.1103/PhysRev.71.622.

[35] A. H. Castro Neto et al. “The electronic properties of graphene”. In: *Reviews of Modern Physics* 81.1 (Jan. 14, 2009). Publisher: American Physical Society, pp. 109–162. doi: 10.1103/RevModPhys.81.109.

[36] Arnaud Raoux et al. “Orbital magnetism in coupled-bands models”. In: *Physical Review B* 91.8 (Feb. 23, 2015), p. 085120. doi: 10.1103/PhysRevB.91.085120.

[37] Dean Moldovan, Miša Anđelković, and Francois Peeters. *pybinding*. Version v0.9.5. 2020.

[38] Zala Lenarvcivc. “Landau levels in graphene”. Seminar.

[39] L. Onsager. “Interpretation of the de Haas-van Alphen effect”. In: *The London, Edinburgh, and Dublin Philosophical Magazine and Journal of Science* 43.344 (1952), pp. 1006–1008. doi: 10.1080/14786440908521019.

[40] J. N. Fuchs et al. “Topological Berry phase and semiclassical quantization of cyclotron orbits for two dimensional electrons in coupled band models”. In: *The European Physical Journal B* 77.3 (Oct. 2010), pp. 351–362. doi: 10.1140/epjb/e2010-00259-2.

[41] Walter Kohn. “Theory of Bloch Electrons in a Magnetic Field: The Effective Hamiltonian”. In: *Physical Review* 115.6 (Sept. 15, 1959), pp. 1460–1478. doi: 10.1103/PhysRev.115.1460.

[42] Laura M. Roth. “Semiclassical Theory of Magnetic Energy Levels and Magnetic Susceptibility of Bloch Electrons”. In: *Physical Review* 145.2 (May 13, 1966), pp. 434–448. doi: 10.1103/PhysRev.145.434.

[43] Claude Fermon and Marcel Van de Voorde. *Nanomagnetism: Applications and Perspectives*. Google-Books-ID: Xa7ODQAAQBAJ. John Wiley & Sons, Dec. 28, 2016. 350 pp.

[44] Jack Bass and William P Pratt. “Spin-diffusion lengths in metals and alloys, and spin-flipping at metal/metal interfaces: an experimentalist’s critical review”. In: *Journal of Physics: Condensed Matter* 19.18 (May 8, 2007), p. 183201. doi: 10.1088/0953-8984/19/18/183201.

[45] M. N. Baibich et al. “Giant Magnetoresistance of (001)Fe/(001)Cr Magnetic Superlattices”. In: *Physical Review Letters* 61.21 (Nov. 21, 1988), pp. 2472–2475. doi: 10.1103/PhysRevLett.61.2472.

[46] G. Binasch et al. “Enhanced magnetoresistance in layered magnetic structures with antiferromagnetic interlayer exchange”. In: *Physical Review B* 39.7 (Mar. 1, 1989), pp. 4828–4830. doi: 10.1103/PhysRevB.39.4828.

[47] *Smart Sensors, Measurement and Instrumentation*. Springer. url: https://www.springer.com/series/10617.

[48] R. E. Camley and J. Barnaś. “Theory of giant magnetoresistance effects in magnetic layered structures with antiferromagnetic coupling”. In: *Physical Review Letters* 63.6 (Aug. 7, 1989), pp. 664–667. doi: 10.1103/PhysRevLett.63.664.

[49] E. H. Sondheimer. “The mean free path of electrons in metals”. In: *Advances in Physics* 50.6 (2001). Publisher: Taylor & Francis _eprint: https://doi.org/10.1080/00018730110102187, pp. 499–537. doi: 10.1080/00018730110102187.

[50] J. Barnaś et al. “Novel magnetoresistance effect in layered magnetic structures: Theory and experiment”. In: *Physical Review B* 42.13 (Nov. 1, 1990), pp. 8110–8120. doi: 10.1103/PhysRevB.42.8110.

[51] P. A. Guitard et al. “Local nuclear magnetic resonance spectroscopy with giant magnetic resistance-based sensors”. In: *Applied Physics Letters* 108.21 (May 23, 2016), p. 212405. doi: 10.1063/1.4952947.

[52] Denis Vasyukov et al. “A scanning superconducting quantum interference device with single electron spin sensitivity”. In: *Nature Nanotechnology* 8.9 (Sept. 2013), pp. 639–644. doi: 10.1038/nnano.2013.169.

[53] Y. Anahory et al. “SQUID-on-tip with single-electron spin sensitivity for high-field and ultra-low temperature nanomagnetic imaging”. In: *Nanoscale* 12.5 (2020), pp. 3174–3182. doi: 10.1039/C9NR08578E.

[54] Filippo Pizzocchero et al. “The hot pick-up technique for batch assembly of van der Waals heterostructures”. In: *Nature Communications* 7.1 (Sept. 2016), p. 11894. doi: 10.1038/ncomms11894.

[55] Rebeca Ribeiro-Palau et al. “Twistable electronics with dynamically rotatable heterostructures”. In: *Science* 361.6403 (Aug. 17, 2018). Publisher: American Association for the Advancement of Science, pp. 690–693. doi: 10.1126/science.aat6981.

[56] Theo Pellegrin. “Mesure du magnétisme orbital du graphène”. Masters Thesis. Université Paris-Sud, 2017.

[57] *MODEL SR830 DSP Lock-In Amplifier*. Oct. 2011.

[58] *Principles of lock-in detection and the state of the art*. Zurich Instruments. 2016.

[59] M. V. Berry. "Quantal Phase Factors Accompanying Adiabatic Changes". In: *Proceedings of the Royal Society of London. Series A, Mathematical and Physical Sciences* 392.1802 (1984), pp. 45–57.

[60] Mikito Koshino and Tsuneya Ando. "Orbital diamagnetism in multilayer graphenes: Systematic study with the effective mass approximation". In: *Physical Review B* 76.8 (Aug. 17, 2007), p. 085 425. doi: 10.1103/PhysRevB.76.085425.

[61] Yuya Ominato and Mikito Koshino. "Orbital magnetism of graphene flakes". In: *Physical Review B* 87.11 (Mar. 25, 2013), p. 115433. doi: 10.1103/PhysRevB.87.115433.

[62] Hidetoshi Fukuyama. "Anomalous Orbital Magnetism and Hall Effect of Massless Fermions in Two Dimension". In: *Journal of the Physical Society of Japan* 76.4 (Apr. 15, 2007), p. 043711. doi: 10.1143/JPSJ.76.043711.

[63] Oleg V Yazyev. "Emergence of magnetism in graphene materials and nanostructures". In: *Reports on Progress in Physics* 73.5 (May 1, 2010), p. 056501. doi: 10.1088/0034-4885/73/5/056501.

[64] M. Sepioni et al. "Limits on Intrinsic Magnetism in Graphene". In: *Physical Review Letters* 105.20 (Nov. 12, 2010), p. 207205. doi: 10.1103/PhysRevLett.105.207205.

[65] Zhilin Li et al. "Field and temperature dependence of intrinsic diamagnetism in graphene: Theory and experiment". In: *Physical Review B* 91.9 (Mar. 27, 2015), p. 094429. doi: 10.1103/PhysRevB.91.094429.

[66] Lianlian Chen et al. "Fabrication of vertically aligned graphene sheets on SiC substrates". In: *RSC Advances* 3.33 (2013), p. 13926. doi: 10.1039/c3ra40840j.

[67] Jian-Hao Chen et al. "Tunable Kondo effect in graphene with defects". In: *Nature Physics* 7.7 (July 2011), pp. 535–538. doi: 10.1038/nphys1962.

[68] S. G. Sharapov, V. P. Gusynin, and H. Beck. "Magnetic oscillations in planar systems with the Dirac-like spectrum of quasiparticle excitations". In: *Physical Review B* 69.7 (Feb. 17, 2004), p. 075104. doi: 10.1103/PhysRevB.69.075104.

[69] Amit Ghosal, Pallab Goswami, and Sudip Chakravarty. “Diamagnetism of nodal fermions”. In: *Physical Review B* 75.11 (Mar. 22, 2007), p. 115123. doi: 10.1103/PhysRevB.75.115123.

[70] J. Martin et al. “Observation of electron–hole puddles in graphene using a scanning single-electron transistor”. In: *Nature Physics* 4.2 (Feb. 2008), pp. 144–148. doi: 10.1038/nphys781.

[71] Jiamin Xue et al. “STM Spectroscopy of ultra-flat graphene on hexagonal boron nitride”. In: *Nature Materials* 10.4 (Apr. 2011), pp. 282–285. doi: 10.1038/nmat2968. arXiv: 1102.2642[cond-mat].

[72] C. R. Woods et al. “Commensurate–incommensurate transition in graphene on hexagonal boron nitride”. In: *Nature Physics* 10.6 (June 2014), pp. 451–456. doi: 10.1038/nphys2954.

[73] Jeil Jung et al. “Moiré band model and band gaps of graphene on hexagonal boron nitride”. In: *Physical Review B* 96.8 (Aug. 30, 2017), p. 085442. doi: 10.1103/PhysRevB.96.085442.

[74] J. Vallejo Bustamante et al. “Singular paramagnetic orbital magnetism in Graphene with a moiré potential. In preparation.” In: ().

[75] R. Peierls. “Zur Theorie des Diamagnetismus von Leitungselektronen”. In: *Zeitschrift fur Physik* 80.11 (Nov. 1933), pp. 763–791. doi: 10.1007/BF01342591.

[76] G. Gómez-Santos and T. Stauber. “Measurable Lattice Effects on the Charge and Magnetic Response in Graphene”. In: *Physical Review Letters* 106.4 (Jan. 27, 2011), p. 045504. doi: 10.1103/PhysRevLett.106.045504.

[77] A. Principi et al. “Many-body orbital paramagnetism in doped graphene sheets”. In: *Physical Review Letters* 104.22 (June 2, 2010), p. 225503. doi: 10.1103/PhysRevLett.104.225503. arXiv: 1004.2636[cond-mat].

[78] Matthew Yankowitz et al. “Emergence of superlattice Dirac points in graphene on hexagonal boron nitride”. In: *Nature Physics* 8.5 (May 2012), pp. 382–386. doi: 10.1038/nphys2272.

[79] Menyoung Lee et al. “Ballistic miniband conduction in a graphene superlattice”. In: *Science* 353.6307 (Sept. 30, 2016), pp. 1526–1529. doi: 10.1126/science.aaf1095.

[80] D. I. Indolese et al. “Signatures of van Hove Singularities Probed by the Supercurrent in a Graphene-hBN Superlattice”. In: *Physical Review Letters* 121.13 (Sept. 25, 2018), p. 137701. doi: 10.1103/PhysRevLett.121.137701.

[81] Sanfeng Wu et al. “Multiple hot-carrier collection in photo-excited graphene Moiré superlattices”. In: *Science Advances* 2.5 (May 6, 2016), e1600002. doi: 10.1126/sciadv.1600002.

[82] Rai Moriya et al. “Emergence of orbital angular moment at van Hove singularity in graphene/h-BN moiré superlattice”. In: *Nature Communications* 11.1 (Dec. 2020), p. 5380. doi: 10.1038/s41467-020-19043-x.

[83] Yuan Cao et al. “Correlated insulator behaviour at half-filling in magic-angle graphene superlattices”. In: *Nature* 556.7699 (Apr. 5, 2018), pp. 80–84. doi: 10.1038/nature26154.

[84] Yuan Cao et al. “Unconventional superconductivity in magic-angle graphene superlattices”. In: *Nature* 556.7699 (Apr. 2018), pp. 43–50. doi: 10.1038/nature26160.

[85] Pilkyung Moon and Mikito Koshino. “Electronic properties of graphene / hexagonal -boron - nitride moiré superlattice”. In: *Physical Review B* 90.15 (Oct. 3, 2014), p. 155406. doi: 10.1103/PhysRevB.90.155406.

[86] J. R. Wallbank et al. “Generic miniband structure of graphene on a hexagonal substrate”. In: *Physical Review B* 87.24 (June 4, 2013), p. 245408. doi: 10.1103/PhysRevB.87.245408.

[87] Jeil Jung et al. “Origin of band gaps in graphene on hexagonal boron nitride”. In: *Nature Communications* 6.1 (May 2015), p. 6308. doi: 10.1038/ncomms7308.

[88] J. N. Fuchs and F. Piechon. *Moire bands calculation*.

[89] Noah F. Q. Yuan and Liang Fu. “Classification of critical points in energy bands based on topology, scaling, and symmetry”. In: *Physical Review B* 101.12 (Mar. 23, 2020), p. 125120. doi: 10.1103/PhysRevB.101.125120.

[90] Haoxin Zhou et al. “Isospin magnetism and spin-polarized superconductivity in Bernal bilayer graphene”. In: *Science* 375.6582 (Feb. 18, 2022), pp. 774–778. doi: 10.1126/science.abm8386.

[91] Sergio C. de la Barrera et al. “Cascade of isospin phase transitions in Bernal-stacked bilayer graphene at zero magnetic field”. In: *Nature Physics* 18.7 (July 2022), pp. 771–775. doi: 10.1038/s41567-022-01616-w.

[92] Edward McCann and Mikito Koshino. “The electronic properties of bilayer graphene”. In: *Reports on Progress in Physics* 76.5 (Apr. 2013). Publisher: IOP Publishing, p. 056503. doi: 10.1088/0034-4885/76/5/056503.

[93] A. B. Kuzmenko et al. “Determination of the gate-tunable band gap and tight-binding parameters in bilayer graphene using infrared spectroscopy”. In: *Physical Review B* 80.16 (Oct. 8, 2009), p. 165406. doi: 10.1103/PhysRevB.80.165406.

[94] M. Mucha-Kruczyński, E. McCann, and Vladimir I. Fal’ko. “Electron–hole asymmetry and energy gaps in bilayer graphene”. In: *Semiconductor Science and Technology* 25.3 (Feb. 2010), p. 033001. doi: 10.1088/0268-1242/25/3/033001.

[95] J. Blinowski and C. Rigaux. “Theory of magnetic susceptibility in acceptor and donor graphite intercalation compounds”. In: *Journal de Physique* 45.3 (1984), pp. 545–555. doi: 10.1051/jphys:01984004503054500.

[96] S. A. Safran. “Stage dependence of magnetic susceptibility of intercalated graphite”. In: *Physical Review B* 30.1 (July 1, 1984), pp. 421–423. doi: 10.1103/PhysRevB.30.421.

[97] Yuanbo Zhang et al. “Direct observation of a widely tunable band gap in bilayer graphene”. In: *Nature* 459.7248 (June 2009). Number: 7248 Publisher: Nature Publishing Group, pp. 820–823. doi: 10.1038/nature08105.

[98] Edward McCann. “Asymmetry gap in the electronic band structure of bilayer graphene”. In: *Physical Review B* 74.16 (Oct. 18, 2006), p. 161403. doi: 10.1103/PhysRevB.74.161403.

[99] Eduardo V. Castro et al. “Biased Bilayer Graphene: Semiconductor with a Gap Tunable by the Electric Field Effect”. In: *Physical Review Letters* 99.21 (Nov. 20, 2007), p. 216802. doi: 10.1103/PhysRevLett.99.216802.

[100] Mikito Koshino and Tsuneya Ando. “Anomalous orbital magnetism in Dirac-electron systems: Role of pseudospin paramagnetism”. In: *Physical Review B* 81.19 (May 25, 2010). Publisher: American Physical Society, p. 195431. doi: 10.1103/PhysRevB.81.195431.

[101] Long Ju et al. “Topological valley transport at bilayer graphene domain walls”. In: *Nature* 520.7549 (Apr. 2015), pp. 650–655. doi: 10.1038/nature14364.

[102] M Junaid and G Witjaksono. “Analysis of Band Gap in AA and AB Stacked Bilayer Graphene by Hamiltonian Tight Binding Method”. In: 2019 IEEE International Conference on Sensors and Nanotechnology (SENSORS & NANO). Penang, Malaysia: IEEE, July 2019, pp. 1–4. doi: 10.1109/SENSORSNANO44414.2019.8940102.

[103] Long Ju et al. “Tunable excitons in bilayer graphene”. In: *Science* 358.6365 (Nov. 17, 2017), pp. 907–910. doi: 10.1126/science.aam9175.

[104] Aaron L. Sharpe et al. “Emergent ferromagnetism near three-quarters filling in twisted bilayer graphene”. In: *Science* 365.6453 (Aug. 9, 2019), pp. 605–608. doi: 10.1126/science.aaw3780.

[105] M. Serlin et al. “Intrinsic quantized anomalous Hall effect in a moiré heterostructure”. In: *Science* 367.6480 (Feb. 21, 2020). doi: 10.1126/science.aay5533.

[106] Jianpeng Liu et al. “Quantum Valley Hall Effect, Orbital Magnetism, and Anomalous Hall Effect in Twisted Multilayer Graphene Systems”. In: *Physical Review X* 9.3 (Aug. 8, 2019), p. 031021. doi: 10.1103/PhysRevX.9.031021.

[107] Jörn W. F. Venderbos and Liang Fu. “Interacting Dirac fermions under a spatially alternating pseudomagnetic field: Realization of spontaneous quantum Hall effect”. In: *Physical Review B* 93.19 (May 13, 2016), p. 195126. doi: 10.1103/PhysRevB.93.195126.

[108] C.-C. Hsu et al. “Nanoscale strain engineering of giant pseudomagnetic fields, valley polarization, and topological channels in graphene”. In: *Science Advances* 6.19 (May 8, 2020), eaat9488. doi: 10.1126/sciadv.aat9488.

[109] Yu Zhang et al. “Correlation-induced valley splitting and orbital magnetism in a strain-induced zero-energy flatband in twisted bilayer graphene near the magic angle”. In: *Physical Review B* 102.8 (Aug. 24, 2020), p. 081403. doi: 10.1103/PhysRevB.102.081403.

[110] Daniele Guerci, Pascal Simon, and Christophe Mora. “Moiré lattice effects on the orbital magnetic response of twisted bilayer graphene and Condon instability”. In: *Physical Review B* 103.22 (June 29, 2021), p. 224436. doi: 10.1103/PhysRevB.103.224436.

[111] S. G. Xu et al. “Giant oscillations in a triangular network of one-dimensional states in marginally twisted graphene”. In: *Nature Communications* 10.1 (Dec. 2019), p. 4008. doi: 10.1038/s41467-019-11971-7.

[112] A Reserbat-Plantey et al. “Strain Superlattices and Macroscale Suspension of Graphene Induced by Corrugated Substrates”. In: *Nano Letters* 14.9 (Sept. 10, 2014), pp. 5044–5051. doi: 10.1021/nl5016552.

[113] C. L. Kane and E. J. Mele. “Quantum Spin Hall Effect in Graphene”. In: *Physical Review Letters* 95.22 (Nov. 23, 2005), p. 226801. doi: 10.1103/PhysRevLett.95.226801.

[114] P. Potasz and J. Fernández-Rossier. “Orbital Magnetization of Quantum Spin Hall Insulator Nanoparticles”. In: *Nano Letters* 15.9 (Sept. 9, 2015), pp. 5799–5803. doi: 10.1021/acs.nanolett.5b01805.

[115] Hae Jin Kim et al. “Unexpected orbital magnetism in Bi-rich Bi2Se3 nanoplatelets”. In: *NPG Asia Materials* 8.5 (May 2016), e271–e271. doi: 10.1038/am.2016.56.

Résumé

1. Magnétisme orbital

Nous consacrons le premier chapitre 1 au magnétisme orbital. Dans ce chapitre, nous présenterons une très brève introduction aux définitions fondamentales nécessaires pour le reste du manuscrit. On mentionnera également l'interrelation entre les caractéristiques accessibles expérimentalement de la susceptibilité orbitale et les particularités de la structure de bande qui sont à leur origine.

La relation principale que nous utilisons définit la réponse linéaire magnétique d'un système en présence d'un champ magnétique externe

$$\vec{M} \equiv \chi_{orb}\vec{B} \tag{8.1}$$

où $\vec{B}$ est le champ magnétique externe, χ_{orb} est la susceptibilité et $\vec{M}$ est l'aimantation du système.

Parce qu'en 2D, $\vec{M}$ est la densité de moments magnétiques $\vec{m}$ par unité de surface, l'aimantation sera donnée en Ampères, A, le champ extérieur en Tesla, T, et donc, le la susceptibilité sera donnée en Ampère par Tesla, A/T.

Lorsque l'aimantation s'oppose au champ magnétique, de manière équivalente $\vec{M}$ et $\vec{B}$ sont anti-parallèles, alors la susceptibilité est négative, $\chi_{orb} < 0$. On parle dans ce cas de diamagnétisme orbital. Dans le cas contraire, lorsque $\vec{M}$ et $\vec{B}$ sont parallèles, on parle de paramagnétisme orbital et $\chi_{orb} > 0$. Tout ceci est général au magnétisme 2D.

Dans le cas d'un ensemble grand canonique, l'aimantation est

$$\vec{M} = -\frac{1}{S}\frac{\partial\Omega}{\partial B}\vec{u}_z \tag{8.2}$$

et par conséquent, la susceptibilité orbitale est

$$\chi_{orb} = -\frac{1}{S}\frac{\partial^2\Omega}{\partial B^2}\bigg|_{B\to 0} \tag{8.3}$$

où Ω es le grand potentiel.

2. Graphène

Les propriétés générales et les caractéristiques les plus fondamentales du graphène sont présentées dans le chapitre 2. Ici, nous avons utilisé le modèle de liaisons fortes pour donner une explication très simple de sa propriété magnétique la plus importante, le pic diamagnétique de McClure divergeant au point de Dirac, qui est une signature étonnante de la phase de Berry anormale égale à π dans le graphène.

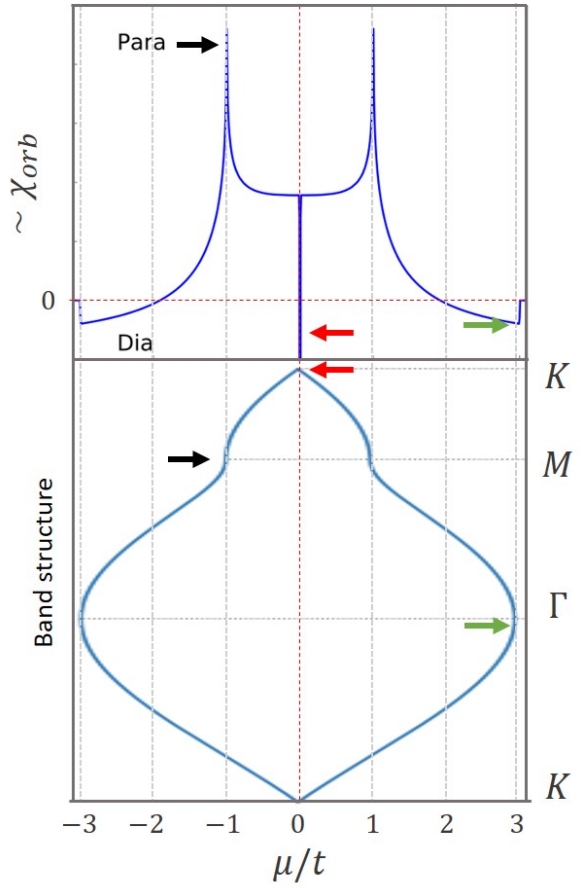

Figure 8.1: En haut : susceptibilité orbitale du graphène dans un modèle à 2 bandes couplées calculé en [36]. En bas : structure des bandes des deux bandes d'énergie les plus basses du graphène, calculée avec le package numérique pybinding [37]. Les flèches noires sont les points selle dans la structure des bandes, et la susceptibilité paramagnétique correspondante. Les flèches rouges montrent les endroits des points de Dirac avec des divergences diamagnétiques. Les flèches vertes correspondent aux bandes paraboliques et au diamagnétisme de Landau.

3. Sondes à effet de magnéto-resistance géante

Dans le troisième chapitre, nous présenterons l'un des aspects clés qui rend possible la détection expérimentale : les sondes à magnéto-résistance géante (GMR). Nous présenterons les caractéristiques ainsi qu'un modèle simple mais intuitif pour expliquer leur fonctionnement de manière générale.

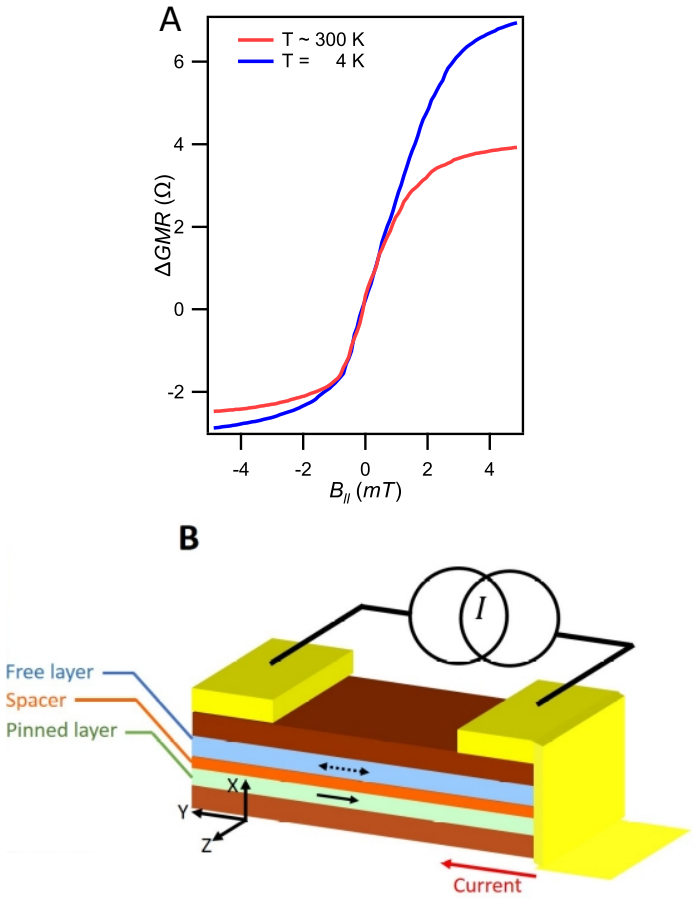

Figure 8.2: (A) Variation de la résistance d'une seule GMR en fonction du champ horizontal [17]. (B) Schéma d'une GMR dans la géométrie: courant dans le plan (CIP). Le courant circule parallèlement au plan des couches suivant l'axe y (flèche rouge). C'est la géométrie de nos sondes.

4. Technique de fabrication des stacks et principe de mesure

Le chapitre 4 détaille le montage et le principe de la détection expérimentale. Il met en évidence la technique qui permet de réduire les contributions des signaux magnétiques parasites. En particulier, nous montrons que le signal mésuré est proportionel à la dérivé de l'aimantation en fonction de la tension de grille

$$V_{lock-in} = IK\left[\frac{\partial R}{\partial B_M}\frac{\partial M}{\partial V_g}\delta V_g\right] \tag{8.4}$$

Nous présentons également la technique de fabrication de nos échantillons dans ce chapitre

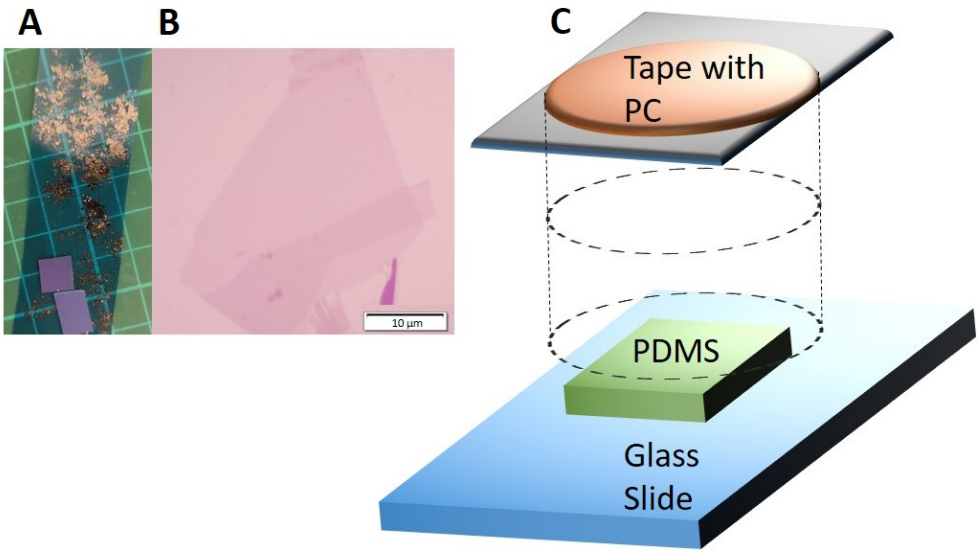

Figure 8.3: (A) Cristaux de graphite sur du ruban adhésif. (B) Monocouche de graphène sur un substrat de SiO_2/SiO. La monocouche est la partie où le contraste optique est le plus faible. (C) Schémas du dispositif consistant en une couche PC au-dessus d'un coussin PDMS utilisé pour fabriquer les stacks.

5. Résultats experimentaux: susceptibilité de McClure dans le graphène

L'étude expérimentale de la réponse singulière diamagnétique orbitale dans le graphène est donnée au chapitre 5. Il montre les mesures de l'aimantation dépendante de la tension de grille d'un seul flocon de graphène monocouche encapsulé entre des cristaux de nitrure de bore. Il est également accompagné d'un modèle théorique qui permet de comprendre les détails. Ce chapitre est tiré de l'article [17] qui a été publié au cours de ce projet.

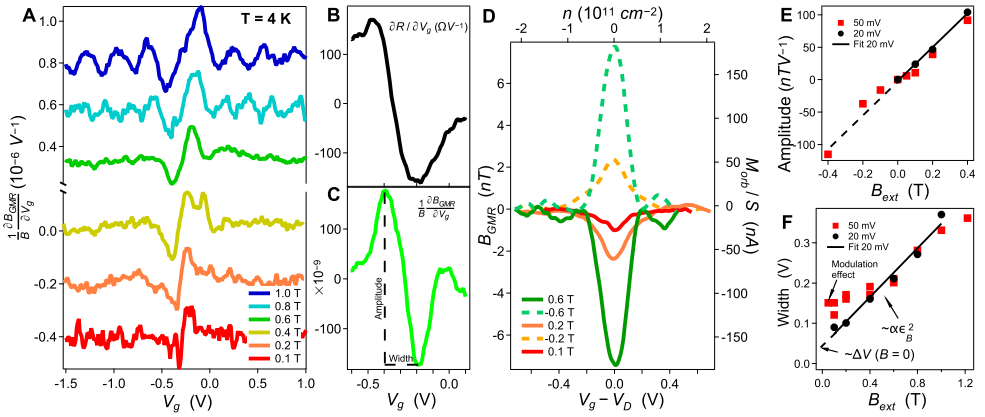

Figure 8.4: **A** : modulation détectée de la résistance du détecteur GMR avec une modulation de tension de grille AC de 20 mV, en fonction de la tension de grille continue. La quantité tracée est $\frac{\partial B_{GMR}}{\partial V_g}$, déduite du signal sur le capteur GMR calibré, divisée par le champ magnétique vertical appliqué B. Les données sont la moyenne de 80 mesures indépendantes . **B** : Dérivée par rapport à la tension de grille de la résistance à deux points du graphène mesurée à travers les électrodes latérales, dans la région du point de Dirac, avec une modulation de tension de grille de 50 mV. **C** : à des fins de comparaison, signal GMR à -0,6 T utilisant la même modulation de tension de grille que dans **B**. Le pic GMR est beaucoup plus étroit. **D** : intégration numérique des données tracées dans **A**, donnant l'aimantation par unité de surface en nA (axe de droite), et le champ magnétique B_{GMR} détecté par le dispositif GMR, en nT (axe de gauche), en fonction de la tension de grille. **E** et **F** : dépendances de champ des maxima et des largeurs de pic, définis dans **C**, pour des modulations de tension de grille de 20 et 50 mV, et comparaison avec les prédictions théoriques. Les écarts dus à l'amplitude de modulation excessive sont visibles pour une modulation de 50 mV.

6. Paramagnétisme orbital dans le graphène avec un potential de moiré

Ensuite au chapitre 6, nous présentons l'exploration expérimentale du magnétisme orbital du graphène monocouche dans un potentiel moiré. Cela a été fait en alignant le flocon de graphène avec l'un des cristaux de BN qui l'encapsule. En particulier, nous nous concentrons sur la région où les points de selle dans la structure de bande sont attendus, ce qui s'accompagne de divergences dans la densité des états. En ces points, la susceptibilité est attendue [18] et expérimentalement trouvée paramagnétique.

7. Magnétisme orbital dans la bicouche de graphene AB

Nous présentons les résultats préliminaires du magnétisme orbital du graphène bicouche dans le chapitre 7. Ici, nous nous intéressons principalement à l'évolution de la susceptibilité en tant que fonction du champ de déplacement électrique perpendiculaire.

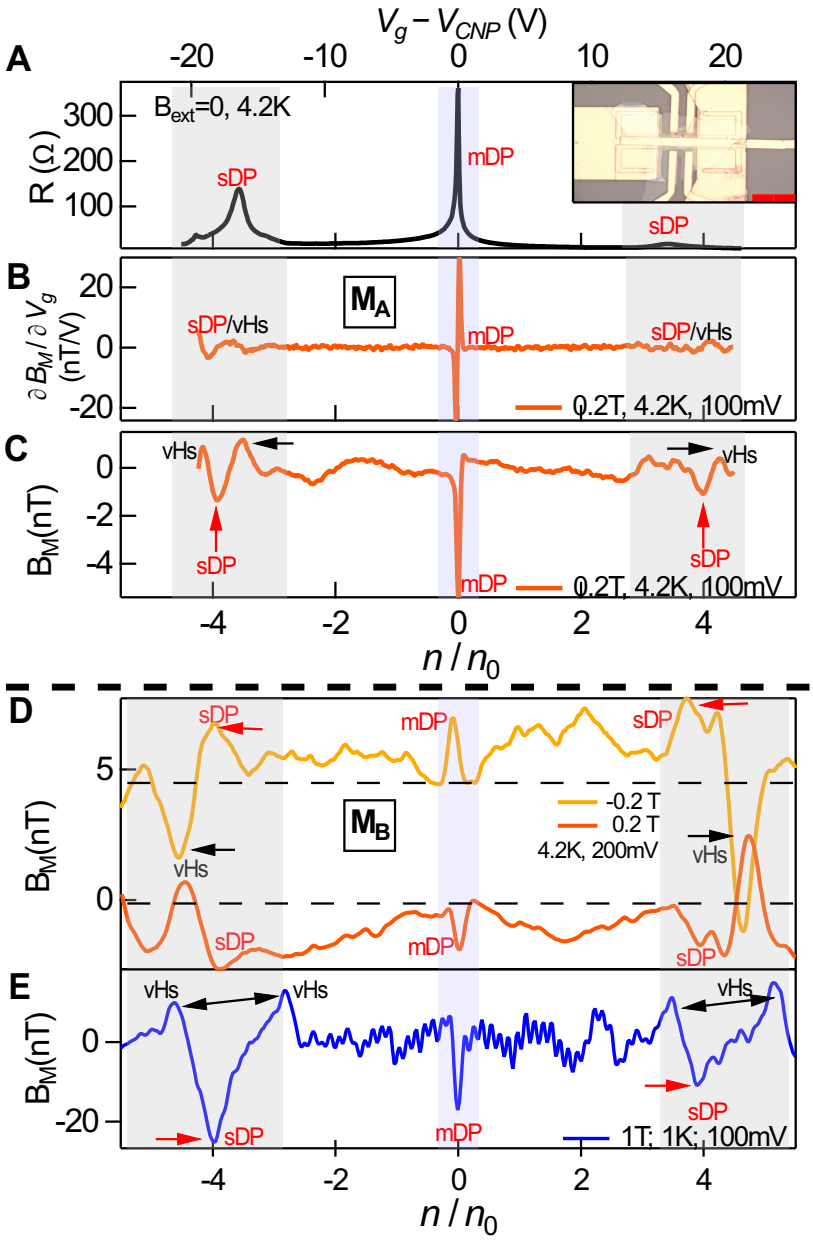

Figure 8.5: **(A)** Résistance à 4 terminales de l'échantillon M_A. **(B)** Dérivée de l'aimantation en fonction de la tension de grille et de la densité de porteurs (renormalisée à n_0) pour une grande plage de dopage dans un champ magnétique externe de 0,2T pour le même échantillon. **(B)** Aimantation (en unités du champ magnétique détecté sur les GMR) obtenue par intégration numérique des données en (C). Près de la région des pics secondaires de Dirac, on observe des pics diamagnétiques (flèches rouges) entourés de pics paramagnétiques (flèches noires). **(D)** Données GMR mesurées sur l'échantillon M_B. Aimantation intégrée numériquement en fonction de la densité de porteurs (renormalisée à n_0) $\pm$0.2 T et 1 T **(E)**.

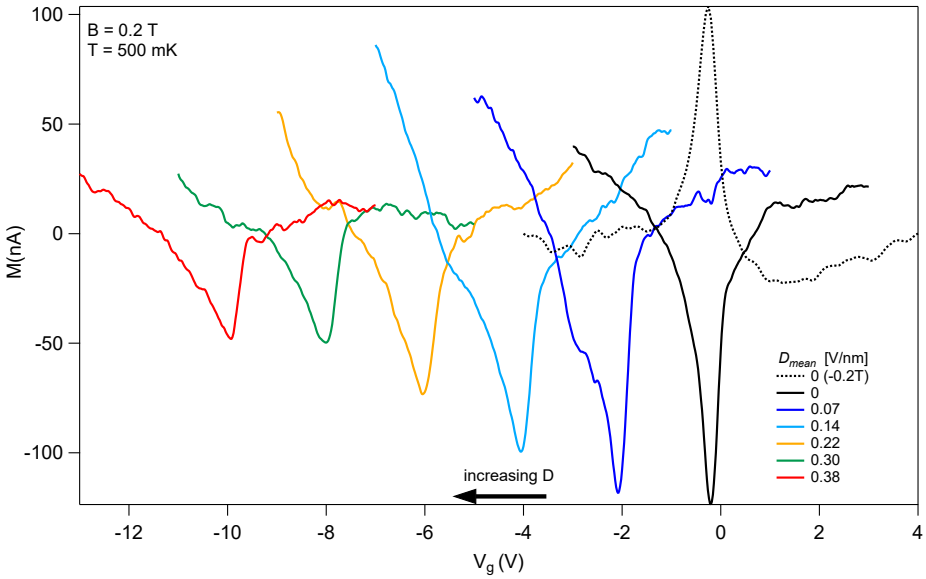

Figure 8.6: Pic de McClure pour le graphène bicouche pour différentes valeurs du champ de déplacement D. La température dans ces mesures est de l'ordre de 500 mK.